IJRAR.ORG E-ISSN: 2348-1269, P-ISSN: 2349-5138

INTERNATIONAL JOURNAL OF RESEARCH AND ANALYTICAL REVIEWS (IJRAR) | IJRAR.ORG

An International Open Access, Peer-reviewed, Refereed Journal

PARAMETRIC NUMERICAL ANALYSIS OF UNSTEADY NEWTONIAN FLUID FLOW IN ROTATING POROUS CHANNELS WITH HEAT AND MASS TRANSFER EFFECTS

Sanjay Kumar Suman

Department of Mathematics, Government Degree College, Bagaha, West Champaran, B.R.A. Bihar University, Muzaffarpur, Bihar, India.

ABSTRACT :

This research presents a comprehensive numerical investigation of unsteady Newtonian fluid flow through three distinct porous geometries: open rectangular channels, vertical porous plates with rotation, and rotating parallel plate configurations1. The study employs advanced finite difference methods to solve dimensionless governing equations, systematically examining the coupled effects of rotation, magnetic fields, porosity, and thermal-chemical phenomena on fluid dynamics, heat transfer, and mass transport processes1.

The mathematical formulation incorporates multiple physical effects including chemical reactions, thermal radiation, Soret and Dufour phenomena, and magnetohydrodynamic interactions under rotating reference frames1. Parametric analysis reveals that primary velocity components increase with rotation parameters while secondary velocities exhibit opposite behavior, and magnetic field intensity consistently reduces resultant velocities throughout the fluid domain1. The investigation demonstrates that thermal diffusion enhances species concentration while chemical reactions diminish it, and heat transfer rates correlate positively with Prandtl numbers, radiation parameters, and Dufour effects1.

Extensive numerical computations spanning 32 comprehensive data tables provide detailed velocity profiles, skin friction coefficients, Nusselt numbers, and Sherwood numbers across varying Ekman numbers (0.01-0.04), Hartmann numbers (1-10), inverse Darcy parameters (2000-5000), and material parameters1. The study establishes that permeability reduction significantly impacts velocity distributions, with lower permeability media yielding reduced resultant velocities, while both velocity components enhance with increased relaxation times1.

This work fills critical gaps in understanding multi-physics fluid flow phenomena in rotating porous systems fluid dynamics in industrial applications1. The comprehensive parametric database serves as a foundational resource for designing chemical processing equipment, optimizing manufacturing systems, and developing

advanced thermal management technologies. The validated numerical methodology offers robust tools for future investigations into complex fluid-structure interactions, biomedical flow applications, and emerging energy systems involving rotating porous media. The research significantly contributes to the theoretical understanding of coupled transport phenomena while providing practical design guidelines for engineering applications requiring precise flow control and thermal management in rotating environments.

Keywords: Magnetohydrodynamic flows,Rotating porous media,Soret-Dufour effects,Finite difference method,Thermal radiation.

INTRODUCTION :

The present paper reports on a numerical study of the nature of unsteady Newtonian fluid flow through porous media, focusing on situations where dust particles are embedded and in rotating fluid systems. Fluid flow with suspended particulate matter is very important in a wide range of engineering fields. Earlier studies in this field are Saffman's study of the stability of laminar dusty gas flow, Liu's study of flow caused by an oscillating plate in a dusty gas, and Michael and Miller's study on dusty gas motion over a rigid boundary. More recently, Ghosh and Ghosh investigated MHD flow of viscoelastic fluid in porous media, Nabil investigated couple stress influence on pulsatile hydromagnetic Poiseuille flow, and Sleep researched organic vapor transport within porous media using the dusty gas model. In addition, Mitra and Bhattacharyya investigated unsteady hydromagnetic laminar flow of a conducting dusty fluid, Hamdan considered dusty gas flow in porous media, and Allan solved dusty gas flow in naturally occurring porous media. The theory of Frenet frames, which is a pillar in differential geometry, provides a coordinate system in which to describe structure in relation to an object of concern as opposed to external coordinate systems.

In addition to dusty fluid flows, rotating flows in porous media have become a focus of considerable interest in computational fluid dynamics. The combined effects of mass and heat transfer in rotational hydrodynamics find significant importance in chemical engineering and industrial manufacturing processes. Greenspan laid down some of the fundamental theoretical basis for rotating fluids, whereas Dorfman reported hydrodynamic resistance and heat loss for rotating solids. Kreith led the research in convective heat transfer under rotating fields, while Takhar and Whitelaw gave an understanding of higher-order heat transfer from rotating spheres. Hossain and Takhar researched radiation-conduction interaction in combined convection within rotating bodies. Follow-up studies are Naroua et al.'s investigation of natural convection in rotating fluids with radiation by the finite element method and Deka et al.'s investigation of fluid flow along an accelerated horizontal plate in a rotating fluid. Exact solutions of unsteady hydrodynamic and hydromagnetic boundary layer equations in rotating fluid systems have been obtained by Debnath. Sarojamma and Krishna studied transient hydromagnetic convective flow in rotating channels with porous boundaries, whereas

Smirnov and Shatrov studied boundary layer growth on a plate in a rotating system. Wang studied stretching of a surface in a rotating fluid, and Takhar and Nath studied unsteady flow over a stretching surface in a rotating fluid under the influence of a magnetic field. Ganapathy discussed oscillatory Couette flow in rotating systems, and Singh and Singh et al. discussed oscillatory hydromagnetic Couette flow in rotating systems, including periodic solutions for oscillatory Couette flow in porous media. Lastly, Ghosh discussed the nature of unsteady hydromagnetic flow in a rotating channel with an oscillating pressure gradient.

Based on these well-established findings, the present paper discusses numerical solutions and results for fluid flow through three different porous media configurations: an open porous rectangular channel, a rotating vertical porous plate, and a parallel rotating plate channel. The graphical representations are used to depict the effect of different parameters, giving rise to particular conclusions about the flow characteristics. Expressions for skin-friction at the boundaries are also obtained.

MATHEMATICAL FORMULATION AND SOLUTIONS :

The laminar flow of a rotating fluid past a porous plate in conducting field with variable temperature and variable concentration taking into account the chemical reaction, radiation, thermal diffusion and Dufour effects is considered. *X*-axis is taken along the plate which is in vertical direction. *Y*-axis is taken normal to the surface of the plate. The plate as well as the fluid in a state of rigid body rotates with a uniform angular velocity Ω about *Y*-axis. Initially at time $t^* \leq 0$, both the fluid and the plate are at rest with uniform temperature and concentration T_∞ and C_∞ respectively. At time $t^* > 0$, the plate starts moving in the *X* direction with uniform velocity $U_0 a^* t^*$. The temperature concentration rises to

$$T_\infty + (T_s^* - T_\infty)\left(\frac{t^*}{t_0}\right) \text{ and } C_\infty + (C_s^* - C_\infty)\left(\frac{t^*}{t_0}\right)$$

respectively. Later on it is maintained at uniform temperature T_∞ and concentration C_∞ respectively. Under these considerations the equations that govern the flow is

$$\frac{\partial u^*}{\delta t^*} + 2\Omega V^* = \nu \frac{\partial^* u^*}{\partial_{y^*}{}^2} + g\beta_T (T^* - T_\infty) - g\beta_C (C^* - C_\infty) - \frac{\sigma B_0^2 u^*}{\rho} - \frac{\nu}{k} u^* \quad \ldots\ldots (1)$$

$$\frac{\partial V^*}{\partial t^*} - 2\Omega u^* = \nu \frac{\partial^2 V^*}{\partial y^{*2}} - \frac{\sigma B_0^2 V^*}{\rho} - \frac{\nu}{k} V^* \qquad \ldots\ldots\ldots (2)$$

$$\rho C_P \frac{\partial T^*}{\partial t^*} = k_T \frac{\partial^2 T^*}{\partial y^{*2}} + Q^* (T^* - T_\infty) - \frac{\partial q_r^*}{\partial y^*} + \frac{D_m k_T \rho}{C_s} \frac{\partial^2 C^*}{\partial y^*} \qquad \ldots\ldots\ldots\ldots (3)$$

$$\frac{\partial C^*}{\partial t^*} = D \frac{\partial^2 C^*}{\partial y^*} - K_r^* (C^* - C_\infty) + D_1 \frac{\partial^2 T^*}{\partial y^*} \qquad \ldots\ldots\ldots (4)$$

The corresponding initial boundary conditions are

$$\left.\begin{array}{l} u^*=0, V^*=0, T^*=T_\infty, C^*=C_\infty \text{ for all } y^*, t^* \leqslant 0 \\ t^*>0: u^*=U_0 a^* t^*, V^*=U_0 a^* t^*, T^*=T_\infty+(T_s^*-T_\infty)\left(\frac{t^*}{t_0}\right) \\ C^*=C_\infty+(C_s^*-C_\infty)\left(\frac{t^*}{t_0}\right) \text{ at } y^*=0 \\ u^*=0, T^*=T_\infty, C^*=C_\infty \text{ as } y^* \to \infty \end{array}\right\} \quad \ldots\ldots (5)$$

The term $\frac{\partial_{q_r^*}}{\partial_{y^*}}$ in equation 3 represents the changes in the radiative flux with the distance normal to the plate.

For an optically thin grey gas, the local radiant is given by $\frac{\partial_{q_r^*}}{\partial_{y^*}}=4a^{'}\sigma^*\left(T_\infty^{*4}-T^{*4}\right)$ where σ^* and $a^{'}$ are the Stefan-Boltzmann constant. We assume that the difference within the flow is sufficiently small so that T^{*4} can be expressed as a linear function of T^* after using the Taylor's series to expand T^{*4} about the free stream temperature T_∞^{*4} and neglecting the higher order terms resulting in approximation $T^{*4} \cong 4T_\infty^{*3}T^*-3T_\infty^{*4}$. Thus equation 2 takes the form

$$\rho C_p \frac{\partial T^*}{\partial t^*}=k\frac{\partial^2 T^*}{\partial y^{*2}}+q_0(T^*-T_\infty^*)-16a^{'}\sigma^* T_\infty^{*3}(T^*-T_\infty^*) \quad \ldots\ldots (6)$$

The non-dimensional quantities are as follows

$$u=\frac{u^*}{U_0}, V=\frac{V^*}{U_0}, t=\frac{t^* U_0^2}{v}, y=\frac{y^* U_0}{v}, \theta=\frac{T^*-T_\infty}{T_s^*-T_\infty}, C=\frac{C^*-C_\infty}{C_s^*-C_\infty}, a=\frac{a^* v}{U_0^2}, \frac{\partial q_r^*}{\partial y^*}=4(T^*-T_\infty)I^*$$

$$Gr=\frac{vg\beta_T(T_s^*-T_\infty)}{U_0^3}, \text{ (Grashof number)}$$

$$Gm=\frac{vg\beta_C(C_s^*-C_\infty)}{U_0^3}, \text{ (Modified Grashof number)}$$

$$M=\frac{\sigma B_0^2 v}{\rho U_0^2}, \text{(Magnetic parameter)}$$

$$k_1^2=\frac{\partial v}{U_0^2}, \text{ (Rotation parameter)}$$

$$K=\frac{kU_0^2}{v^2}, \text{(Permeability of the porous medium)}$$

$$\Pr=\frac{\rho v C_P}{k_T}, \text{(Prandtl number)}$$

$$Q=\frac{Q^* v^2}{k_T U_0^2}, \text{ (Heat absorption)}$$

$$F=\frac{4vI^*}{\rho C_p U_0^2}, \text{(Radiation parameter)}$$

$$Sc=\frac{v}{D}, \text{ (Schmidt number)}$$

$$S_0=\frac{D_1(T_s^*-T_\infty)}{v(C_*^*-C_\infty)} \text{(Soret number)}$$

$$Df=\frac{D_m k_T(C_4^*-C_\infty)}{vC_\alpha C_p(T_*^*-T_\infty)} \text{(Dufour number)}$$

$$Kr=\frac{K_r^* v^2}{U_0^2}, \text{(Chemical reaction parameter)}$$

On the basis of above non-dimensional quantities eq. (1)-(2) reduces to

$$\frac{\partial u}{\partial t}+2k_1^2V=\frac{\partial^2 u}{\partial_{y^2}}+Gr\theta+GmC-Mu-\frac{1}{K}u \quad \ldots\ldots\ldots\ldots (7)$$

$$\frac{\partial V}{\partial t}-2k_1^2u=\frac{\partial^2 V}{\partial Y^2}-MV-\frac{1}{K}V \quad \ldots\ldots\ldots (8)$$

$$\frac{\partial \theta}{\partial t}=\frac{1}{Pr}\frac{\partial^2 \theta}{\partial Y^2}+Q\theta-F\theta+Df\frac{\partial^2 C}{\partial Y^2} \quad \ldots\ldots\ldots (9)$$

$$\frac{\partial C}{\partial t}\frac{1}{Sc}\frac{\partial^2 C}{\partial Y^2}-KrC+S_0\frac{\partial^2 \theta}{\partial Y^2} \quad \ldots\ldots\ldots\ldots (10)$$

The corresponding initial boundary conditions are:

$$\left.\begin{array}{l} u=0,\quad V=0,\theta=0,C=0 \quad \text{for all } y,t\le 0 \\ t>0:\quad u=e^{at},V=e^{at},\theta=t,C=t \quad \text{at } y=0 \\ \quad u=0,\quad V=0,\theta=0,C=0 \quad \text{as } y\to\infty \end{array}\right\}$$

We observe that (7)–(10) are linear partial differential equations and they are to be solved with the initial and boundary conditions (11). In fact the exact solution is not possible for this set of equations and hence we solve these equations by finite-difference method. The equivalent finite difference schemes of equations for(7)–(10) are as follows:

$$\frac{u_{i,j+1}-u_{i,j}}{\Delta t}+2k_1^2V_{i,j}=Gr\,\theta_{i,j}+Gm\,C_{i,j}+\frac{u_{i-1,j}-2u_{i,j}+u_{i+1,j}}{(\Delta y)^2}-M\,u_{i,j}-\frac{1}{K}u_{i,j} \quad \ldots\ldots(11)$$

$$\frac{V_{i,j+1}-V_{i,j}}{\Delta t}-2k_1^2u_{i,j}=\frac{V_{i-1,j}-2V_{i,j}+V_{i+1,j}}{(\Delta y)^2}-M\,V_{i,j}-\frac{1}{K}V_{i,j} \quad \ldots\ldots(12)$$

$$\frac{\theta_{i,j+1}-\theta_{i,j}}{\Delta t}=\frac{1}{\mathrm{Pr}}\frac{\theta_{i-1,j}-2\theta_{i,j}+\theta_{i+1,j}}{(\Delta y)^2}+Q\theta_{i,j}-F\theta_{i,j}+Df\frac{C_{i-1,j}-2C_{i,j}+C_{i+1,j}}{(\Delta y)^2} \quad \ldots\ldots(13)$$

$$\frac{C_{i,j+1}-C_{i,j}}{\Delta t}=\frac{1}{Sc}\frac{C_{i-1,j}-2C_{i,j}+C_{i+1,j}}{(\Delta y)^2}-KrC_{i,j}+S_0\frac{\theta_{i-1,j}-2\theta_{i,j}+\theta_{i+1,j}}{(\Delta y)^2} \quad \ldots\ldots(14)$$

Here, the suffixes i refer to y and j to time. The mesh system is divided by taking Δy = 0.1. From the initial condition in(11), we have the following equivalent:

$u(i,0)=0$, $V=0$, $\theta(i,0)=0$, $C(i,0)=0$ $\forall i$ ……(15)

The boundary conditions from (11) are expressed in finite difference form as follows

$u(0,j)=e^{at}$, $V(0,j)=e^{at}$, $\theta(0,j)=t$ $\forall j$;$u(i_{max},j)=0$, $V(i_{max},j)=0$, $\theta(i_{max},j)=0$, $C(i_{max},j)=0$ $\forall j$.

(here i_{max} is taken as 200)

The primary velocity at the end of time step viz, $u\,(i, j + 1)$, $i = 1, \ldots, 200$ is computed from (11) and the secondary velocity at the end of time step viz, $V\,(i, j + 1)$, $i = 1, \ldots, 200$ is computed from(12) in terms of velocity, temperature and concentration at points on the earlier time-step. After that $\theta\,(i, j + 1)$ is computed from(13) and then $C\,(i, j + 1)$ is computed from(14). The procedure is

repeated until $t - 0.5$ (i.e., $j = 500$). During computation Δt is chosen as 0.001.

The skin-friction in non-dimensional form is given by : $\tau = \left(\frac{du}{dy}\right)_{y=0}$

The dimensionless rate of heat transfer in terms of Nusselt number : $Nu = -\left(\frac{d\theta}{dy}\right)_{y=0}$

The dimensionless rate of mass transfer in terms of Sherwood number : $Sh = -\left(\frac{dC}{dy}\right)_{y=0}$

If we consider the porous media to be a rotating parallel plate channel :

In the initial undisturbed state both the fluid and the plates are in rigid rotation with the same angular velocity Ω about the normal to the plates and at t > 0 the fluid is driven by constant pressure gradient parallel to the channel walls and in addition the lower plate perform non-torsional oscillations in its own plane. We choose a Cartesian system O(*x, y, z*) such that the boundary walls are at z=0 and z=*l*, z-axis being the axis of rotation of the plates. Since the plates extends to infinity along *x* and *y* directions, all the physical quantities except the pressure depend on *z* and *t* alone. The unsteady hydro magnetic equations governing the electrically conducting fluid under the influence of transverse magnetic field with reference to a frame rotating with a constant angular velocity Ω are

$$\rho\left[\frac{\partial V}{\partial t} + (V.\nabla)V + 2\Omega \times V + \Omega \times (\Omega \times r)\right] = -\nabla p + \text{div } S + J \times B + R \qquad \ldots\ldots(17)$$

$$\nabla . V = 0 \qquad \ldots\ldots(18)$$

$$\nabla . B = 0 \qquad \ldots\ldots.(19)$$

$$\nabla \times B = \mu_m J \qquad \ldots\ldots.(20)$$

$$\nabla \times E = -\frac{\partial B}{\partial t} \qquad \ldots\ldots.(21)$$

Where J is the current density, B is the total magnetic field, E is the total electric field, μ_m is the magnetic permeability, V=(u, v, w) is the velocity field, T is the Cauchy stress tensor, B is the total magnetic field such that B = B_0 + b, where B_0 is the applied magnetic field parallel to the z-axis and b is the induced magnetic field. The induced magnetic field is negligible such that B=(0, 0, B_0), the Lorentz force $J \times B = -\sigma B_0^2 V$, σ is is the electric conductivity of the fluid, ρ is the density of the fluid, and $\frac{D}{Dr}$ is the material derivate, r is the radial vector with $r^2 = x^2 + y^2$ and R is the Darcy resistance. The extra tensor S is given by

$$T = -pI + S$$

$$S + \lambda\left(\frac{DS}{Dt} - LS - SL^T\right) = \mu A \qquad \ldots\ldots(22)$$

where $-pI$ is the stress due to constraint of the impermeability, here p is the static fluid pressure, I is the identity tensor, μ is the viscosity of the fluid, λ is material time constant referred to as relaxation time, it is assumed that $\lambda \geq 0$. The first Rivlin-Ericksen Tensor A_1 is defined as $A_1=(\text{grad}V)+(\text{grad}V)^T$ ……(23)

It should be noted that this model includes the viscous Navier-Stokes fluid as a special Case for $\lambda=0$. Let us indicate the velocity component as $V(z, t) = (u, v, 0)$ ……..(24)

According to Tan and Masuoka, Darcy's resistance satisfies the following expression:

$$\left(I+\lambda\frac{\partial}{\partial t}\right)R=-\frac{\mu\emptyset}{k}\left(I+\lambda_r\frac{\partial}{\partial t}\right)V \qquad \text{…….(25)}$$

Where λ_r is the retardation time, ø is the porosity ($0 < ø < 1$) and k is the permeability of the porous medium, Since we have $\lambda_r=0$ hence

$$\left(I+\lambda\frac{\partial}{\partial t}\right)R=-\frac{\mu\emptyset}{k}V \qquad \text{…….. (26)}$$

Hence (17) reduces to

$$\rho\left[\frac{\partial u}{\partial t}-2\Omega\, v\right]=-\frac{\partial p}{\partial x}+\frac{\partial S_{xz}}{\partial z}-\sigma B_0^2 u+R_x \qquad \text{……. (27)}$$

$$\rho\left[\frac{\partial v}{\partial t}-2\Omega\, u\right]=-\frac{\partial p}{\partial y}+\frac{\partial S_{yz}}{\partial z}-\sigma B_0^2 v+R_y \qquad \text{…….. (28)}$$

Where R_x and R_y are x and y Components of Darcy's resistance in R.

$$\left(I+\lambda\frac{\partial}{\partial t}\right)S_{xz}=\mu\frac{\partial u}{\partial z} \text{ and } \left(I+\lambda\frac{\partial}{\partial t}\right)S_{yz}=\mu\frac{\partial v}{\partial z} \qquad \text{…… (29)}$$

The equations (27) and (28) reduces to

$$\rho\left[\frac{\partial u}{\partial t}-2\Omega\, v\right]=-\frac{\partial p}{\partial x}+\frac{\partial S_{xz}}{\partial z}-\sigma B_0^2 u-\frac{\mu\emptyset}{k}u \qquad \text{……..(30)}$$

$$\rho\left[\frac{\partial v}{\partial t}-2\Omega\, u\right]=-\frac{\partial p}{\partial y}+\frac{\partial S_{yz}}{\partial z}-\sigma B_0^2 v-\frac{\mu\emptyset}{k}v \qquad \text{……..(31)}$$

Let $q = u + iv$ and $\varsigma=x-iy$. Combining equation (30) and (31) we have

$$\rho\left[\frac{\partial q}{\partial t}-2i\Omega\right]=-\frac{\partial p}{\partial \varsigma}+\frac{\partial}{\partial z}(S_{xz}+iS_{yz})-\sigma B_0^2 q-\frac{\mu\emptyset}{k}q \qquad \text{…….(32)}$$

Since,

$$\left(I+\lambda\frac{\partial}{\partial t}\right)(S_{xz}+iS_{yz})=\mu\frac{\partial q}{\partial z} \qquad \text{…….(33)}$$

By substituting (33) in (32) we obtain the equation for governing the flow through porous medium with respect to the rotating frame, as

$$\left(I+\lambda\frac{\partial}{\partial t}\right)\frac{\partial q}{\partial z}+\left(2i\Omega+\frac{\sigma B_0^2}{\rho}+\frac{\nu\phi}{k}\right)\left(I+\lambda\frac{\partial}{\partial t}\right)q=-\frac{1}{\rho}\left(I+\lambda\frac{\partial}{\partial t}\right)\frac{\partial p}{\partial \varsigma}+\nu\frac{\partial^2 q}{\partial z^2} \qquad \text{…..(34)}$$

The boundary and initial conditions are

$$q = ae^{iwt} + be^{-iwt} \qquad t > 0,\ z = 0$$

$$q = 0, \quad t \neq 0, \quad z = l$$

$$q(z,t) = 0, \frac{dq\,(z,t)}{dt} = 0, \qquad t \leq 0 \quad for\ all\ z \qquad \text{..... (35)}$$

We introduce the following non-dimensional variables

$$z^*=\frac{z}{l},\ q^*=\frac{ql}{v},t^*=\frac{tv}{l^2},w^*=\frac{wl^2}{v},\varsigma^*=\frac{\varsigma}{l},p^*=\frac{pl^2}{pv^2}$$

The non=dimensional governing equations are (after dropping "*")

$$\left(I+\beta_1\frac{\partial}{\partial t}\right)\frac{\partial q}{\partial t}+\left(2iE^{-1}+M^2+D^{-1}\emptyset\right)+\left(I+\beta_1\frac{\partial}{\partial t}\right)q=\frac{1}{\rho}\left(I+\beta_1\frac{\partial}{\partial t}\right)P+\frac{\partial^2 q}{\partial z^2} \quad \text{.....(36)}$$

Where $M^2=\frac{\sigma\mu_e^2H_0^2l^2}{\rho v}$ (Hartmann number squared), $D^{-1}=\frac{l^2}{k}$ (Inverse Darcy Parameter), $E=\frac{v}{\Omega l^2}$ (Ekman Number), $\beta_1=\frac{\lambda v}{l^2}$ (material parameter related to relaxation time) and $P=-\frac{\partial p}{\partial \varsigma}$ (Pressure gradient).

The corresponding initial and boundary conditions are

$$q=ae^{i\omega t}+be^{-i\omega t},t>0,z=0$$
$$q=0,t\neq 0,z=l$$
$$q(z,t)=0,\frac{dq(z,t)}{dt}=0,t\leq 0, \text{ for all } z \qquad \text{..... (37)}$$

suppose the pressure is given by

$$P=\begin{cases}P_0+P_1e^{i\omega_1}, & t>0\\ 0 & t<0\end{cases} \qquad \text{.....(38)}$$

From (35), (37) and (38) we get

$$\frac{d^2\bar{q}}{dz^2}-\left[\beta_1 s^2+\left(1+\beta_1\left(M^2+2iE^{-1}+D^{-1}\phi\right)\right)s+\left(M^2+2iE^{-1}+D^{-1}\phi\right)\right]\bar{q}$$
$$=-\left(1+i\beta_1\omega_1\right)\frac{P_1}{s-i\omega_1}-\frac{P_0}{s} \qquad \text{.....(39)}$$

Solving equation (39) subjected to the conditions (37), we obtain

$$\bar{q}=\frac{a\cosh(\lambda_1 z)}{s-i\omega}+\frac{b\cosh(\lambda_1 z)}{s+i\omega}-\frac{P_1\left(1+i\beta_1\omega_1\right)\cosh(\lambda_1 z)}{\lambda_1^2(s-i\omega_1)}$$
$$-\frac{P_0\cosh(\lambda_1 z)}{\lambda_1^2 s}-\frac{a\cosh(\lambda_1)\cdot\sinh(\lambda_1 z)}{(s-i\omega)\cdot\sinh(\lambda_1)}-\frac{b\cosh(\lambda_1)\cdot\sinh(\lambda_1 z)}{(s+i\omega)\cdot\sinh(\lambda_1)}$$

$$+\frac{P_1\left(1+i\beta_1\omega_1\right)\mathrm{Cosh}(\lambda_1)\sinh(\lambda_1 z)}{\lambda_1^2(s-i\omega_1)\cdot\sinh(\lambda_1)}+\frac{P_0\cosh(\lambda_1)\cdot\sinh(\lambda_1 z)}{\lambda_1^2 s\cdot\sinh(\lambda_1)}$$

$$-\frac{P_1\left(1+i\beta_1\omega_1\right)\cdot\mathrm{Sinh}(\lambda_1 z)}{\lambda_1^2(s-i\omega_1)\cdot\sinh(\lambda_1)}-\frac{P_0\cdot\sinh(\lambda_1 z)}{\lambda_1^2\sinh(\lambda_1)}$$

$$+\frac{P_1\left(1+i\beta_1\omega_1\right)}{\lambda_1^2(s-i\omega_1)}+\frac{P_0}{\lambda_1^2 s(1+s\alpha)}$$

Where

$$\lambda_1^2=\beta_1 s^2+\left(1+\beta_1\left(M^2+2iE^{-1}+D^{-1}\varphi\right)\right)s+\left(M^2+2iE^{-1}+D^{-1}\varphi\right) \quad \ldots\ldots\ldots\ldots (40)$$

Taking the inverse Laplace Transformation in above equation

$$q=-\frac{P_0\ Cosh(b_0z)}{b_0^2}+\frac{P_0\ Cosh(b_0).Sinh(b_0z)}{b_0^2\ Sinh(b_0)}-\frac{P_0\ Sinh(b_0z)}{b_0^2\ Sinh(b_0)}+\frac{P_0}{b_0^2}$$
$$+a\left\{Cosh(b_1z)-\frac{Cosh(b_1).Sinh(b_1z)}{Sinh(b_1)}\right\}e^{i\omega t}$$

$$+b\left\{Cosh(b_2z)-\frac{Cosh(b_2).Sinh(b_2z)}{Sinh(b_2)}\right\}e^{-i\omega t}$$
$$+\frac{P_1(1+i\beta_1\omega_1)}{(i\omega_1-s_1)(i\omega_1-s_2)}\left\{-Cosh(b_4z)+\frac{Cosh(b_4).Sinh(b_4z)}{Sinh(b_4)}\right.$$
$$\left.-\frac{Sinh(b_4z)}{Sinh(b_4)}+1\right\}e^{i\omega_1 t}+\left\{-\frac{P_1(1+i\beta_1\omega_1).Cosh(b_3z)}{(s_1-s_2)(s_1-i\omega_1)}+\right.$$
$$+\frac{P_1(1+i\beta_1\omega_1).Cosh(b_3).Sinh(b_3z)}{(s_1-s_2)(s_1-i\omega_1).Sinh(b_3)}-\frac{P_1(1+i\beta_1\omega_1).Sinh(b_3z)}{(s_1-s_2)(s_1-i\omega_1)Sinh(b_3)}$$
$$+\frac{P_1(1+i\beta_1\omega_1)}{(s_1-s_2)(s_1-i\omega_1)}-\frac{P_0\ Cosh(b_3z)}{(s_1-s_2)s_1}+\frac{P_0\ Cosh(b_3).Sinh(b_3z)}{(s_1-s_2)(s_1).Sinh(b_3)}$$
$$\left.-\frac{P_0.Sinh(b_3z)}{(s_1-s_2)(s_1).Sinh(b_3)}+\frac{P_0}{(s_1-s_2)(s_1)}\right\}e^{s_1t}$$
$$+\left\{-\frac{P_1(1+i\beta_1\omega_1).Cosh(b_7z)}{(s_2-s_1)(s_2-i\omega_1)}\right.$$
$$+\frac{P_1(1+i\beta_1\omega_1).Cosh(b_7).Sinh(b_7z)}{(s_2-s_1)(s_2-i\omega_1).Sinh(b_7)}-\frac{P_1(1+i\beta_1\omega_1).Sinh(b_7z)}{(s_2-s_1)(s_2-i\omega_1)Sinh(b_7)}$$
$$+\frac{P_1(1+i\beta_1\omega_1)}{(s_2-s_1)(s_2-i\omega_1)}-\frac{P_0\ Cosh(b_7z)}{(s_2-s_1)s_2}+\frac{P_0\ Cosh(b_7).Sinh(b_7z)}{(s_2-s_1)s_2.Sinh(b_7)}$$
$$\left.-\frac{P_0.Sinh(b_7z)}{(s_2-s_1)s_2.Sinh(b_7)}+\frac{P_0}{(s_2-s_1)s_2}\right\}e^{s_2t}$$

$$+\sum_{n=0}^{\infty}\left\{-\frac{a.\ Cosh(b_6)Sinh(b_6z)}{(s_3-i\omega)(s_3-s_4)}-\frac{b.\ Cosh(b_6)Sinh(b_6z)}{(s_3+i\omega)(s_3-s_4)}\right.$$
$$+\frac{P_1(1+i\beta_1\omega_1).Cosh(b_6).Sinh(b_6z)}{b_6^2(s_3-s_4)(s_3-i\omega_1)}-\frac{P_1(1+i\beta_1\omega_1).Sinh(b_6z)}{b_6^2(s_3-s_4)(s_3-i\omega_1)}$$
$$\left.+\frac{P_0\ Cosh(b_6).Sinh(b_6z)}{b_6^2(s_3-s_4)(s_3)}-\frac{P_0\ Sinh(b_6z)}{b_6^2(s_3-s_4)(s_3)}\right\}e^{s_3t}$$
$$+\sum_{n=0}^{\infty}\left\{-\frac{a.\ Cosh(b_5)Sinh(b_5z)}{(s_4-i\omega)(s_4-s_3)}-\frac{b.\ Cosh(b_5)Sinh(b_5z)}{(s_4+i\omega)(s_4-s_3)}\right.$$
$$+\frac{P_1(1+i\beta_1\omega_1).Cosh(b_5).Sinh(b_5z)}{b_5^2(s_4-s_3)(s_4-i\omega_1)}-\frac{P_1(1+i\beta_1\omega_1).Sinh(b_5z)}{b_5^2(s_4-s_3)(s_4-i\omega_1)}$$
$$\left.+\frac{P_0\ Cosh(b_5).Sinh(b_5z)}{b_5^2(s_4-s_3)(s_4)}-\frac{P_0\ Sinh(b_5z)}{b_5^2(s_4-s_3)(s_4)}\right\}e^{s_4t} \qquad (2.26)$$

41)

The shear stresses on the upper and lower plates are given by

$$\tau_U=\left(\frac{dq}{dz}\right)_{z=1} \text{ and } \tau_L=\left(\frac{dq}{dz}\right)_{z=0} \qquad \text{.....(42)}$$

The solutions for the combined velocity q and q_p consists of three kinds of terms 1. Steady state 2. The quasi-steady state terms associated with non-torsional oscillations in the boundary 3. The transient terms involving exponentially varying time dependence. The analysis of transient terms indicates that this transient velocity decay exponentially in dimensionless time to of order i.e.,

$$t> \max\left\{\beta_1, \frac{M^2+D^{-1}\phi}{\left\{\left(M^2+D^{-1}\phi\right)^2+4E^{-2}\right\}^{\frac{1}{2}}}, \frac{I}{|S_3|}, \frac{I}{|S_4|}\right\}$$

This decay in the transient term depends on the non-dimensional parameters β_1, M, D^{-1} and E^{-1}. When these transient terms decay the ultimate velocity consists of steady and oscillatory components.

$$(q)_{steady}=-\frac{P_0 Cosh(b_0 z)}{b_0^2}+\frac{P_0 Cosh(b_0).Sinh(b_0 z)}{b_0^2 Sinh(b_0)}-\frac{P_0 Sinh(b_0 z)}{b_0^2 Sinh(b_0)}+\frac{P_0}{b_0^2} \qquad \text{.....(43)}$$

$$(q)_{Oscillary}=a\left\{Cosh(b_1 z)-\frac{Cosh(b_1).Sinh(b_1 z)}{Sinh(b_1)}\right\}e^{iwt}+b\left\{Cosh(b_2 z)-\frac{Cosh(b_2).Sinh(b_2 z)}{Sinh(b_2)}\right\}e^{-iwt}$$

.....(44)

The hyperbolic terms in the steady state solution give rise to a boundary layer on the upper plate whose dimension less thickness of order i.e.,

$$O\left(\frac{I}{|d_0|}\right)=O\left(\frac{I}{\sqrt{A^2+B^2}}\right)$$

$$A=\frac{I}{\sqrt{2}}\left\{\left(\left(\frac{M^2+D^{-1}\phi}{\beta_I}\right)^2+\frac{4E^{-2}}{\beta_I^2}\right)^{\frac{1}{2}}+\left(\frac{M^2+D^{-1}\phi}{\beta_I}\right)\right\}^{\frac{1}{2}}$$

$$B=\frac{I}{\sqrt{2}}\left\{\left(\left(\frac{M^2+D^{-1}\phi}{\beta_I}\right)^2+\frac{4E^{-2}}{\beta_I^2}\right)^{\frac{1}{2}}-\left(\frac{M^2+D^{-1}\phi}{\beta_I}\right)\right\}^{\frac{1}{2}}$$

This layer may be referred as modified Ekman-Harmann-Darcy layer, whose thickness is magnified by the relaxation time related to the Maxwell fluid. We may also note that the thickness of this layer reduces in the presence of a magnetic field and higher the magnetic field lesser its thickness. The decay time for hydro magnetic transient velocity ($M^2 \neq 0$) is always less than that of hydro dynamic transient solution ($M^2=0$) in both regions. Also we noticed that lesser the permeability of porous medium smaller the thickness of the layer and in fact the thickness directly proportional to square root of the permeability. A similar layer may be noticed near the lower plate which is proportional to square root of the product of the relaxation time of the Maxwell fluid and the permeability of the medium.

The steady oscillatory velocity represented in the above equation give rise to the modified Stokes-

Ekman-Darcy-Hartmann layers of order i.e., $\max\left\{\frac{1}{|d_1|},\frac{1}{|d_2|}\right\}$. Similar layer can be found near the lower plate with thickness order of $\max\left\{\frac{1}{|d_1|},\frac{1}{|d_2|}\right\}$. we now discuss the nature of the boundary layer when the frequency of oscillation is low (w <<I). In such case the the thickness of the layer reduces to $\frac{2}{(M^2+D^{-1}\phi+2iE^{-1})^{\frac{1}{2}}}$. In case of high frequency it reduces to $\frac{1}{w}\left(\frac{-1}{\beta_I^2}\right)^{\frac{1}{2}}$.

Now if we consider the porous medium to be a open rectangular channel, The geometry of the flow can be seen in Figure 1 (Frenet Frame Field system in Figure 2). From the previous studies, to describe the flow of fluid we have

$\vec{u}=u_b\vec{b},\ \vec{v}=v_b\vec{b}$ …….(45)

i.e. $u_s = u_n = 0$ and $v_s = v_n = 0$, where (u_s, u_n, u_b) and (v_s, v_n, v_b) are the velocity component of fluid and dust respectively. Now by virtue of the intrinsic decomposition of above studied equations we have,

$$0=-\frac{1}{\rho}\frac{\partial p}{\partial s}+\nu\left[u_b k_s\tau_s-2\sigma_n'\frac{\partial u_b}{\partial n}\right] \quad \text{……(46)}$$

$$0=-\frac{1}{\rho}\frac{\partial p}{\partial n}+\nu\left[u_b k_n'\sigma_n'-2\tau_s\frac{\partial u_b}{\partial s}\right] \quad \text{……(47)}$$

$$\frac{\partial u_b}{\partial t}=-\frac{1}{\rho}\frac{\partial p}{\partial b}+\nu\left[\frac{\partial^2 u_b}{\partial s^2}+\frac{\partial^2 u_b}{\partial n^2}-C_r u_b\right]+\frac{kN}{\rho}(v_b-u_b)-\frac{\mu}{\eta}u_b \quad \text{.....(48)}$$

$$v_b^2 k^{''} b=0 \quad \text{.....(49)}$$

$$\frac{\partial v_b}{\partial t}=\frac{k}{m}(u_b-v_b) \quad \text{..... (50)}$$

Where $C_r=(\sigma_n'^2+\tau_s^2)$ is curvature number. Since the choice $v_b = 0$ is impossible because then it will mean that flow did not existed, hence, from (49) we have $k_b^{''}=0$ and this suggests that curvature of streamline along binormal direction is zero. Equation (48) and (50) are to be solved as per following conditions

Initial Condition : *at* t=0; $u_b(s,n,0)$=0, $v_b(s,n,0)$=0

Boundary Condition: *for* t>0; $u_b(\pm d,n,t)$=0, $v_b(\pm d,n,t)$=0 *at* s=±d,

$$u_b(s,h,t)=g(t),v_b(s,h,t)=g(t) \qquad at\ n=h$$

$$\frac{\partial u_b}{\partial n}=0,\ \frac{\partial v_b}{\partial n}=0, \qquad at\ n=0$$

Let us consider the following non-dimensional quantities

$$u_b^*=u_b\,h/U,v_b^*=v_b\,h/U,s^*=s/h,n^*=n/h,b^*=b/h,t^*=tU/h^2,\rho^*=\rho h^2/\rho U^2$$

Where U is the characteristic velocity.

Hence (48) and (60) reduces to

$$\frac{\partial u_b}{\partial t}=-\frac{\partial p}{\partial b}+\frac{h}{Re}\left[\frac{\partial^2 u_b}{\partial s^2}+\frac{\partial^2 u_b}{\partial n^2}-h^2 C_r u_b\right]+\frac{kNh^2}{\rho U}(v_b-u_b)-\frac{\mu h^2}{\eta U}u_b \quad \text{……(51)}$$

$$\frac{\partial v_b}{\partial t}=\frac{kh^2}{mU}(u_b-v_b) \quad \text{…….(52)}$$

Where Re = Uh/v the Reynold's number. The initial and boundary conditions are

at t=0; u_b=0, v_b=0

for t>0; u_b=0, v_b=0 *at* s=±d/h,

$u_b=g(t),v_b=g(t)$ *at* n=1

$\frac{\partial u_b}{\partial s}=0,\ \frac{\partial v_b}{\partial s}=0, \qquad at\ n=0$

Let $\wp(t)$ be the time dependent pressure gradient for t > 0, so we have

$-\frac{\partial p}{\partial b}=\wp(t)$. Laplace transformation for u_b and v_b can be defined as

$\bar{u}=\int_0^\infty e^{-Xt}u_b dt \ and\ \bar{v}=\int_0^\infty e^{-Xt}v_b dt$ .....(53)

From (51), (52) and (53) after utilizing the initial and boundary conditions, we have,

$X\bar{u}=P(X)+\frac{h}{Re}\left[\frac{\partial^2\bar{u}}{\partial s^2}+\frac{\partial^2\bar{u}}{\partial n^2}-h^2C_r\bar{u}\right]+\frac{lh^2}{\tau U}(\bar{v}-\bar{u})-\frac{\mu h^2}{\eta U}\bar{u}$ .....(54)

$X\bar{v}=\frac{h^2}{\tau U}(\bar{u}-\bar{v})$ ..... (55)

The boundary conditions now reduces to

$for\ t>0;\ \bar{u}=0,\ \bar{v}=0\ at\ s=\pm d/h,$ ..... (56)

$\bar{u}=G(X),\bar{v}=G(X) \qquad at\ n=1$

$\frac{\partial\bar{u}}{\partial n}=0,\ \frac{\partial\bar{v}}{\partial n}=0, \qquad at\ n=0$

Where $l=\frac{mN}{\rho},\tau=\frac{m}{k}$ and G(X) and P(X) are Laplace Transformation for g(t) and $\wp(t)$ respectively. Equation (55) implies that

$\bar{v}=\frac{h^2\bar{u}}{h^2+X\tau U}$ .....(57)

Hence, we obtain

$\frac{d^2\bar{u}}{ds^2}+\frac{d^2\bar{u}}{dn^2}-Q^2\bar{u}=-\frac{Re}{h}P(X)$ ..... (58)

Where $Q^2=\left(C_rh^2+\frac{Re\mu h}{\eta U}+\frac{ReX}{h}+\frac{RelhX}{X\tau U+h^2}\right)$

Taking finite Fourier sine, (57) and (58) becomes

$\frac{d^2\overline{u_F}}{dn^2}-M^2\overline{u_F}=-\frac{Re}{h}P_F(X)$ ..... (59)

$\bar{v_F}=\frac{h^2\overline{u_F}}{h^2+X\tau U}$ ..... (60)

Boundary condition becomes

$for\ t>0;\ \overline{u_F}=0,\ \bar{v_F}=0\ at\ s=\pm d/h,$ .....(61)

$\overline{u_F}=G_F(X),\bar{v_F}=G_F(X) \qquad at\ n=1$

$\frac{\partial\overline{u_F}}{\partial n}=0,\ \frac{\partial\bar{v_F}}{\partial n}=0, \qquad at\ n=0$

Where $M^2=\left(C_rh^2+\frac{Re\mu h}{\eta U}+\frac{ReX}{h}+\frac{RelhX}{X\tau U+h^2}+\frac{r^2\pi^2h^2}{d^2}\right)$ and $P_F(X)$ and $G_F(X)$ are Fourier sine transformation of P(X) and G(X) repectively

$\overline{u_F}=\int_0^{d/h}\bar{u}\sin\left(\frac{\tau\pi s}{d/h}\right)ds\ and\ \bar{v_F}=\int_0^{d/h}\bar{v}\sin\left(\frac{\tau\pi s}{d/h}\right)ds$ ..... (62)

In case of motion for a finite time we take $g(t)=u_0[H(t)-H(t-T)]$ and $\wp(t)=p_0[H(t)-H(t-T)]$ where $\delta(t)$ is Heaviside's unit step function and u_0 and p_0 are constant, (59) and (60) now becomes

$\bar{u}_F=\left[\frac{(1-e^{-XT})(1-(-1)^r)u_0d}{Xhr\pi}\right]\left[\frac{\cosh(Mn)}{\cosh(M)}\right]$

$+\left[\frac{(1-e^{-XT})(1-(-1)^r)Rep_0d}{Xh^2M^2r\pi}\right]\left[1-\frac{\cosh(Mn)}{\cosh(M)}\right]$ .....(63)

$$\bar{v}_F=\left[\frac{h^2}{h^2+X\tau U}\right]\left\{\left[\frac{\left(1-e^{-XT}\right)(1-(-1)^r)u_0 d}{Xr\pi h}\right]\left[\frac{\cosh(Mn)}{\cosh(M)}\right]+\left[\frac{\left(1-e^{-XT}\right)(1-(-1)^r)\mathrm{Re}p_0 d}{Xh^2M^2r\pi}\right]\left[1-\frac{\cosh(Mn)}{\cosh(M)}\right]\right\} \quad \ldots\ldots\ldots\ldots(64)$$

Inverse finite Fourier sine transform of equations (63) and (64), using the calculus of residues,we obtain

$$\bar{u}=\left\{\frac{2\left(1-e^{-XT}\right)}{X\pi}\left[u_0\sum_{r=1}^{\infty}\left(\frac{\cosh(Mn)}{\cosh(M)}\right)+\frac{\mathrm{Re}p_0}{h}\sum_{r=1}^{\infty}\frac{1}{M^2}\left(1-\frac{\cosh(Mn)}{\cosh(M)}\right)\right]\right\}\left\{\frac{(1-(-1)^r)}{r}\sin\left(\frac{r\pi s}{d/h}\right)\right\}$$

$$\bar{v}=\left\{\frac{2h\left(1-e^{-XT}\right)}{X\pi\left(h^2+X\tau U\right)}\left[hu_0\sum_{r=1}^{\infty}\left(\frac{\cosh(Mn)}{\cosh(M)}\right)+\mathrm{Re}p\sum_{r=1}^{\infty}\frac{1}{M^2}\left(1-\frac{\cosh(Mn)}{\cosh(M)}\right)\right]\right\}\left\{\frac{(1-(-1)^r)}{r}\sin\left(\frac{r\pi s}{d/h}\right)\right\}$$

Inverse Laplace transform of $\bar{u}$ and $\bar{v}$ are

$$u_b=2u_0h\sum_{r=1}^{\infty}\sum_{j=0}^{\infty}\frac{(-1)^j(2j+1)(1-(-1)^r)}{r}\cos\left(\frac{(2j+1)\pi}{2}n\right)\sin\left(\frac{r\pi s}{d/h}\right)\times\left[\frac{e^{y_1t}\left(1-e^{-y_1T}\right)\left(h^2+y_1\tau U\right)^2}{y_1Re\left[\left(h^2+y_1\tau U\right)^2+lh^4\right]}+\frac{e^{y_2t}\left(1-e^{-y_2T}\right)\left(h^2+y_2\tau U\right)^2}{y_2Re\left[\left(h^2+y_2\tau U\right)^2+lh^4\right]}\right]$$

$$+\frac{8Rep_0}{\pi^2}\sum_{r=1}^{\infty}\sum_{j=0}^{\infty}\frac{(-1)^j(1-(-1)^r)}{r(2j+1)}\cos\left(\frac{(2j+1)\pi}{2}n\right)\sin\left(\frac{r\pi s}{d/h}\right)\times\left[\frac{e^{y_1t}\left(1-e^{-y_1T}\right)\left(h^2+y_1\tau U\right)^2}{y_1Re\left[\left(h^2+y_1\tau U\right)^2+lh^4\right]}+\frac{e^{y_2t}\left(1-e^{-y2T}\right)\left(h^2+y_2\tau U\right)^2}{y_2Re\left[\left(h^2+y_2\tau U\right)^2+lh^4\right]}\right]$$

$$v_b=2u_0h^3\sum_{r=1}^{\infty}\sum_{j=0}^{\infty}\frac{(-1)^j(2j+1)(1-(-1)^r)}{r}\cos\left(\frac{(2j+1)\pi}{2}n\right)\sin\left(\frac{r\pi s}{d/h}\right)\times\left[\frac{e^{y_1t}\left(1-e^{-y_1T}\right)\left(h^2+y_1\tau U\right)}{y_1Re\left[\left(h^2+y_1\tau U\right)^2+lh^4\right]}+\frac{e^{y_2t}\left(1-e^{-y_2T}\right)\left(h^2+y_2\tau U\right)}{y_2Re\left[\left(h^2+y_2\tau U\right)+lh^4\right]}\right]$$

$$+\frac{8Rep_0h^2}{\pi^2}\sum_{r=1}^{\infty}\sum_{j=0}^{\infty}\frac{(-1)^j(1-(-1)^r)}{r(2j+1)}\cos\left(\frac{(2j+1)\pi}{2}n\right)\sin\left(\frac{r\pi s}{d/h}\right)\times\left[\frac{e^{y_1t}\left(1-e^{-y_1T}\right)\left(h^2+y_1\tau U\right)}{y_1Re\left[\left(h^2+y_1\tau U\right)^2+lh^4\right]}+\frac{e^{y_2t}\left(1-e^{-y_2T}\right)\left(h^2+y_2\tau U\right)}{y_2Re\left[\left(h^2+y_2\tau U\right)^2+lh^4\right]}\right]$$

The expression for shear stress at $n = 1$ and $s = \pm d/h$ are respectively given by:

$$D_1=\mu u_0\pi h\sum_{r=1}^{\infty}\sum_{j=0}^{\infty}\left[\frac{((-1)^r-1)(2j+1)^2}{r}\right]\sin\left(\frac{r\pi s}{d/h}\right)\times\left[\frac{e^{y_1t}\left(1-e^{-y_1T}\right)\left(h^2+y_1\tau U\right)^2}{y_1Re\left[\left(h^2+y_1\tau U\right)^2+lh^4\right]}+\frac{e^{y_2t}\left(1-e^{-y_2T}\right)\left(h^2+y_2\tau U\right)^2}{y_2Re\left[\left(h^2+y_2\tau U\right)^2+lh^4\right]}\right]$$

$$+\frac{4\mu Rep_0}{\pi}\sum_{r=1}^{\infty}\left[\frac{(-1)^r-1}{r}\right]\sin\left(\frac{r\pi s}{d/h}\right)\times\left[\frac{e^{y_1t}\left(1-e^{-y_1T}\right)\left(h^2+y_1\tau U\right)^2}{y_1Re\left[\left(h^2+y_1\tau U\right)^2+lh^4\right]}+\frac{e^{y_2t}\left(1-e^{-y_2T}\right)\left(h^2+y_2\tau U\right)^2}{y_2Re\left[\left(h^2+y_2\tau U\right)^2+lh^4\right]}\right]$$

$$D_{\pm d/h}= \frac{2\mu u_0 h^2\pi}{d}\sum_{r=1}^{\infty}\sum_{j=0}^{\infty}\left[(-1)^j((-1)^r-1)(2j+1)\right]\cos\left(\frac{(2j+1)\pi}{2}n\right)$$

$$\times \left[\frac{e^{y_1 t}(1-e^{-y_1 T})\left(h^2+y_1\tau U\right)^2}{y_1 Re\left[\left(h^2+y_1\tau U\right)^2+lh^4\right]}+\frac{e^{y_2 t}(1-e^{-y_2 T})\left(h^2+y_2\tau U\right)^2}{y_2 Re\left[\left(h^2+y_2\tau U\right)^2+lh^4\right]}\right]$$

$$+\frac{8\mu Rep_0 h}{\pi d}\sum_{r=1}^{\infty}\sum_{j=0}^{\infty}\left[\frac{(-1)^j((-1)^r-1)}{2j+1}\right]\cos\left(\frac{(2j+1)\pi}{2}n\right)$$

$$\times\left[\frac{e^{y_1 t}(1-e^{-y_1 T})\left(h^2+y_1\tau U\right)^2}{y_1 Re\left[\left(h^2+y_1\tau U\right)^2+lh^4\right]}+\frac{e^{y_2 t}(1-e^{-y_2 T})\left(h^2+y_2\tau U\right)^2}{y_2 Re\left[\left(h^2+y_2\tau U\right)^2+lh^4\right]}\right]$$

In the above equation

$$K_1=\sqrt{c_r h^2+\frac{Re\mu h}{\eta U}-\frac{Re\omega}{h}-\frac{Rel\omega h}{h^2-\omega\tau U}+\frac{r^2\pi^2h^2}{d^2}}$$

$$y_1 = -R_1+R_2, y_2=-(R_1+R_2), R_1=B_1+B_2, y_2=-(R_1+R_2)$$

$$B_1 = \frac{d^2\eta U h^2(c_r hU\tau+Re)+Reh^2Ud^2(\mu\tau+l\eta)}{2Re\eta U^2d^2\tau}$$

$$B_2 = \frac{r^2\pi^2h^3\eta U^2\tau+\pi^2\eta U^2hd^2\tau(j^2+j+1/4)}{2Re\eta U^2d^2\tau}$$

$$\alpha = 4\mathrm{Re}\eta U^2d^2\tau\left[h^4d^2(C_r h\eta u+Re\mu)+r^2\pi^2h^5\eta U\right.$$

$$\left.+\pi^2\eta Uh^3d^2\left(j^2+j+1/4\right)\right], R_2=\frac{\sqrt{R_1^2-\alpha}}{2Re\eta U^2d^2\tau}$$

RESULTS AND DISCUSSIONS :

The graphical presentations and tables are helpful in this analysis. Initially the present methodology is verified by comparing a result with the previous literature in the absence of newly introduced parameters. It is evident from Fig. 3 that a good conformity is noticed among the present and previous results in the comparison. Figs. 4, 5 exhibit the velocity profiles with the effect of Grashof number for heat and mass transfer. It is noticed that the fluid velocity increases under the increment of both the cases of Grashof number and modified Grashof number. This is due to the presence of thermal and solutal buoyancy which has the tendency of leading to an increase in the velocity. The variation in velocity under diffusion thermo effect is depicted in Fig. 6. The velocity grows when the values of Dufour number increases. The effect of magnetic parameter on primary velocity and secondary velocity is illustrated in the Figs. 7, 8. The velocity falls down when the values of magnetic parameter increases. This is due to the application of transverse magnetic field, which has the tendency of reducing the velocity. This drag force is called the Lorentz force. The impact of porosity parameter on primary velocity and secondary velocity is presented in the Figs. 9, 10. The velocity grows for increasing values of porosity parameter. Figs. 11, 12 depict the changes in primary and secondary velocities under the influence of rotation parameter. The primary velocity falls down for enhancing values of rotation parameter but an opposite nature is observed in the case of secondary velocity. The variation in the primary velocity with the impact of thermal diffusion is shown in Fig. 13 and an improvement in the velocity is noticed. The consequence of Prandtl number on fluid temperature is shown in Fig. 14. It is evident that the temperature falls down when the value of Prandtl number is increased. The basic reason behind this nature is that the

reduced fluid velocity would mean heat is not convected readily and hence the surface temperature decreases. The consequence in temperature in the existence of heat source and sink is exhibited in Fig.15. It reveals that the temperature falls down under the influence of heat absorption parameter whereas the temperature grows in the presence of heat generation. The fact behind this effect is that the heat absorption causes a decrease in the kinetic energy as well as the thermal energy of the fluid. Hence the momentum and thermal boundary layers get thinner in case of heat absorbing fluids. Improved values of radiation parameter lead to a lessening in the temperature which is experienced from Fig.16. Fig. 17 reveals that the temperature becomes thinner under the existence of thermal diffusion. The variations in temperature due to the impact of diffusion thermo effect are depicted in Fig. 18. The temperature grows for enhancing values of Dufour number. Fig. 19 illustrates the impact of Schmidt number on species concentration. It is noticed that as the Schmidt number increases, there is a decreasing trend in the concentration field. Not much of significant contribution of Schmidt number is observed far away from the plate. The variation in species concentration in the presence of chemical reaction is exhibited in Fig. 20. The existence of chemical reaction leads to a decrease the concentration of the fluid. Fig. 21 reveals that the concentration of the fluid enhances under the existence of thermal diffusion. The variations in skin friction under the impact of the physical parameters are observed with the help of numerical values from Table 34.

The primary skin friction as well as the secondary skin friction decreases for increased values of Grashof number and modified Grashof number but a reverse trend is seen in the case of magnetic field parameter and porosity parameter. The primary skin friction increases under the influence of rotation parameter and the secondary skin friction enhances when the values of rotation parameter are increased. Table 33 presents the effects of Prandtl number, heat source parameter, radiation parameter and Dufour number on skin friction and Nusselt number. The primary skin friction as well as the secondary skin friction decreases for increased values of radiation parameter but an opposite nature is found in the case of diffusion thermo effect. The rate of heat transfer rises on increasing the values of the Prandtl number, the radiation parameter and the Dufour number and on decreasing the values of the heat source parameter. Table 35 gives numerical illustration of the changes in Sherwood number. The Sherwood number increases under the influence of chemical reaction and Schmidt number whereas an opposite trend is noticed in the case of Soret number. The flow of the fluid and dust particles are drawn as in figures 22 to 33, which are paraboloid in nature. Figures 34 and 35 depict the effect of the visco-elastic parameter α and the shear thinning parameter β on the blood flow, respectively. The nature of the graph for blood velocity with varying cross flow Reynold's number or the suction parameter is shown in Fig. 36. Figure 37 illustrates that the fluid velocity decreases with an increase in the magnetic parameter Ha. This result can be implemented as a control measure in handling blood flow during surgeries and other cases where the biological fluid flow needs to be checked. There is a corresponding rise in the fluid velocity as the porous permeability parameter, Da rises as

observed in Fig. 38. This reveals the fact that homogeneity of the channel can be achieved by increasing the porous permeability of the medium. Further, it is observed from Fig. 39 that there is an increase in the fluid temperature with increasing Da, which is a consequence of the increased diffusion of heat within the channel. The variation in the temperature with varying visco-elastic parameter, α and third grade fluid material parameter, β is shown in Fig. 40 and Fig. 41, respectively. The curves in these figures convey that there is a rise in temperature when the values of these parameters are raised. As the

suction parameter, ReC increases, temperature of the fluid increases which is given in Fig. 42.

The response of fluid temperature to the magnetic field parameter, Ha is represented in Fig. 43. It is observed that an increase in the magnetic field intensity results in the increase in temperature of the fluid which is due to Ohmic heating phenomenon. The effect of Prandtl number and Brinkman number on the temperature profile are pre- sented in Fig.44 and Fig.45, respectively. Figure 46[(a), (b), (c), (d)] shows the Volume rate of flow for the flow Parameters for α, β, Da and Ha respectively. While Figure 47[(a), (b), (c), (d)] show the Wall shear stress for different flow parameters for α, β, Da and Ha respectively. Figure 48is about the variation of Nu with Pr and Figure 49 shows the variation of Nu with t_x. We may note that the magnitude of the velocity component *u* and *v* enhances everywhere in the flow field with increase in the Ekman number *E* (fig.54 and fig.74). The resultant velocity enhances throughout the fluid region with increase in the Ekman number *E*. Next we have seen that the effect of the magnetic field on the flow from fig.59 and fig.79. The magnitude of the velocity component *u* reduces and the velocity component *v* increases with increase in the Hartmann number *M*. However, the resultant velocity reduces throughout the fluid region with increase in the intensity of the magnetic field (the Hartmann number *M*). The fig.64 and fig.84 represents the velocity profiles with different variation in the inverse Darcy parameter D^{-1}. We find that the magnitude of *u* reduces with decrease in the permeability of the porous medium, while the magnitude of *v* experiences a slight enhancement with increase in the inverse Darcy parameter D^{-1}. It is interesting to note that lesser the permeability of the porous medium lower the magnitude of the resultant velocity. i.e., the resultant velocity reduces throughout the fluid region with increase in the inverse Darcy parameter D^{-1}. Both the velocity components *u* and *v* enhances with increase in the relaxation time entire fluid region. These displayed in the fig.69 and fig.89. The corresponding curves related to all these parameters can be observed in details in figure 50 to 89, while the corresponding data can be found in Table 1 to Table 32. The resultant velocity enhances throughout the fluid region with increase in the relaxation time. The shear stresses on the upper and lower plates have been calculated with reference to variations in the governing parameters and are tabulated in the (Table 36- Table 39). On the upper plate the magnitude of stresses τ_x enhances with increase in E, M and β_1, while it reduces with increase in the inverse Darcy parameter D^1. The magnitude of the stresses τ_y enhances with increase in for all governing parameters E, M, D^1 and β_1(Table 36-Table 37). On the lower plate the magnitude of the stresses τ_x and τ_y enhances with increase in E, M, and β_1, while thsed reduces with increase in the inverse Darcy parameterD^1 (Table 38-Table 39).

CONCLUSIONS:

The present study delivers a detailed parametric and numerical exploration of unsteady Newtonian fluid flow in rotating porous channels, incorporating the coupled effects of magnetohydrodynamics, thermal radiation, Soret–Dufour diffusion, chemical reactions, and heat–mass transfer. Key findings demonstrate that:

- Rotation enhances primary flow velocity while attenuating secondary motion, highlighting the critical role of Ekman number in guiding flow control strategies for rotating machinery and bioreactor design.
- Magnetic fields uniformly suppress resultant velocities through Lorentz forces, providing a viable mechanism for regulating fluid transport in MHD-based heat exchangers and biomedical devices.
- Porosity promotes fluid acceleration, indicating that tailored permeability distributions can optimize throughput in packed-bed reactors and filtration systems.
- Thermodiffusion (Soret effect) elevates species concentration, whereas chemical reactions deplete it, underscoring the necessity to balance thermal gradients and reactive kinetics in environmental modeling and microfluidic reactors.
- Heat transfer intensifies with increasing Prandtl number, radiation parameter, and Dufour effect but diminishes under heat-absorption conditions—offering design guidelines for thermal management in rotating heat sinks and solar energy collectors.
- Skin friction behavior is parameter-sensitive: rotation boosts wall shear stress, while magnetic and radiation effects generally reduce it. These insights inform advanced coatings and surface treatments to minimize drag in porous rotating systems.

Beyond summarizing flow characteristics, this work establishes a robust finite-difference framework for solving high-dimensional, coupled boundary-value problems in rotating porous media. Its versatility and modular structure make it readily extensible to:

- Non-Newtonian fluids and multi-component suspensions, enabling direct application to blood flow dynamics and pollutant dispersion.
- Three-dimensional geometries and transient forcing functions, facilitating exploration of pulsatile flows in biomedical implants and rotating detonation engines.
- Optimization studies coupling fluid–structure interactions, supporting the design of adaptive porous rotors and smart filtration membranes.

By elucidating the interplay of rotation, magnetism, porosity, and thermal–chemical transport, the paper provides a foundation for future analytical and computational research. It offers clear guidance for experimental validation, encourages development of hybrid numerical–analytical methods, and paves the way for machine-learning–enhanced parameter estimation in complex rotating systems. Consequently, this contribution stands as a valuable resource for engineers and scientists engaged in next-generation MHD technologies, chemical reactors, and biofluid applications.

GRAPHS AND TABLES

GRAPHS :

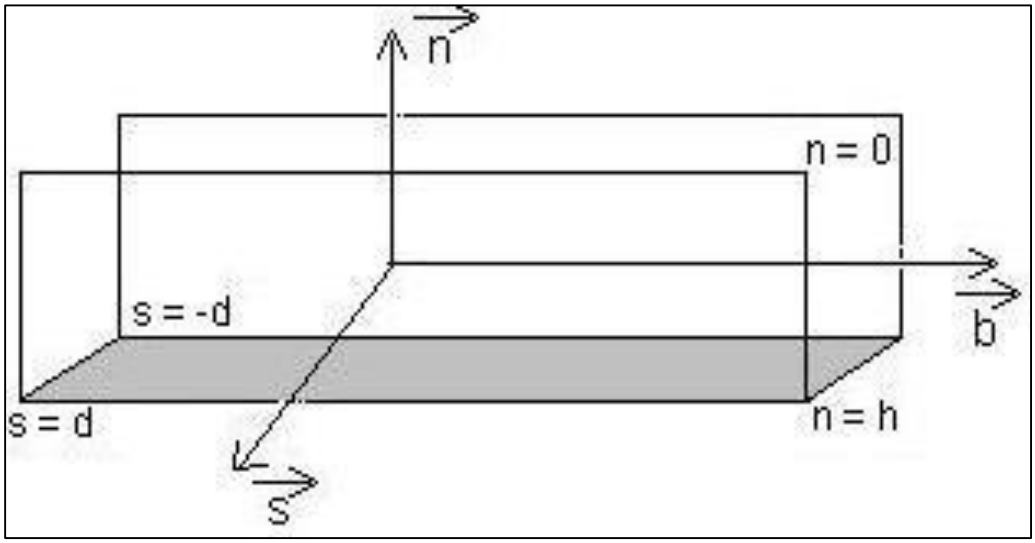

Figure 1 : Pictorial representation of the Geometry of the flow through a porous rectangle channel.

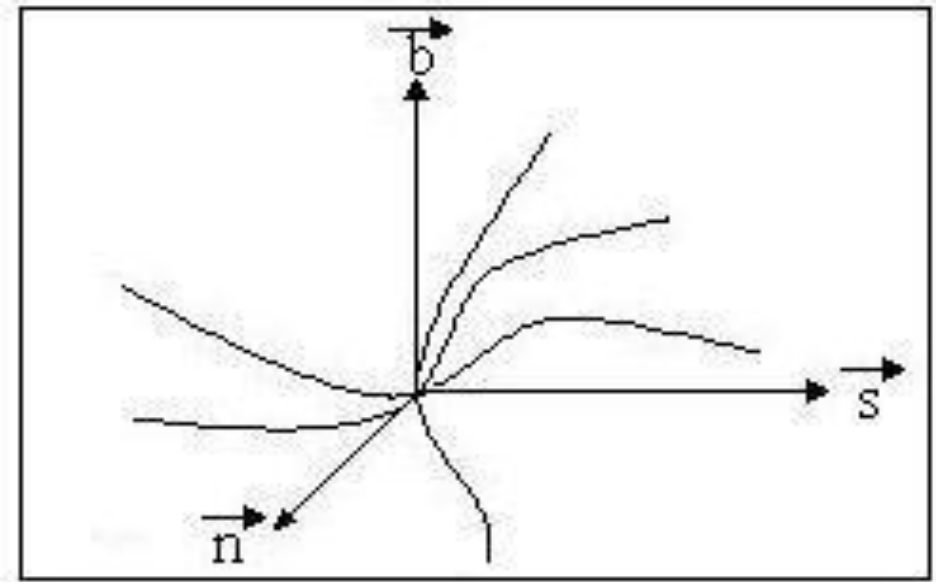

Figure 2: Pictorial representation of Frenet Frame Field System

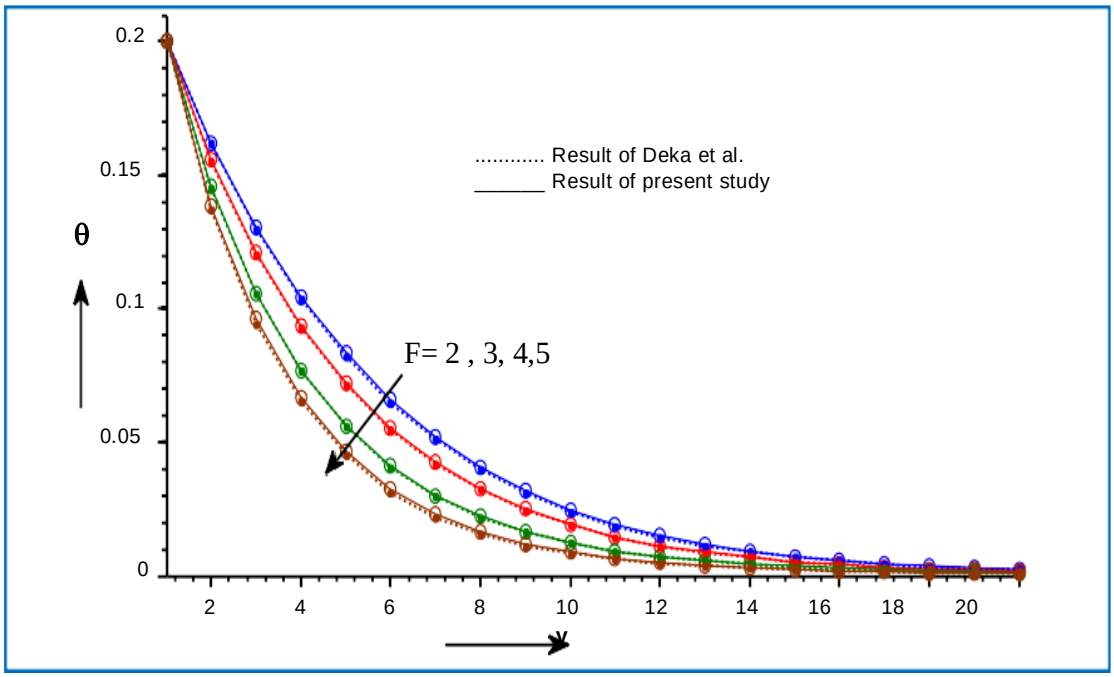

Figure 3 : Comparison of our results with that of Deka et al.

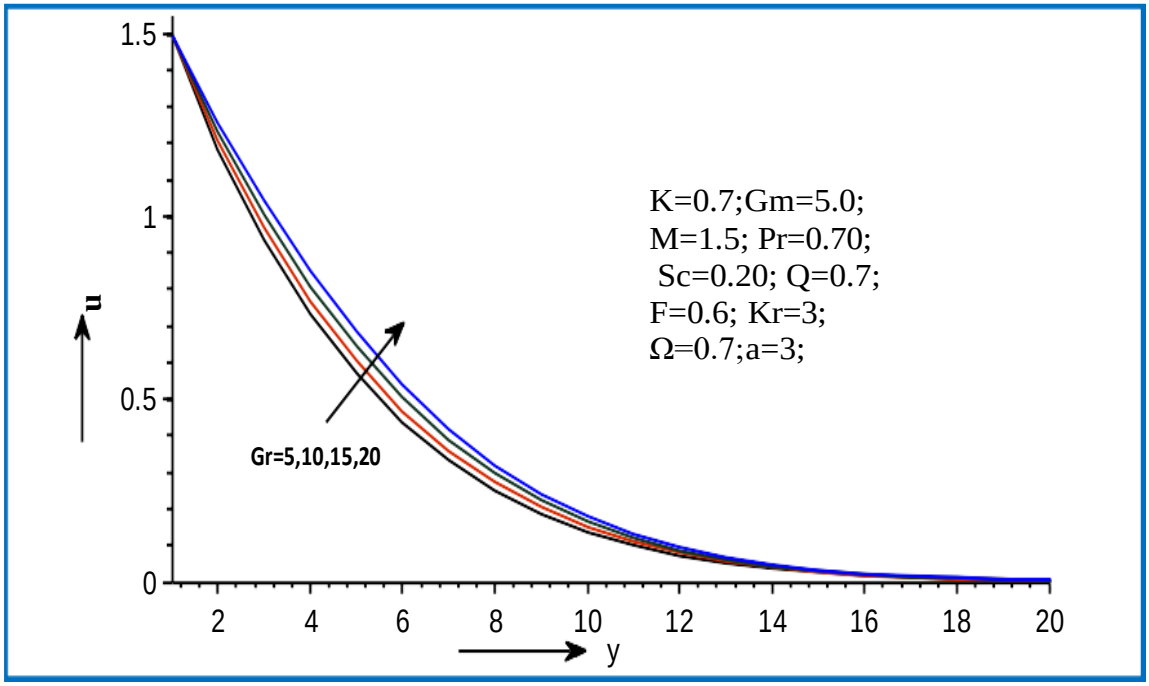

Figure 4 : Illustration of the effect of Grashof number on the primary velocity.

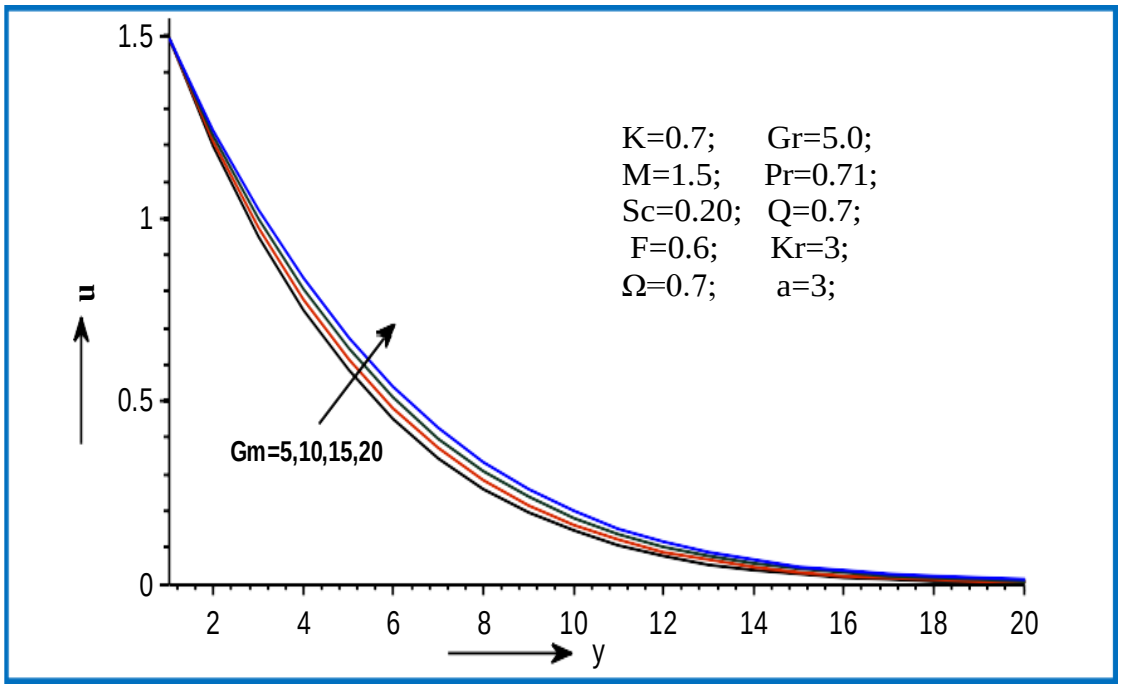

Figure 5 : Illustration of the effect of the modified Grashof number on the primary velocity

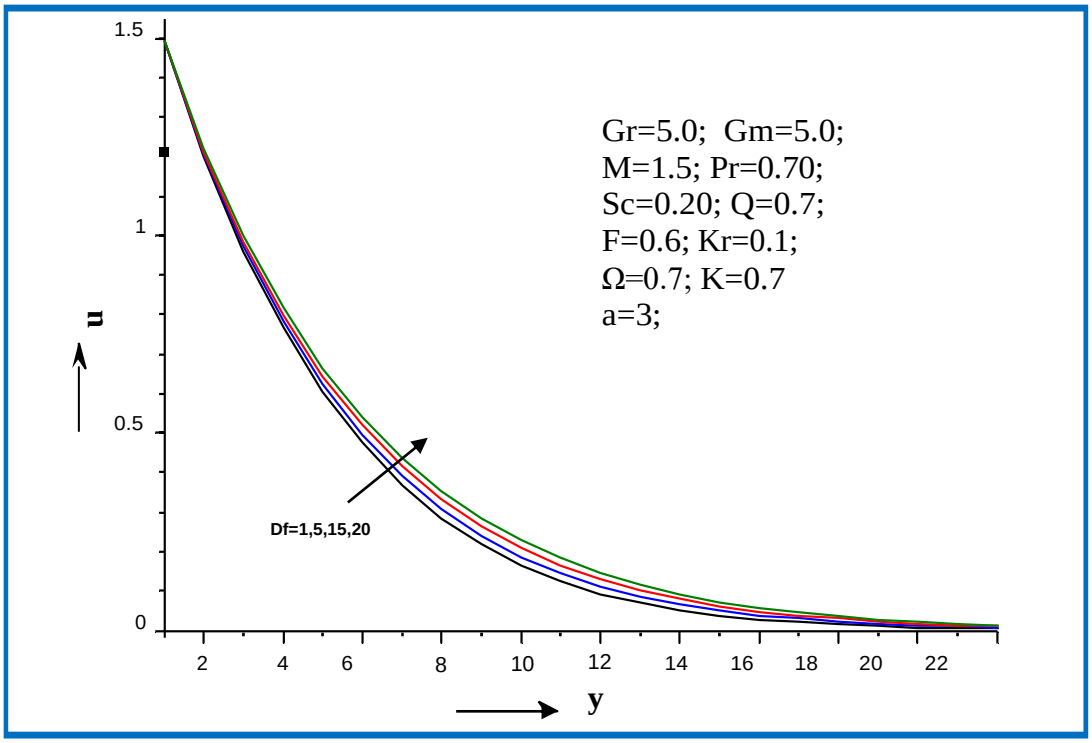

Figure 6 : Illustration of the effect of the Dufour number on the primary velocity

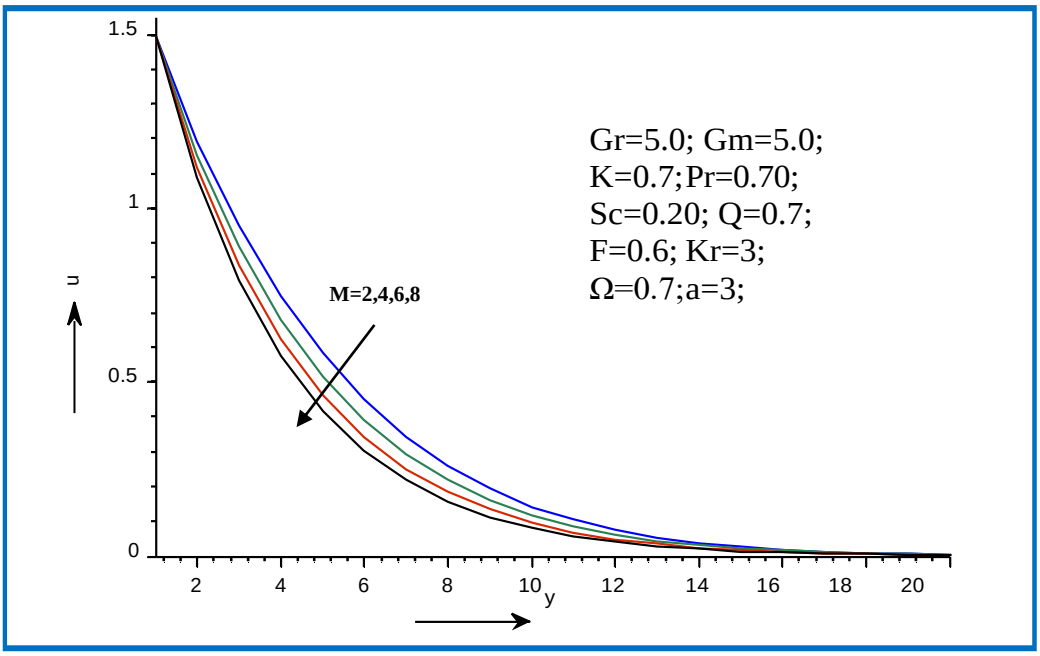

Figure 7 : Illustration of the effect of the magnetic parameter on the primary velocity

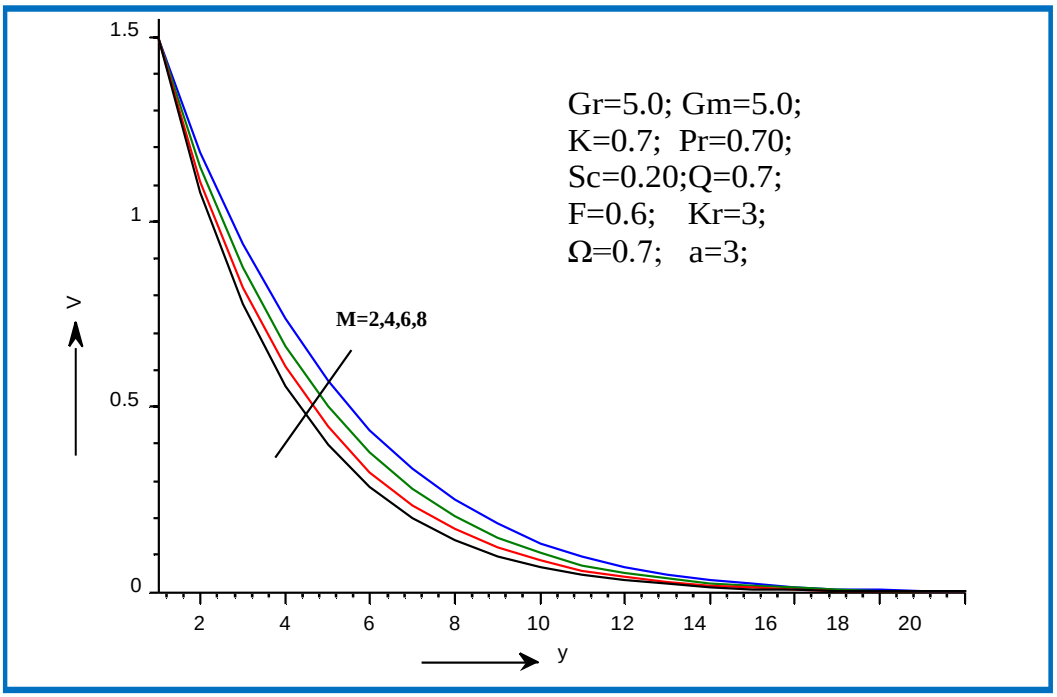

Figure 8: Illustration of the effect of the magnetic parameter on the secondary velocity

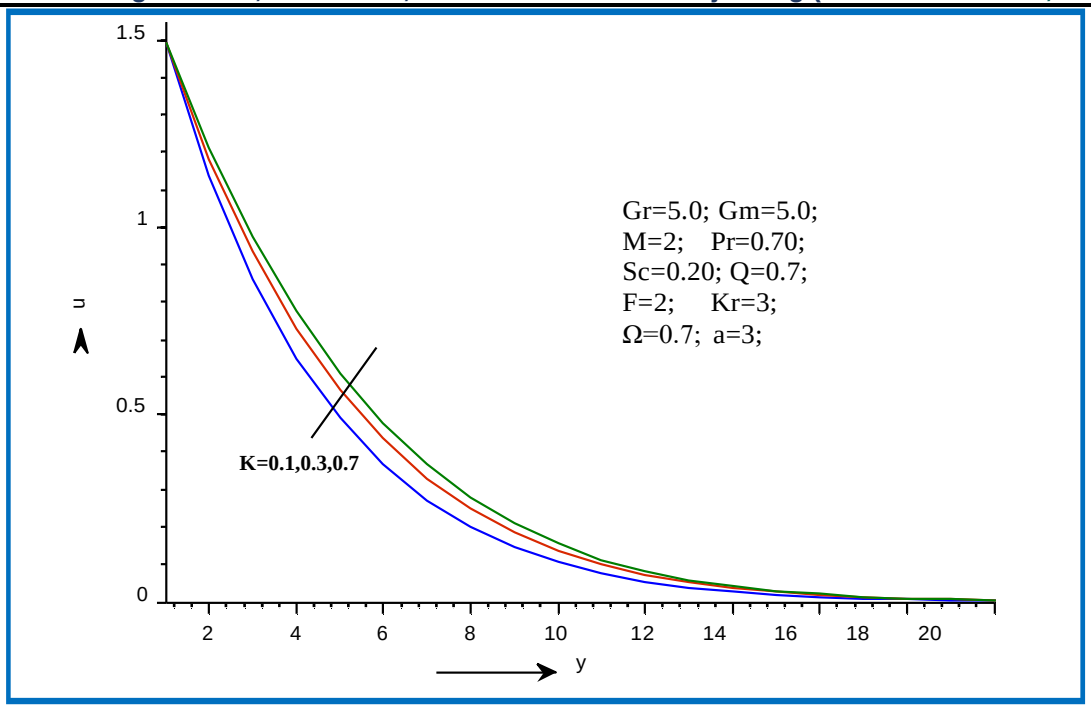

Figure 9: Illustration of the effect of the porosity parameter on the primary velocity

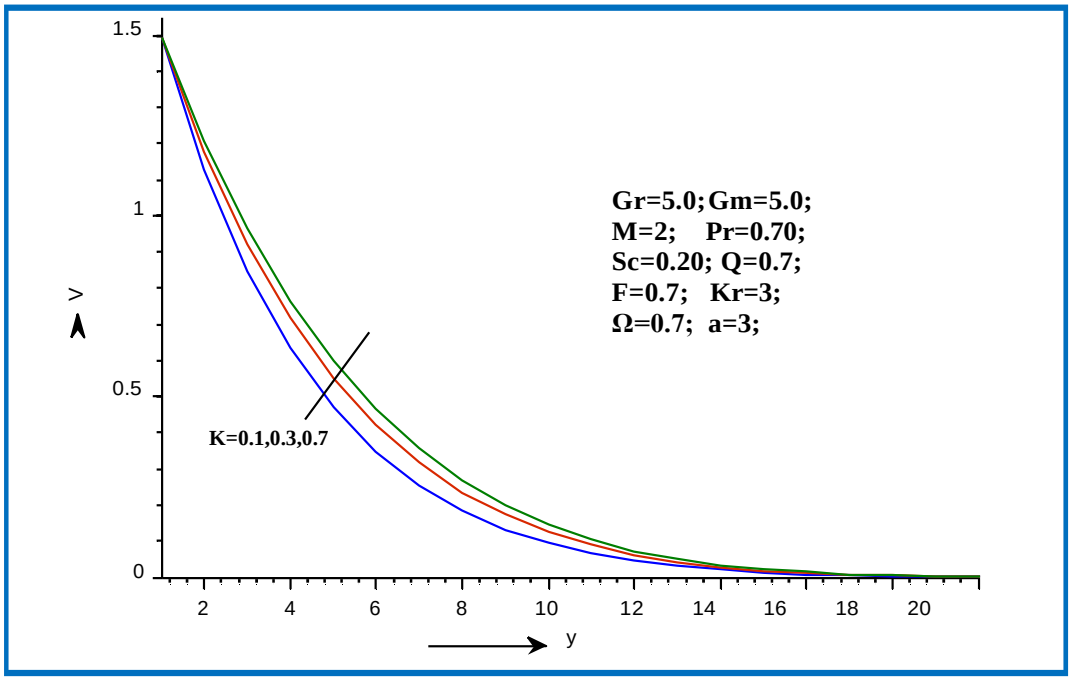

Figure 10: Illustration of the effect of the porosity parameter on the secondary velocity

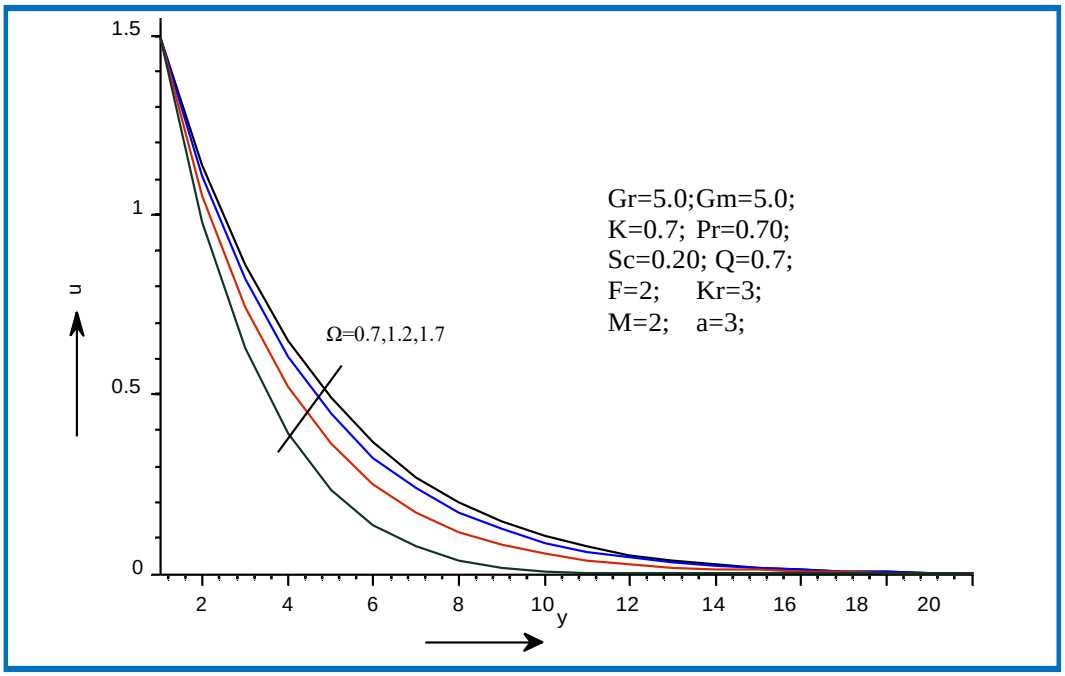

Figure 11: Illustration of the effect of the rotation parameter on the primary velocity

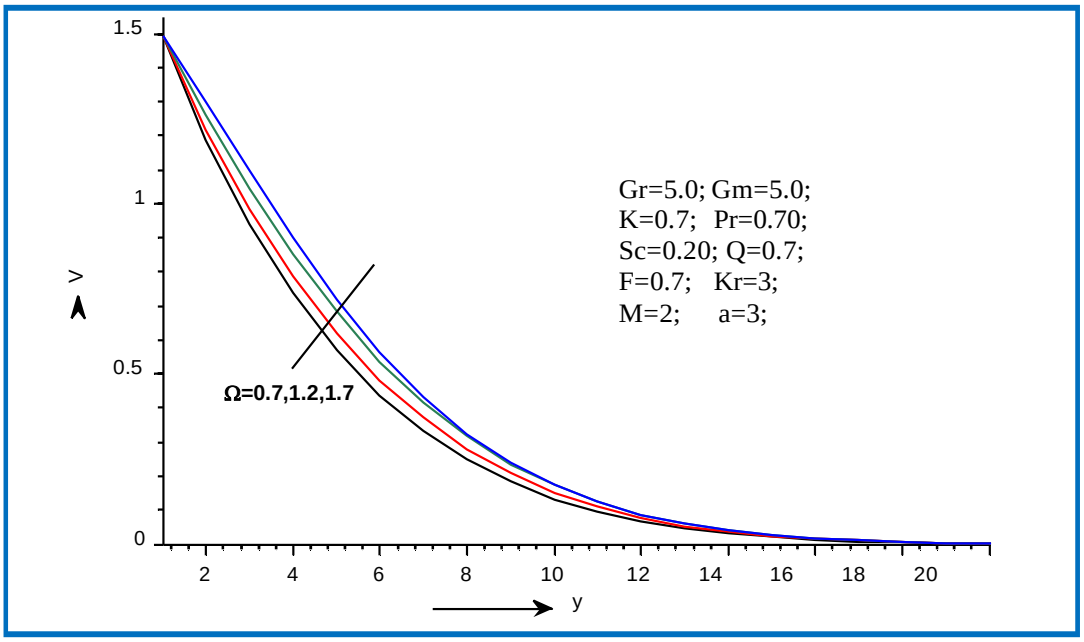

Figure 12: Illustration of the effect of the rotation parameter on the secondary velocity

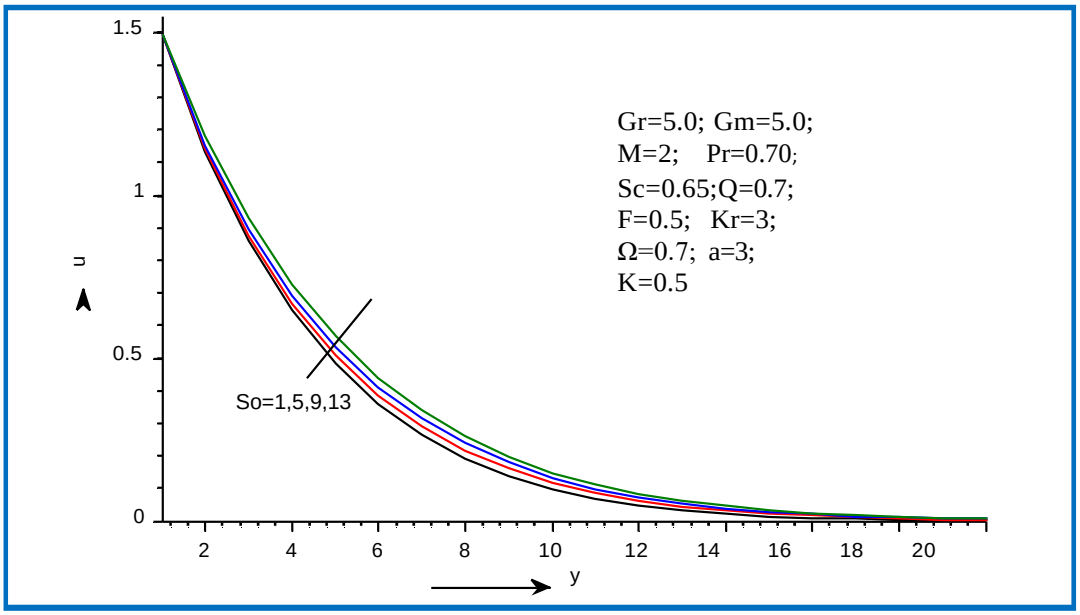

Figure 13: Illustration of the effect of the Soret number on the primary velocity

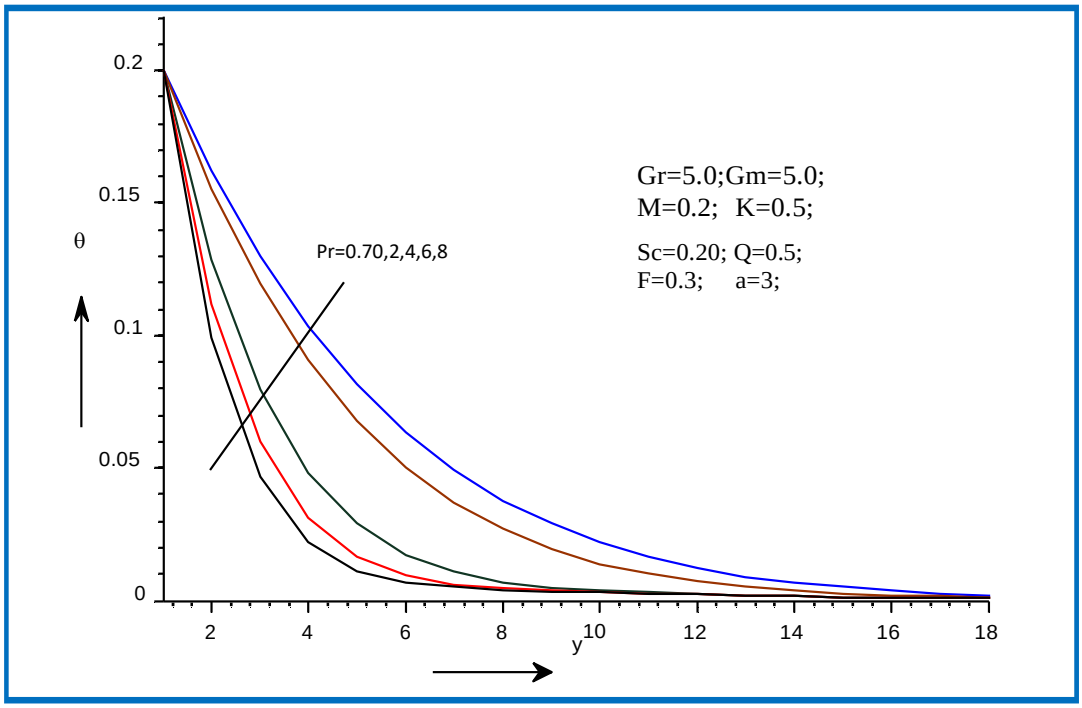

Figure 14: Illustration of the effect of the Prandtl number on the temperature

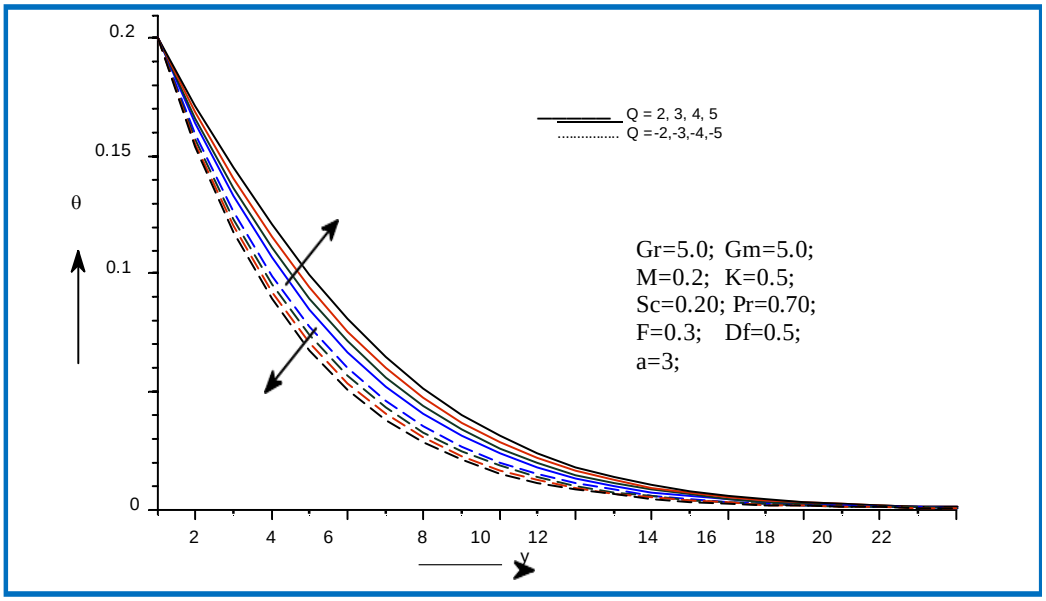

Figure 15: Illustration of the effect of the heat source and the sink parameters on the temperature

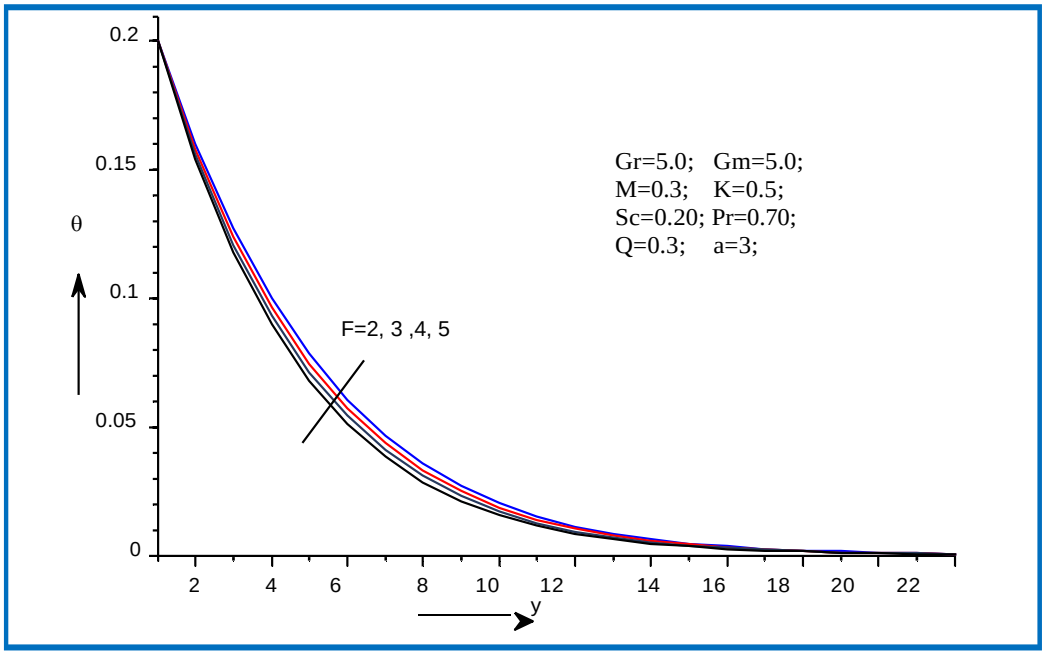

Figure 16: Illustration of the effect of the radiation parameter on the temperature

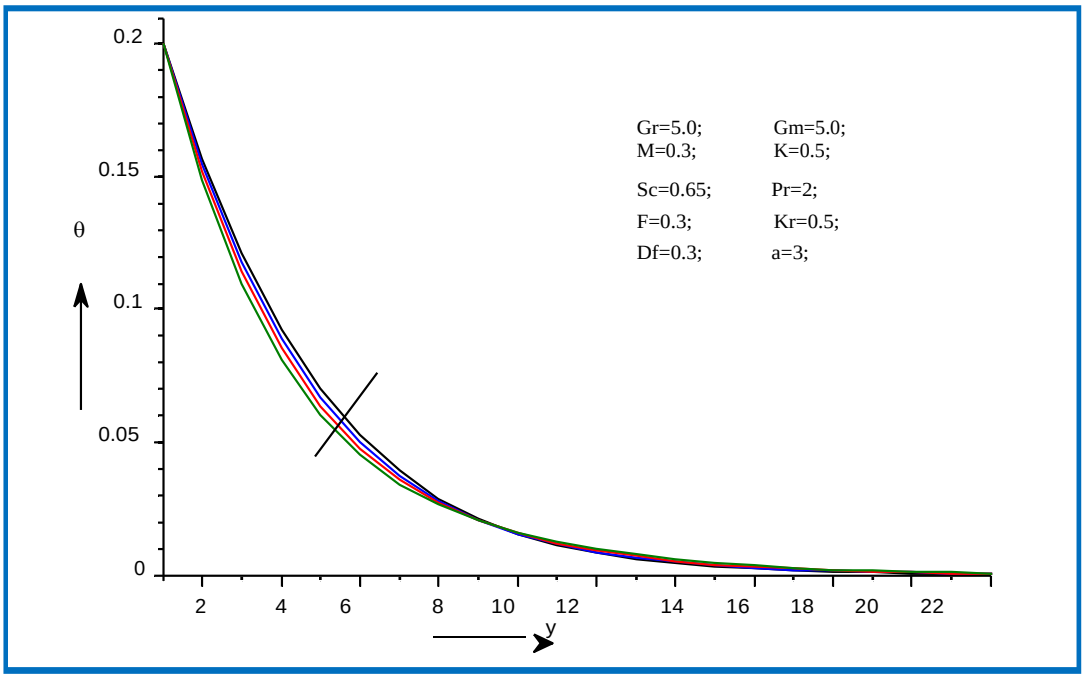

Figure 17: Illustration of the effect of the Soret number on the temperature

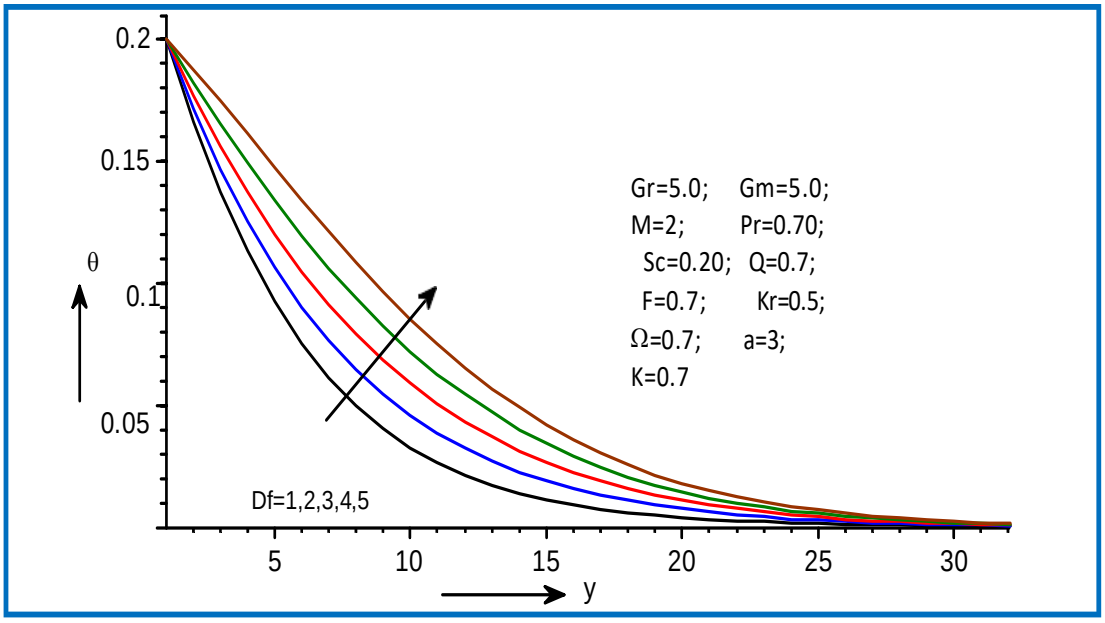

Figure 18 : Illustration of the effect of the Dufour number on the temperature

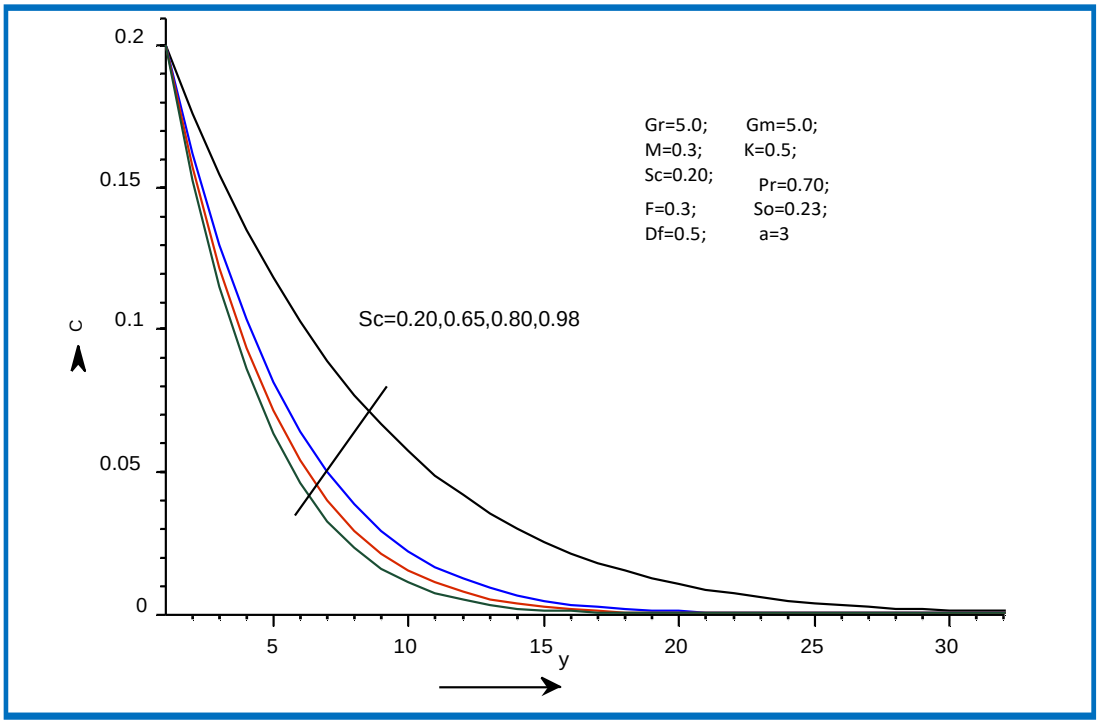

Figure 19: Illustration of the effect of the Schmidt number on the concentration

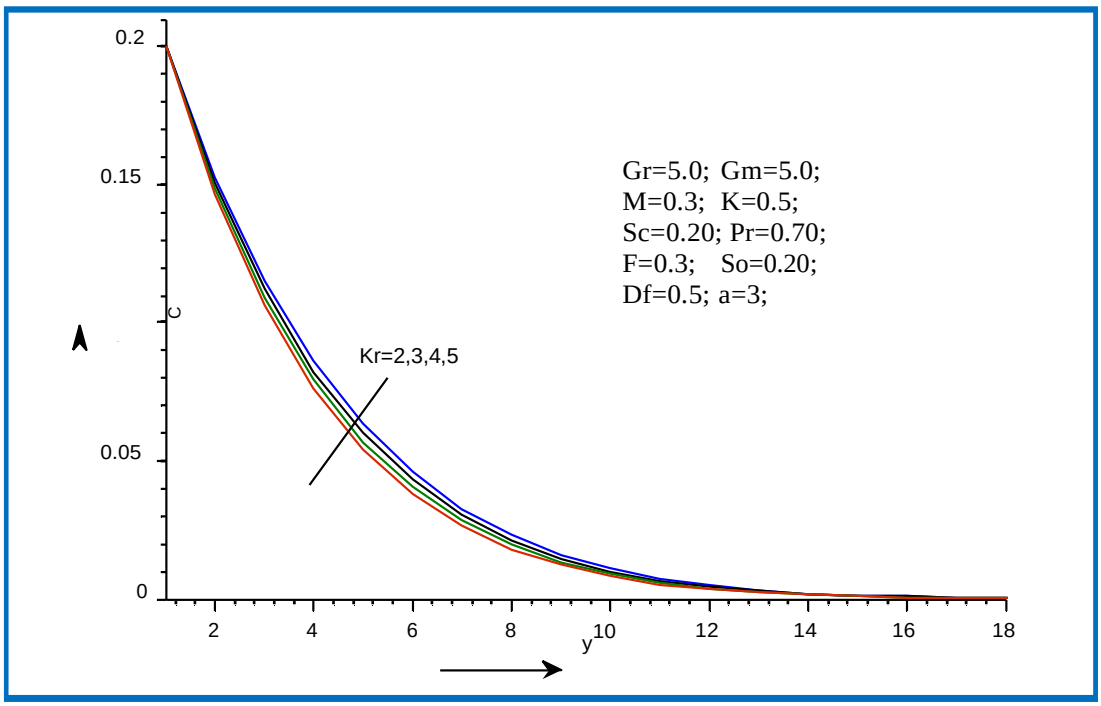

Figure 20 : Illustration of the effect of the chemical reaction parameter on the concentration

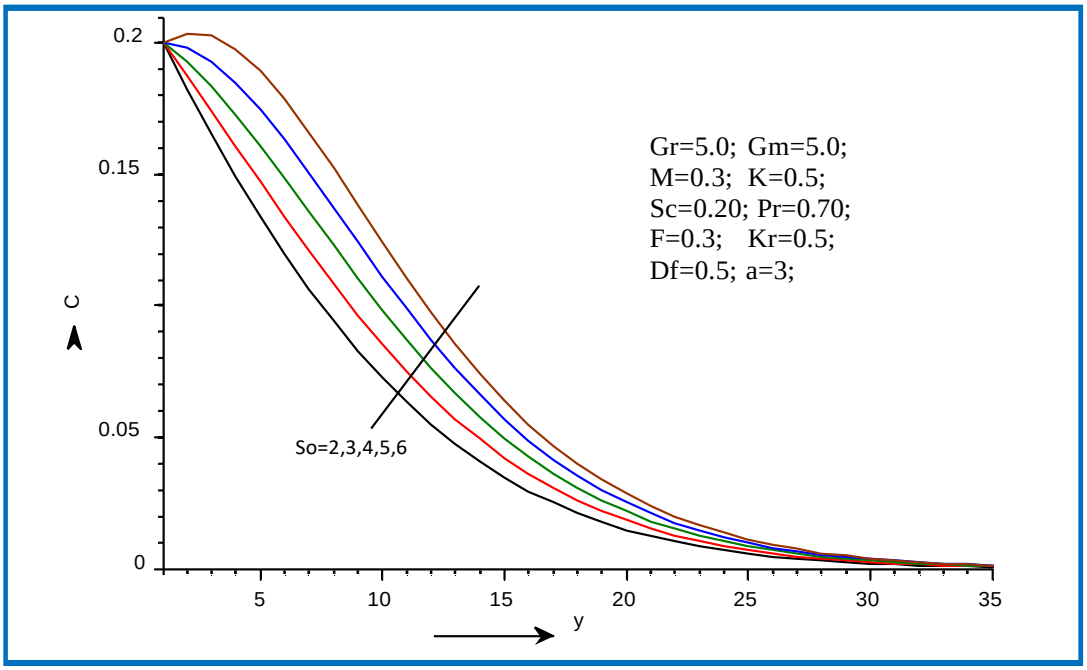

Figure 21: Illustration of the effect of the Soret number on the concentration

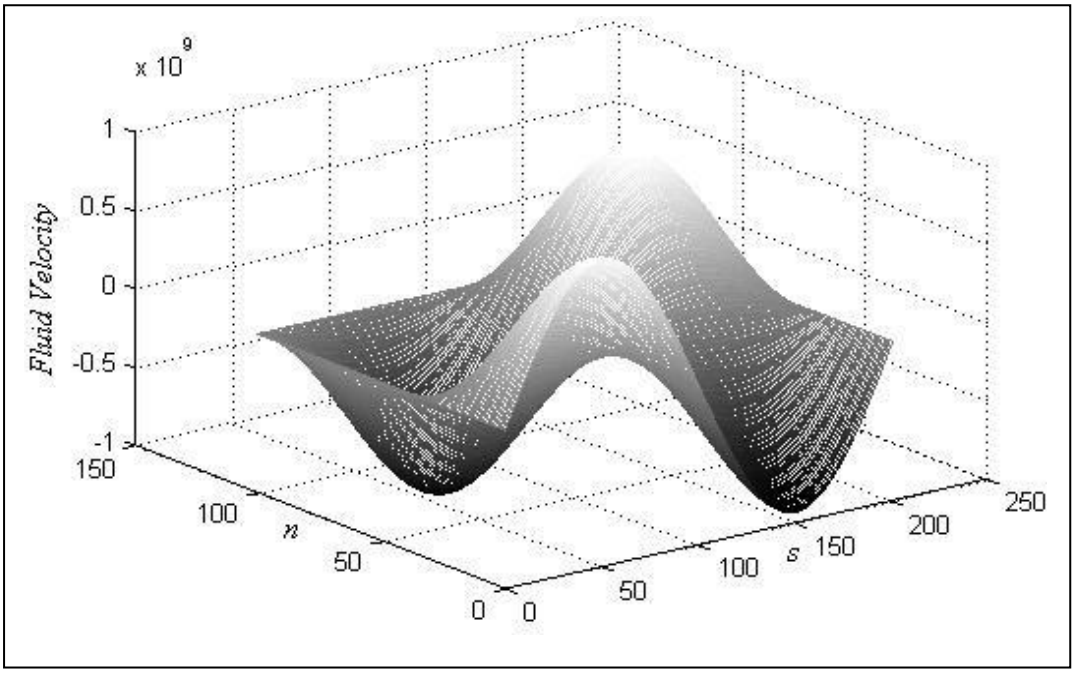

Figure 22: Illustration of the Variation of the fluid velocity with *s* and *n* for *Re* = 1.5 in case of impulsive motion

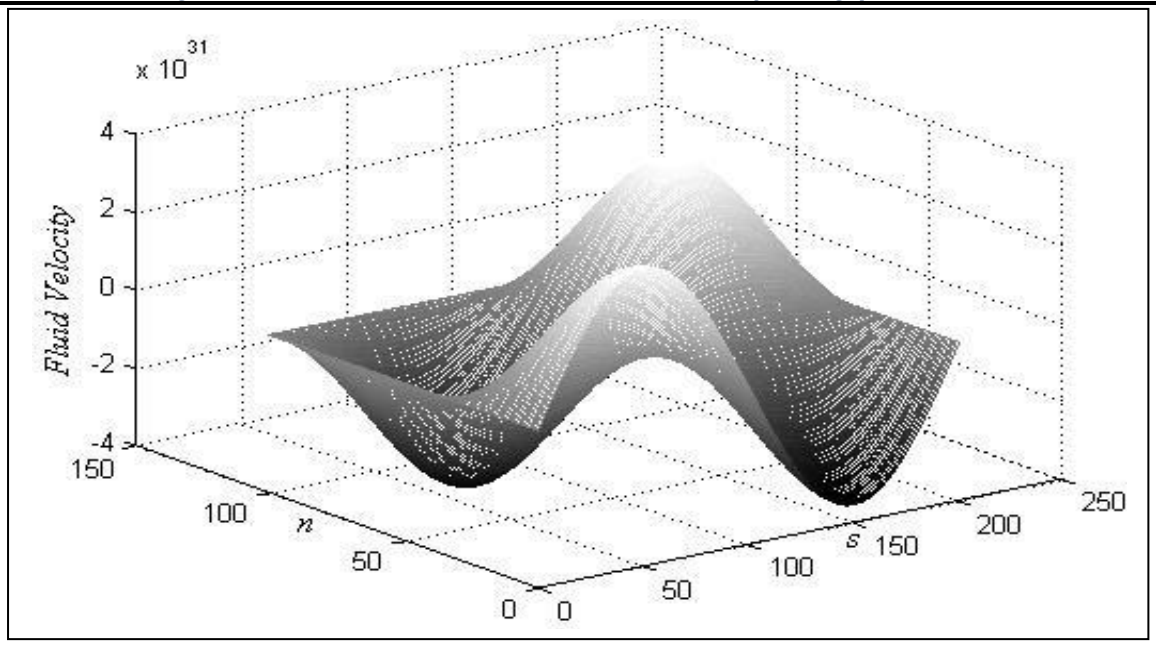

Figure 23: Illustration of the Variation of the fluid velocity with *s* and *n* for *Re* = 0.7 in case of impulsive motion

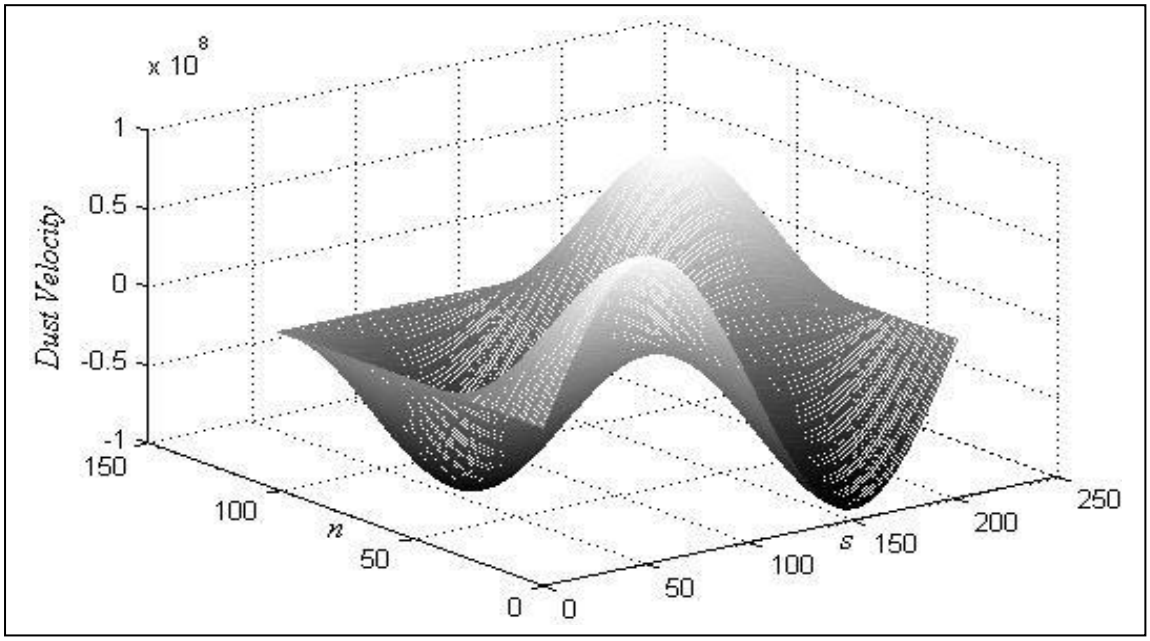

Figure 24: Illustration of the Variation of the dust phase velocity with *s* and *n* for *Re* = 1.5 in case of impulsive motion

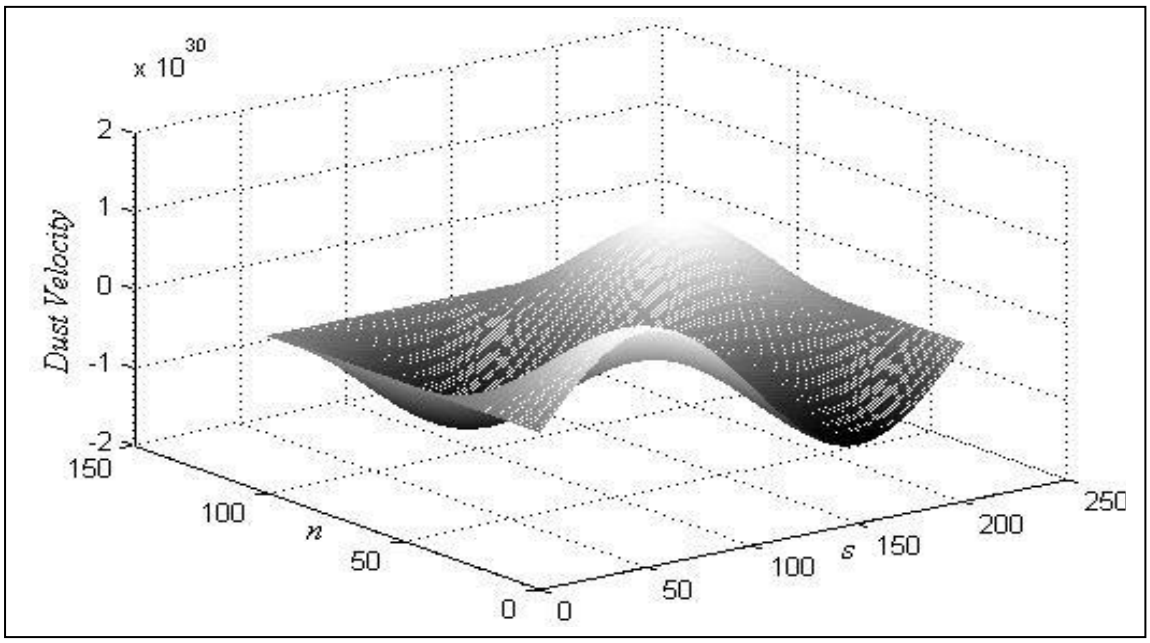

Figure 25: Illustration of the Variation of the dust phase velocity with *s* and *n* for *Re* = 0.7 in case of impulsive motion

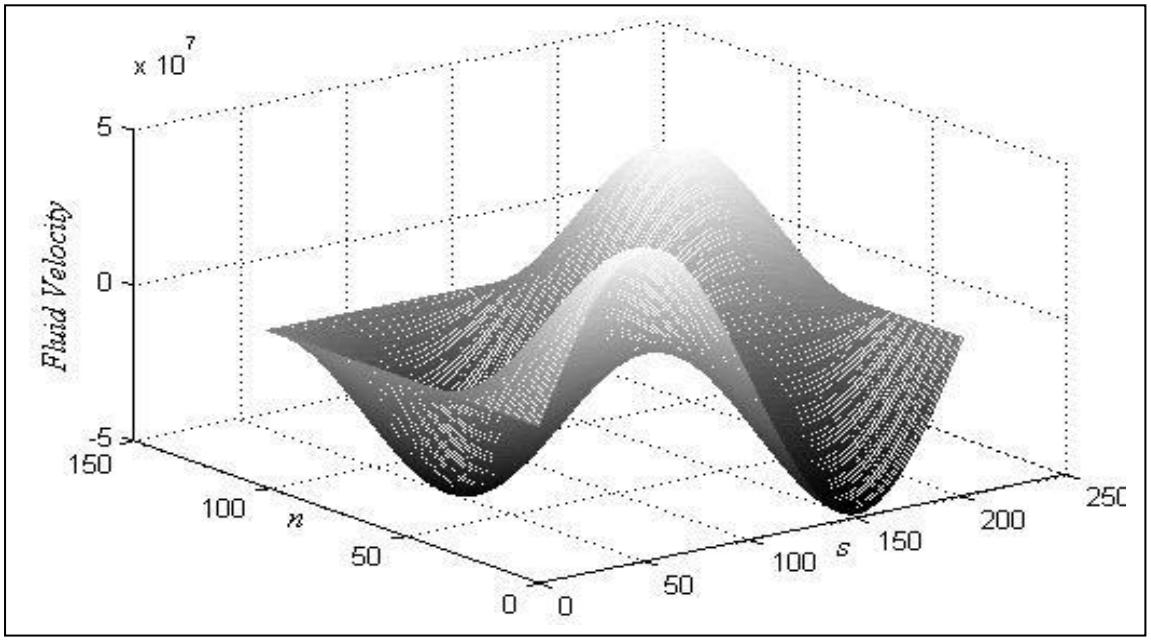

Figure 26: Illustration of the Variation of the fluid velocity with *s* and *n* for *Re* = 1.5 in case of transition motion

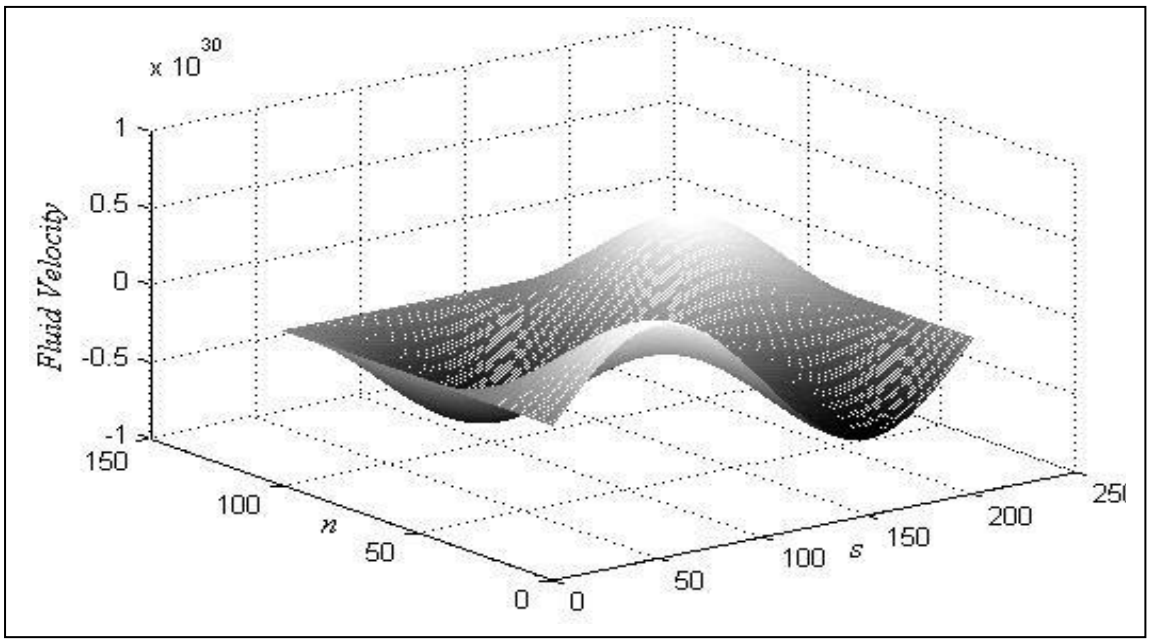

Figure 27: Illustration of the Variation of the fluid velocity with *s* and *n* for *Re* = 0.7 in case of transition motion

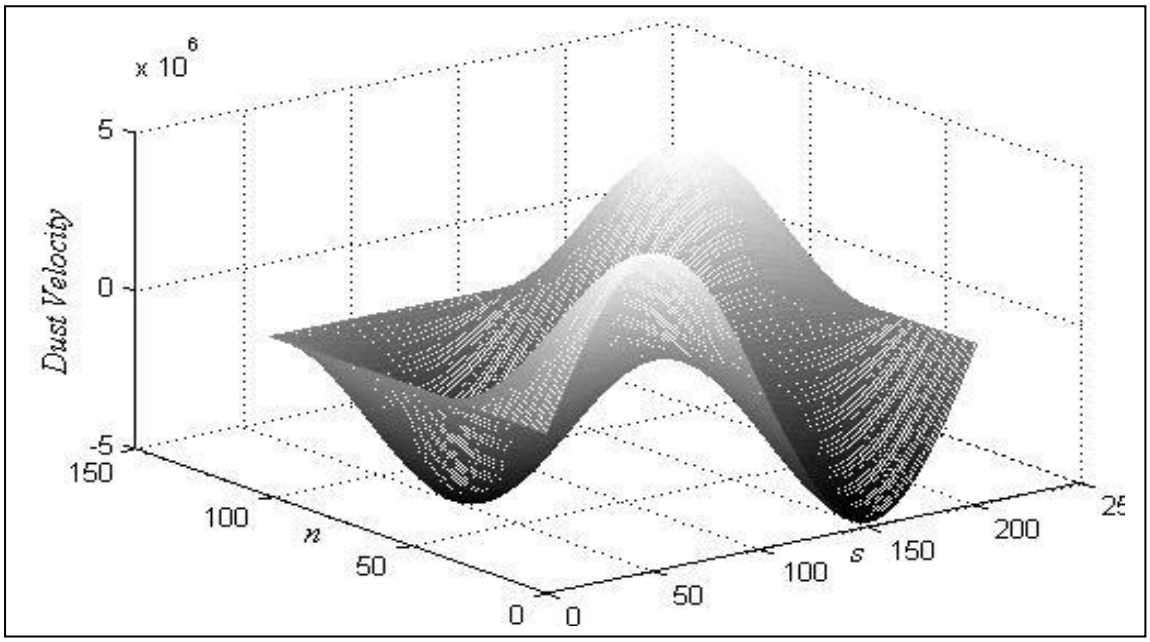

Figure 28: Illustration of the Variation of the dust phase velocity with *s* and *n* for *Re* = 1.5 in case of transition motion

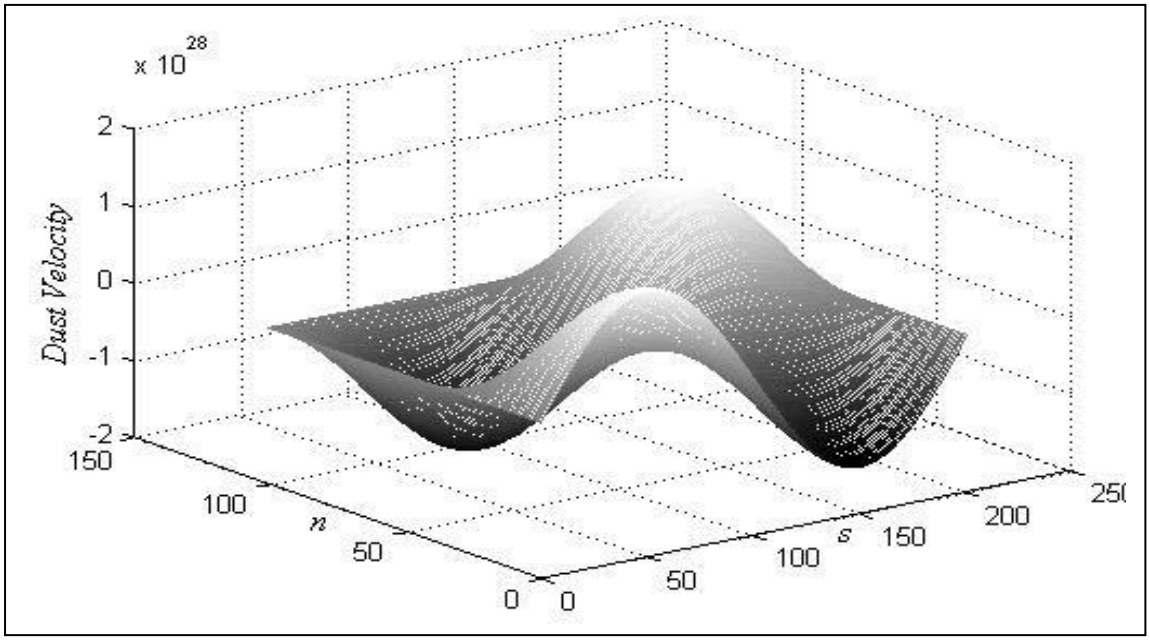

Figure 29: Illustration of the Variation of the dust phase velocity with *s* and *n* for *Re* = 0.7 in case of transition motion

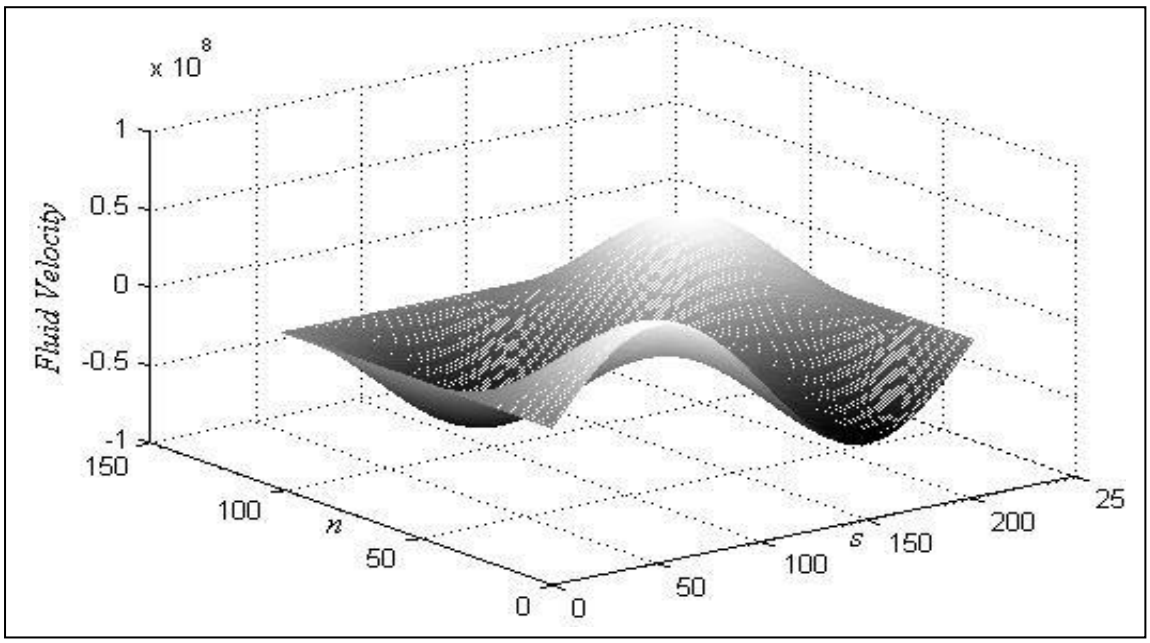

Figure 30: Illustration of the Variation of the fluid velocity with *s* and *n* for *Re* = 1.5 in case of motion for a finite time

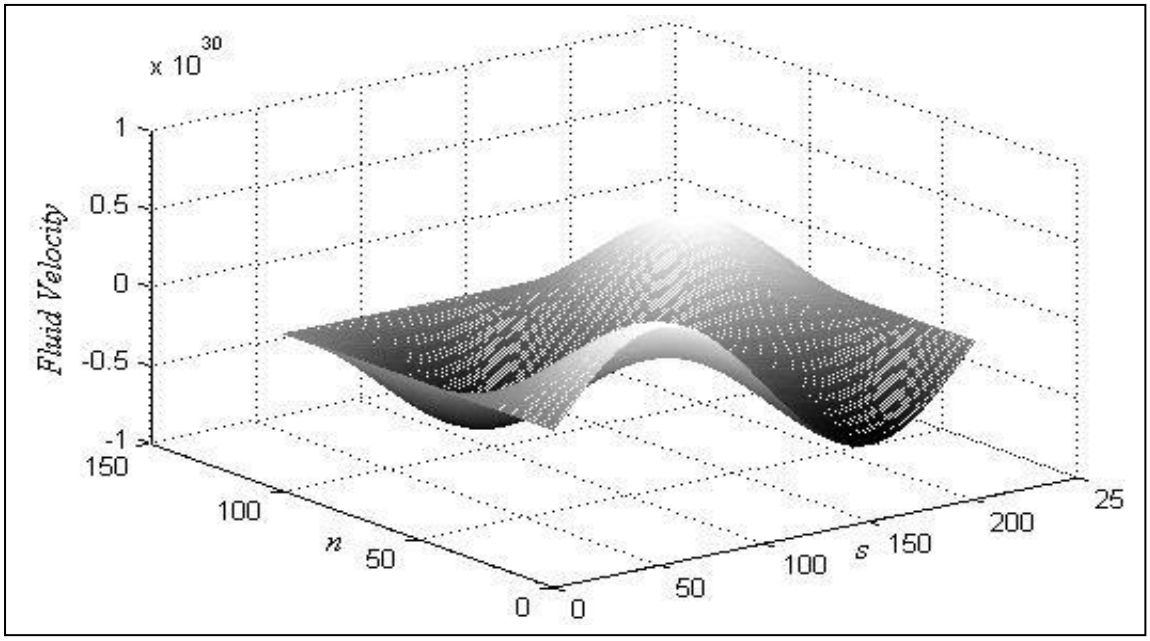

Figure 31: Illustration of the Variation of the fluid velocity with *s* and *n* for *Re* = 0.7 in case of motion for a finite time

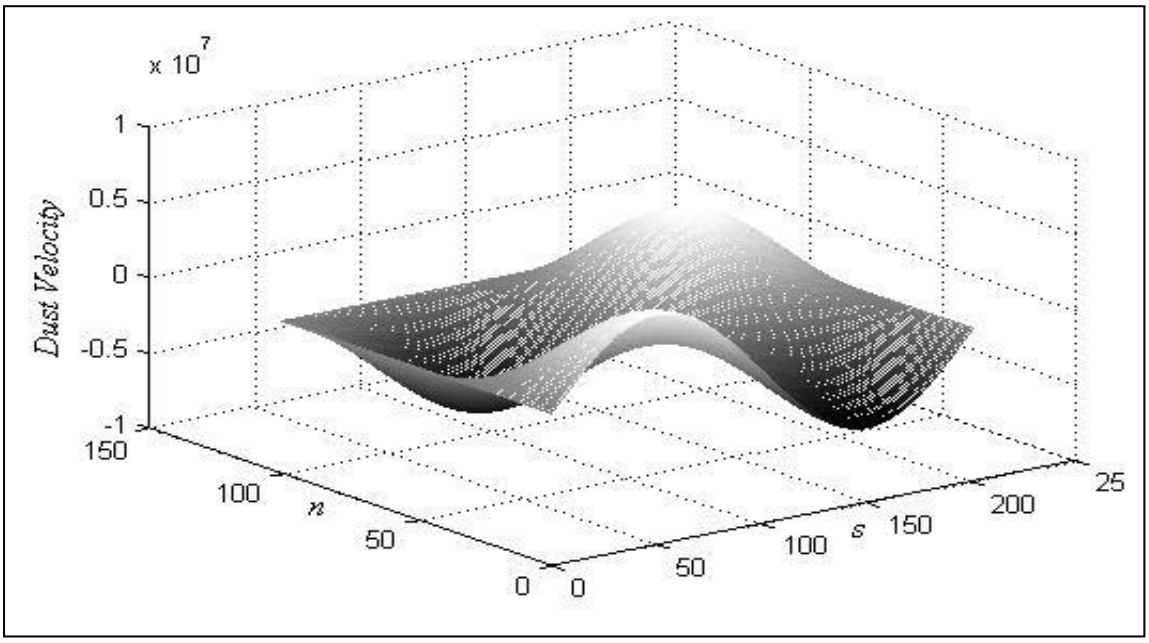

Figure 32: Illustration of the Variation of the dust phase velocity with *s* and *n* for *Re* = 1.5 in case of motion for a finite time

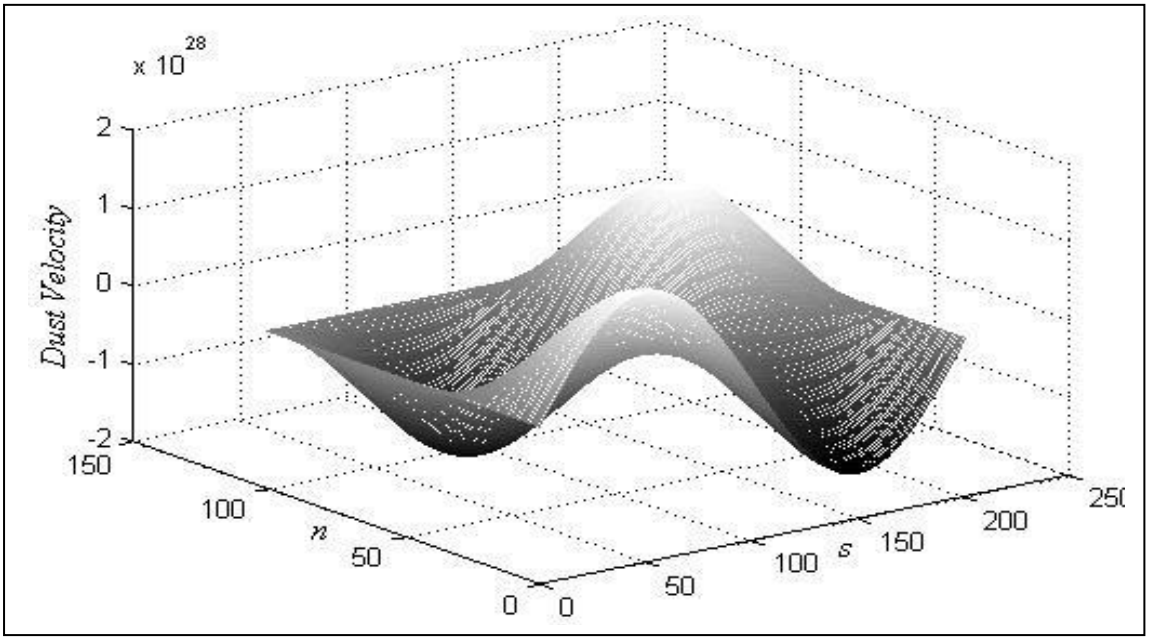

Figure 33: Illustration of the Variation of the dust phase velocity with *s* and *n* for *Re* = 0.7 in case of motion for a finite time

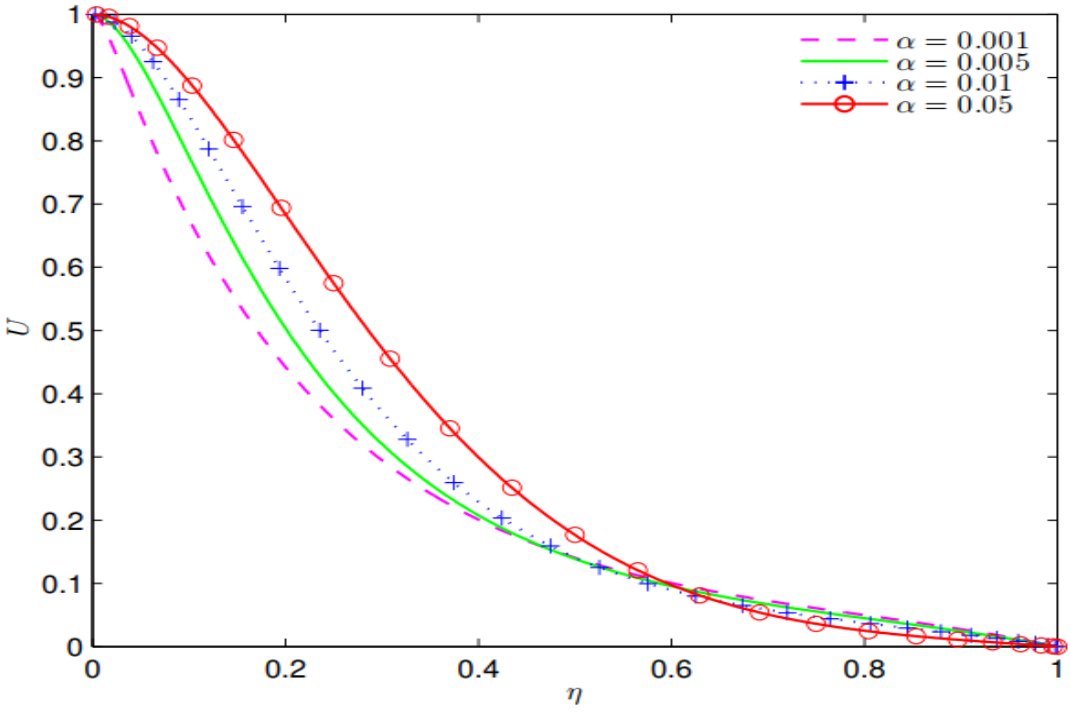

Figure 34: Illustration of the Axial velocity distribution *U* for different values of α

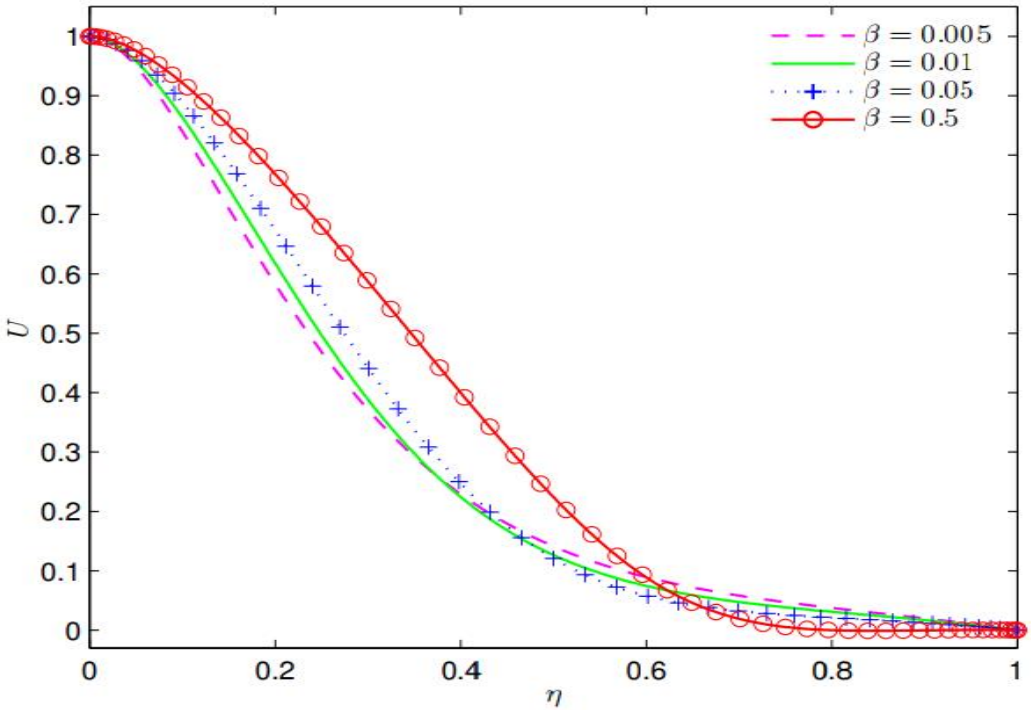

Figure 35: Illustration of the Axial velocity distribution *U* for different values of β

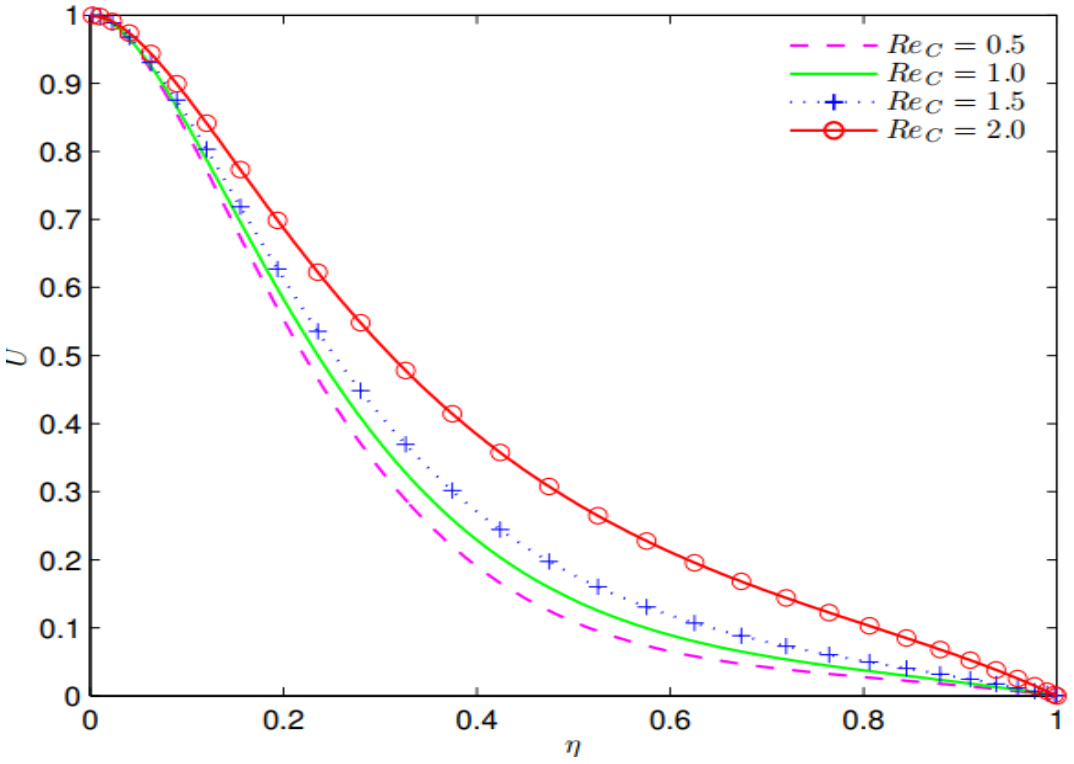

Figure 36: Illustration of the Axial velocity distribution *U* for different values of Rec

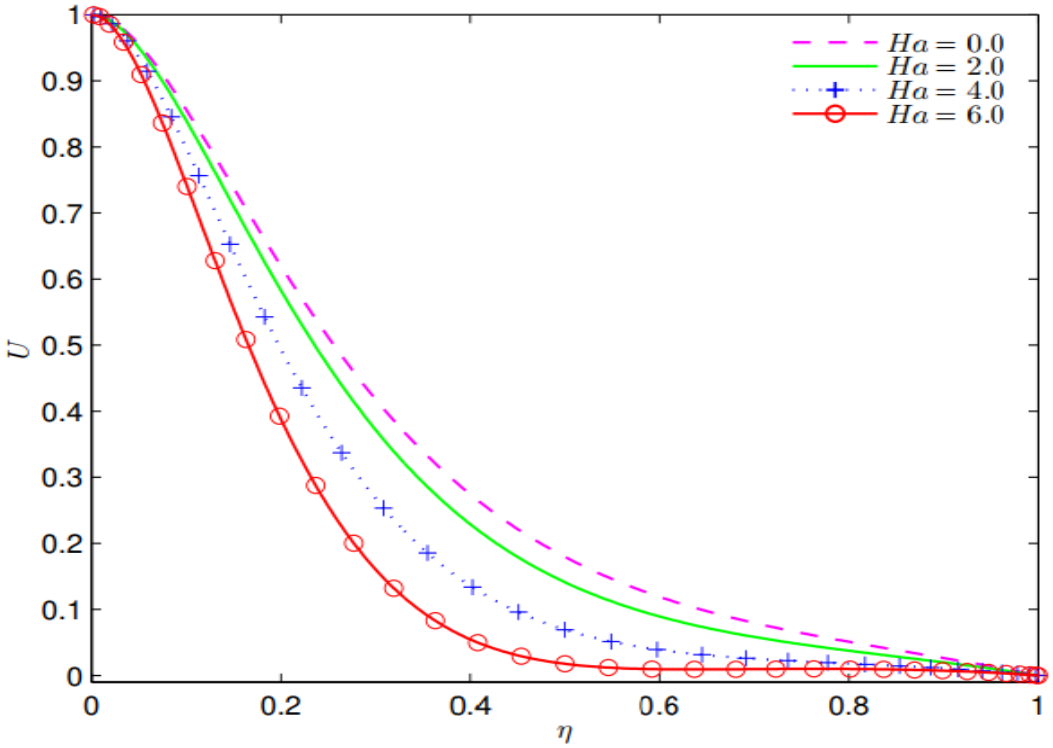

Figure 37: Illustration of the Axial velocity distribution *U* for different values of Ha

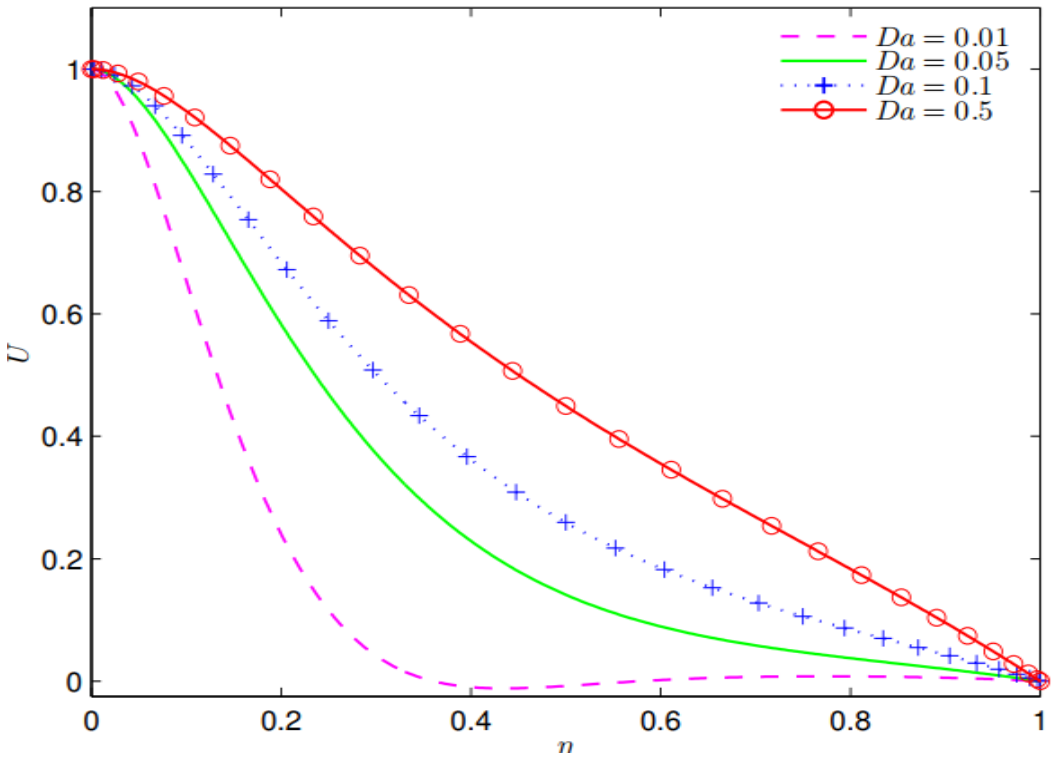

Figure 38: Illustration of the Axial velocity distribution *U* for different values of Da

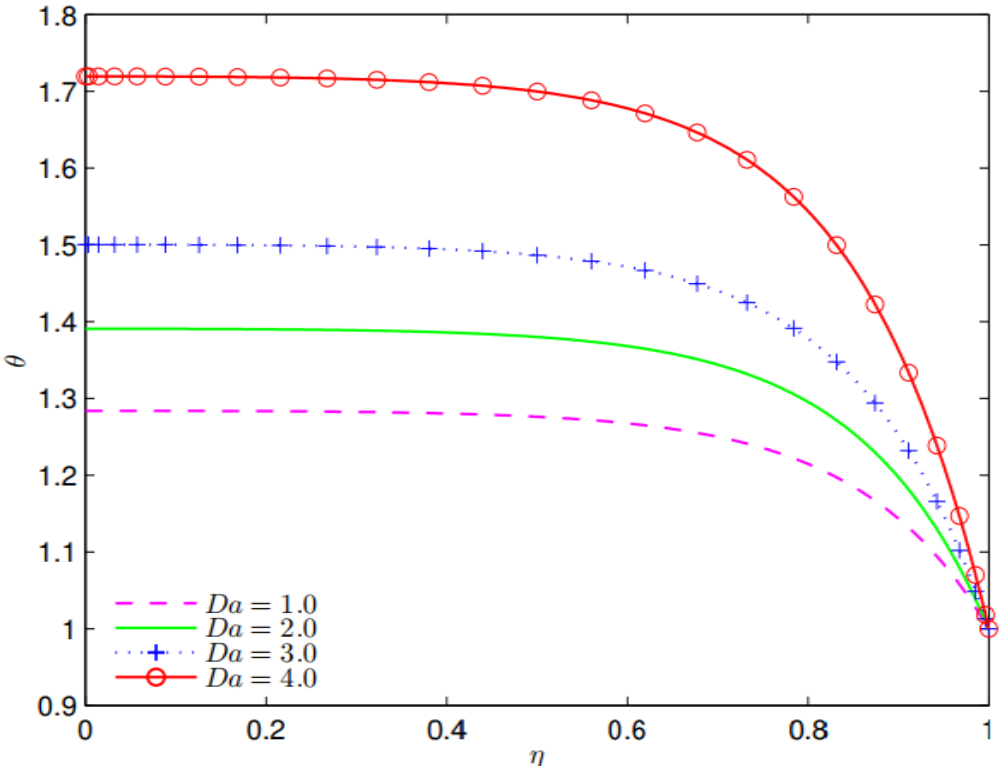

Figure 39: Illustration of the Temperature distribution θ for different values of *Da*

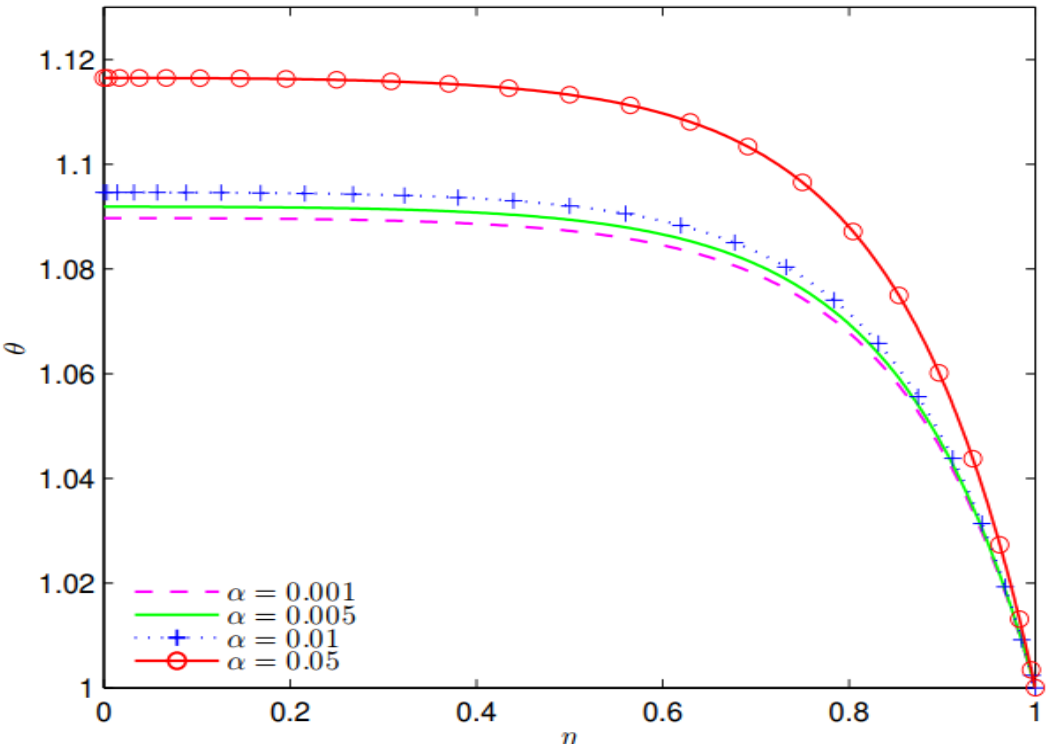

Figure 40: Illustration of the Temperature distribution θ for different values of α

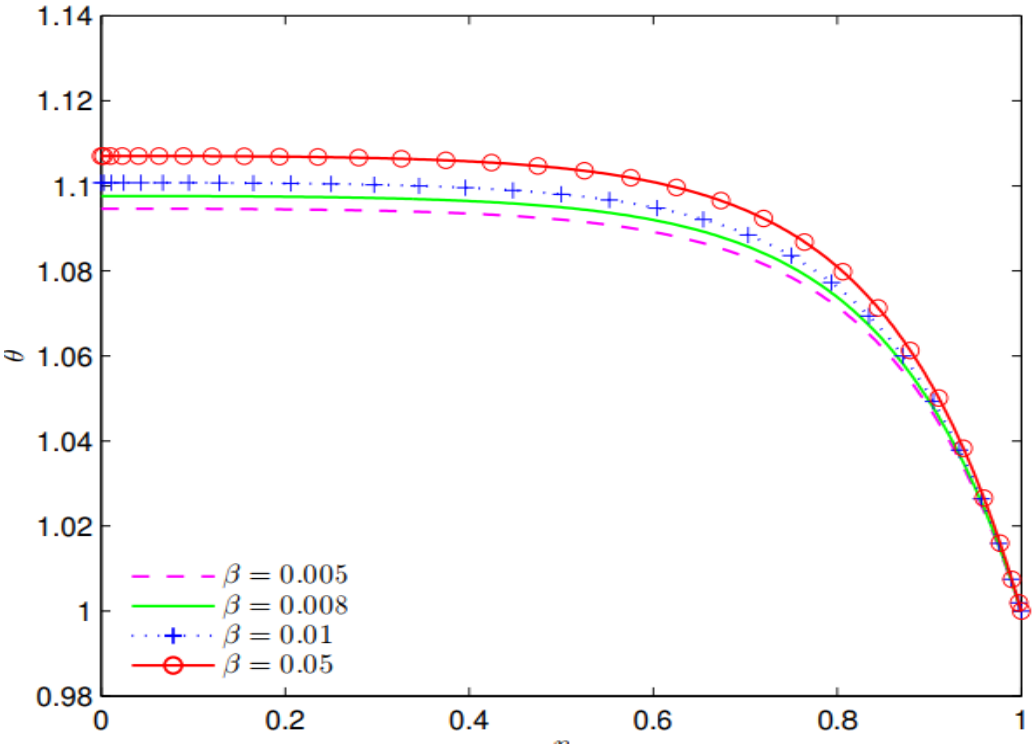

Figure 41: Illustration of the Temperature distribution θ for different values of β

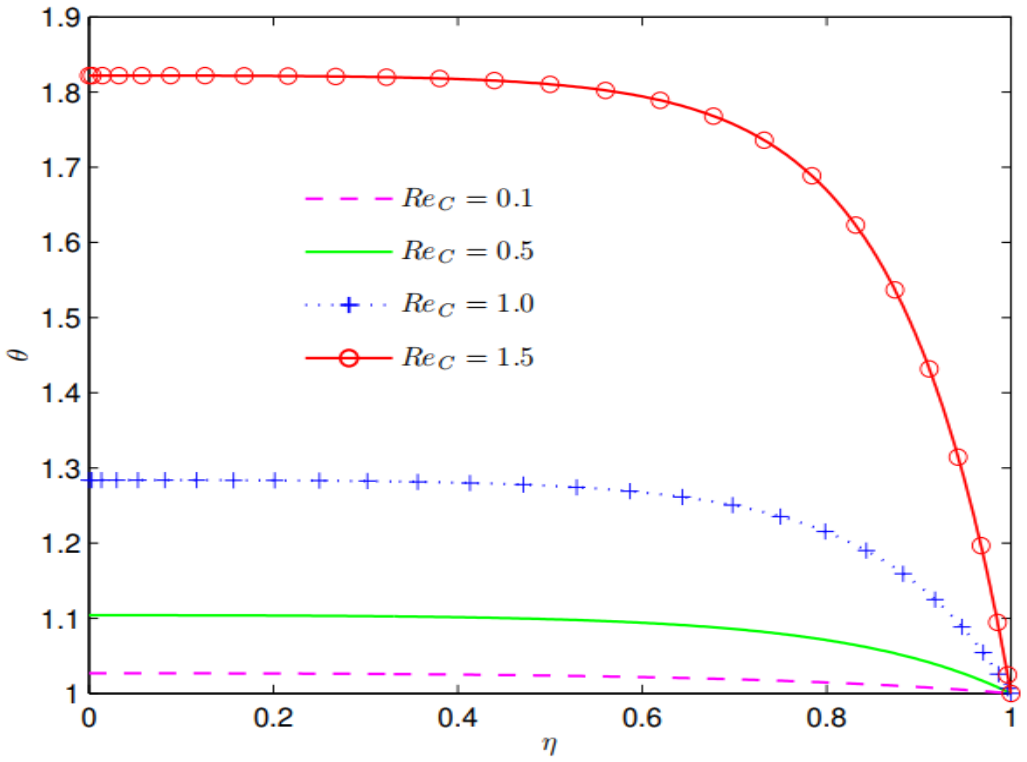

Figure 42: Illustration of the Temperature distribution θ for different values of Rec

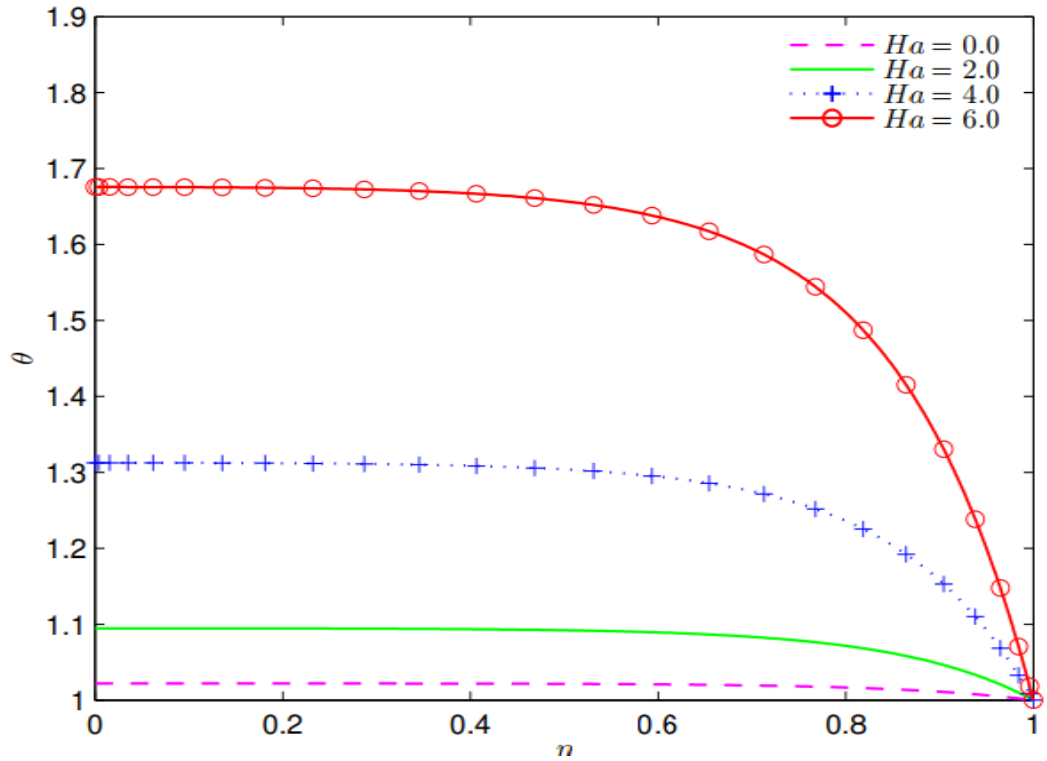

Figure 43: Illustration of the Temperature distribution θ for different values of Ha

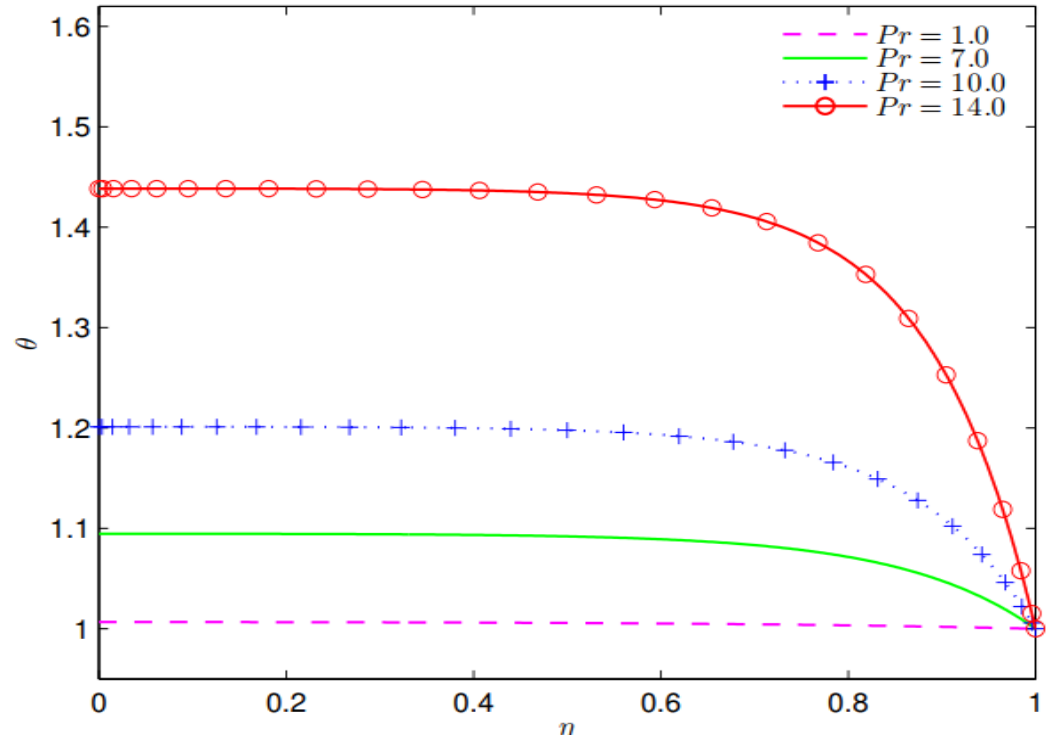

Figure 44: Illustration of the Temperature distribution θ for different values of Pr

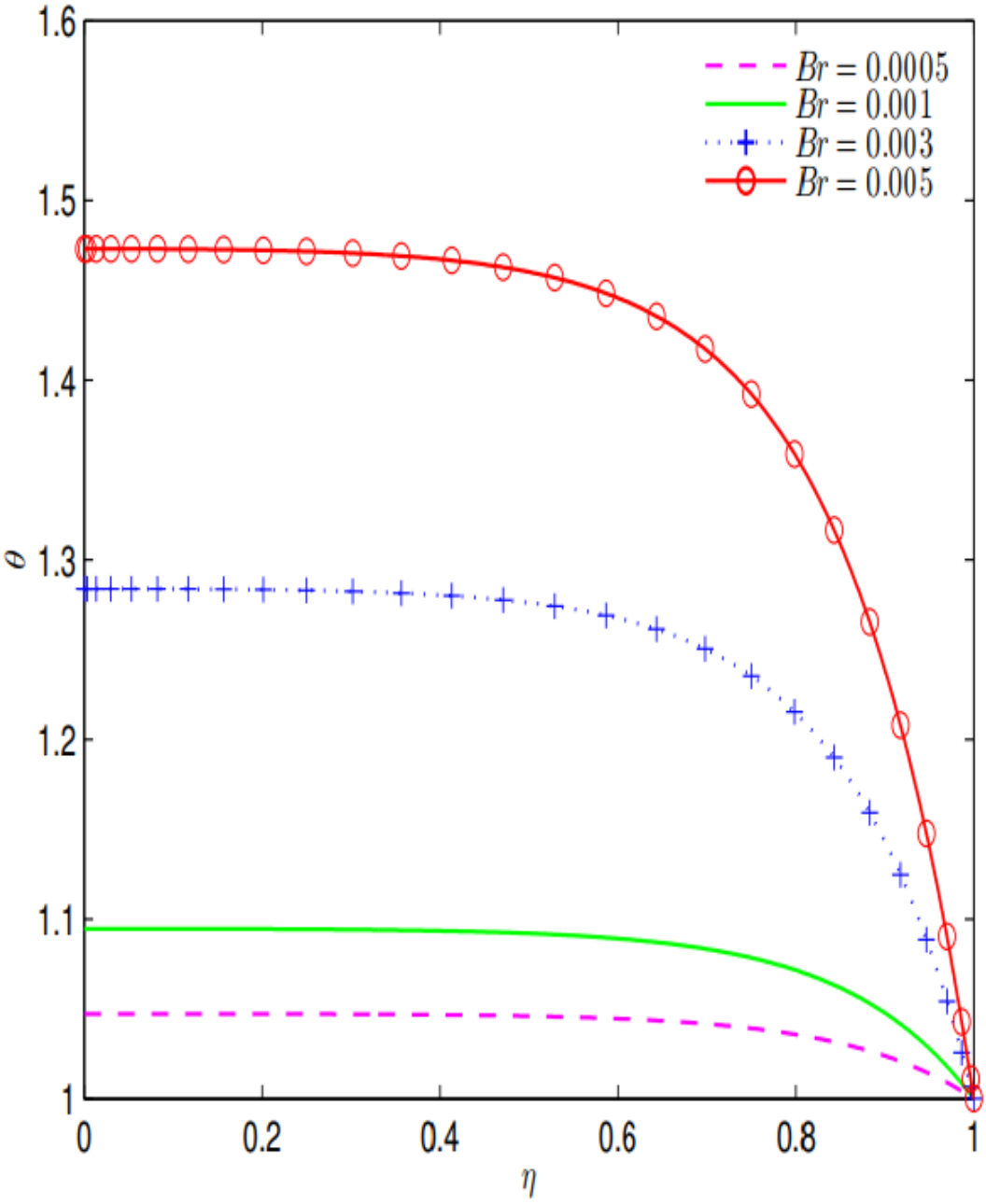

Figure 45: Illustration of the Temperature distribution θ for different values of Br

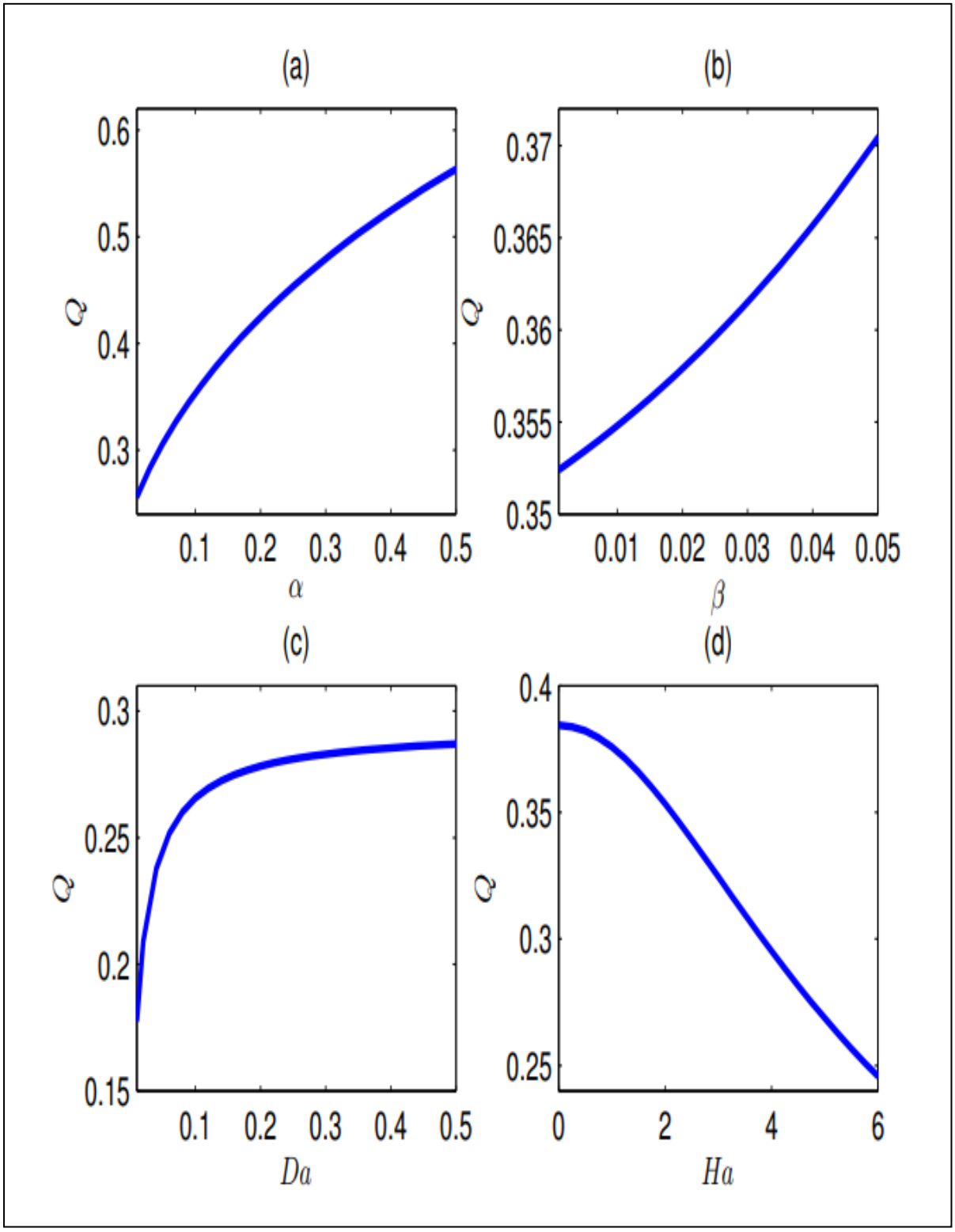

Figure 46[(a), (b), (c), (d)]: Illustration of the Volume rate of flow for the flow Parameters for α, β, Da and Ha respectively.

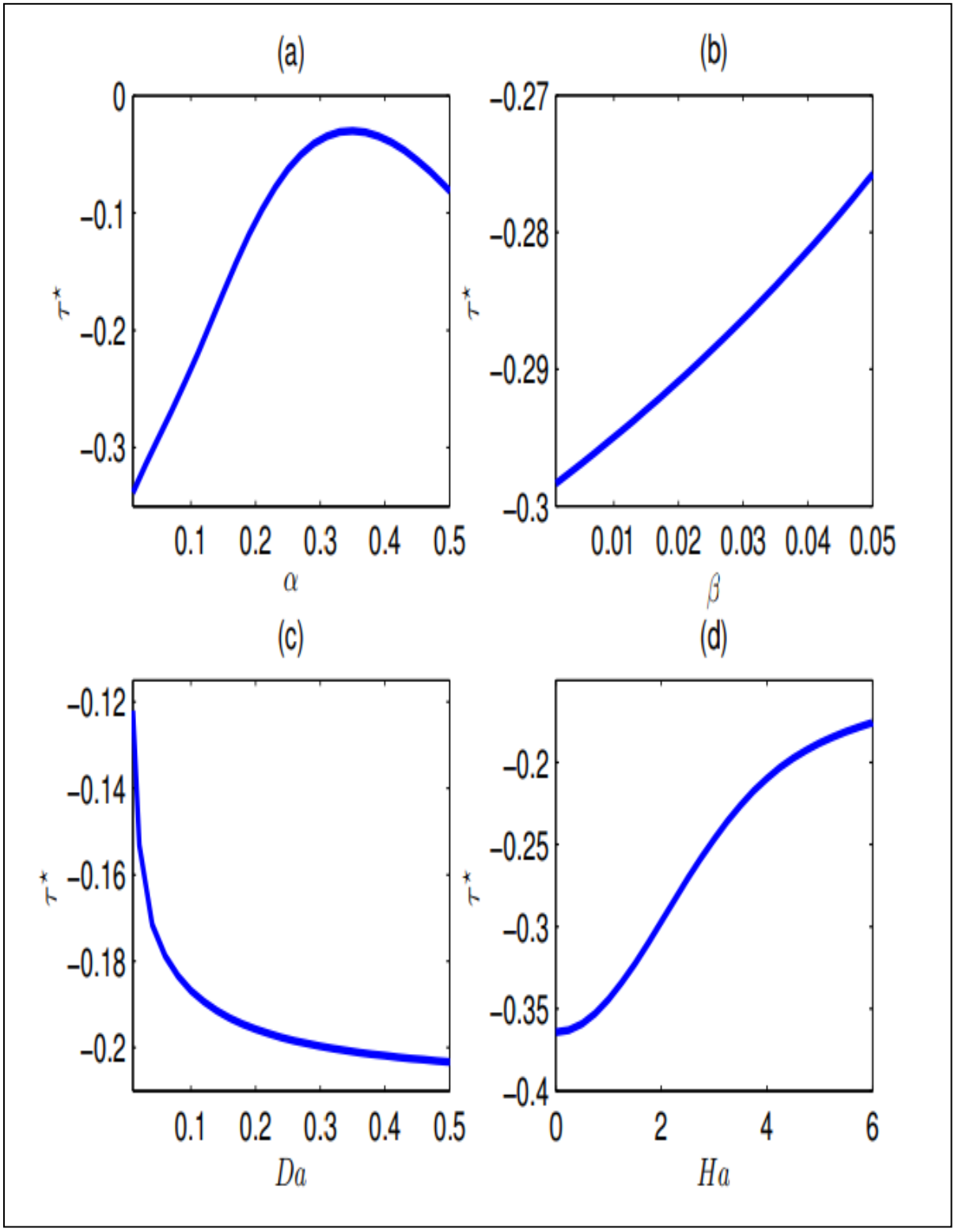

Figure 47[(a), (b), (c), (d)]: Illustration of the Wall shear stress for different flow parameters for α, β, Da and Ha respectively.

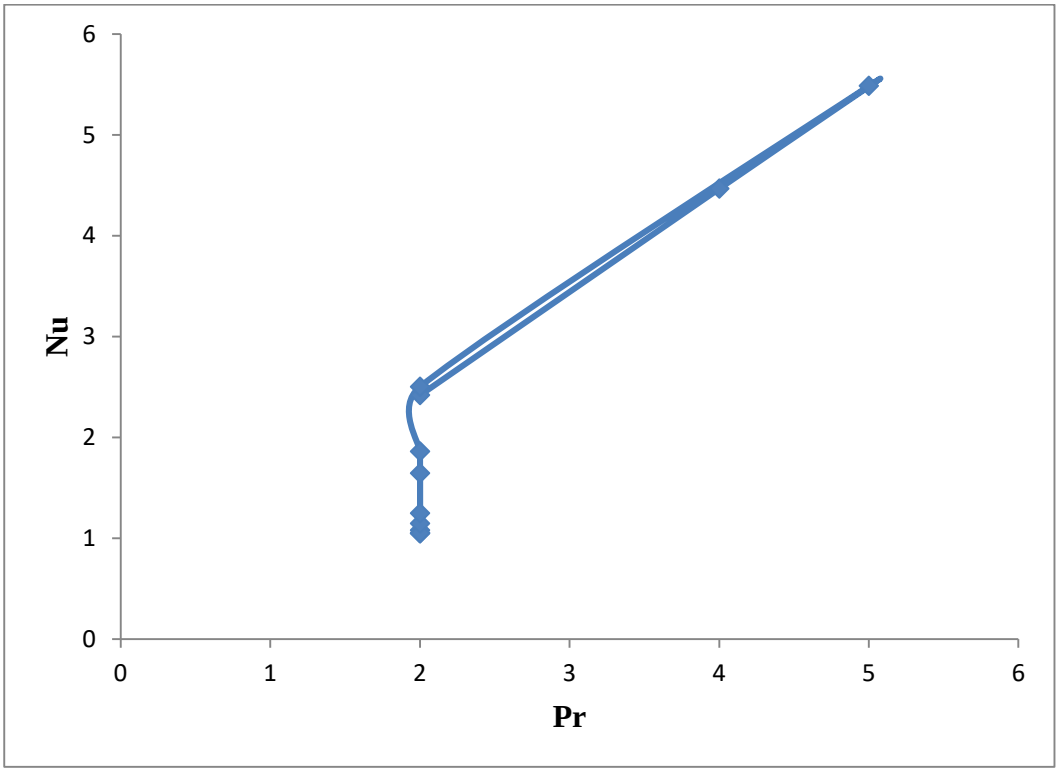

Figure 48: Illustration of the variation of Nu with Pr

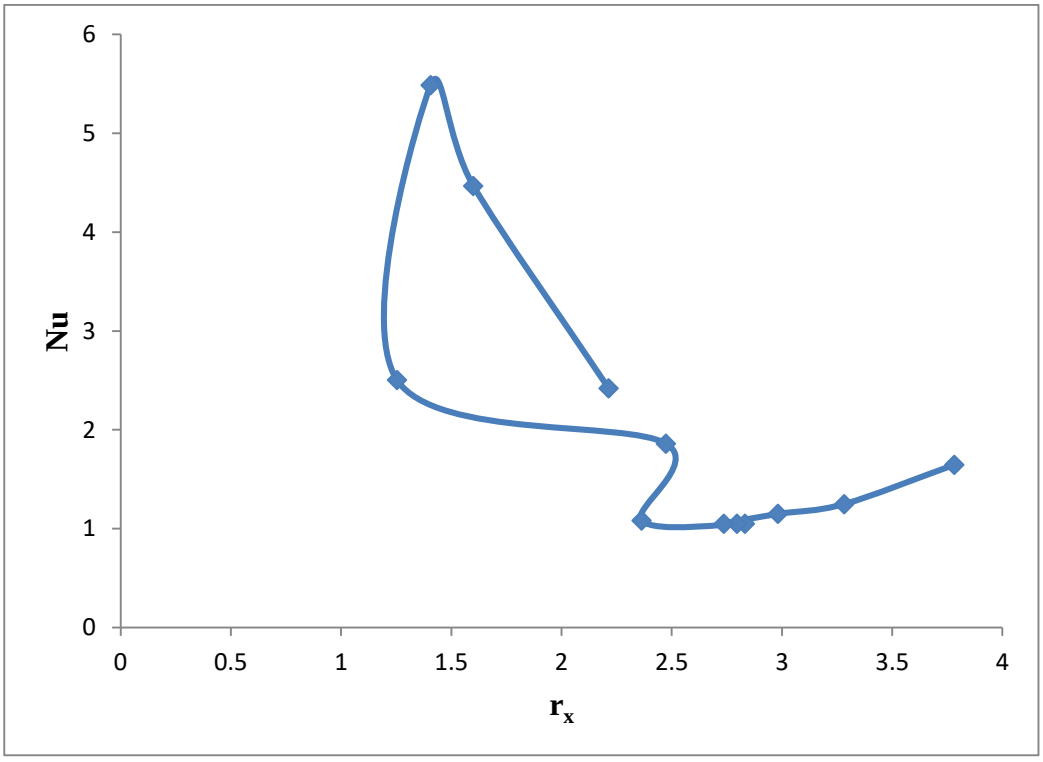

Figure 49: Illustration of the variation of Nu with T_x

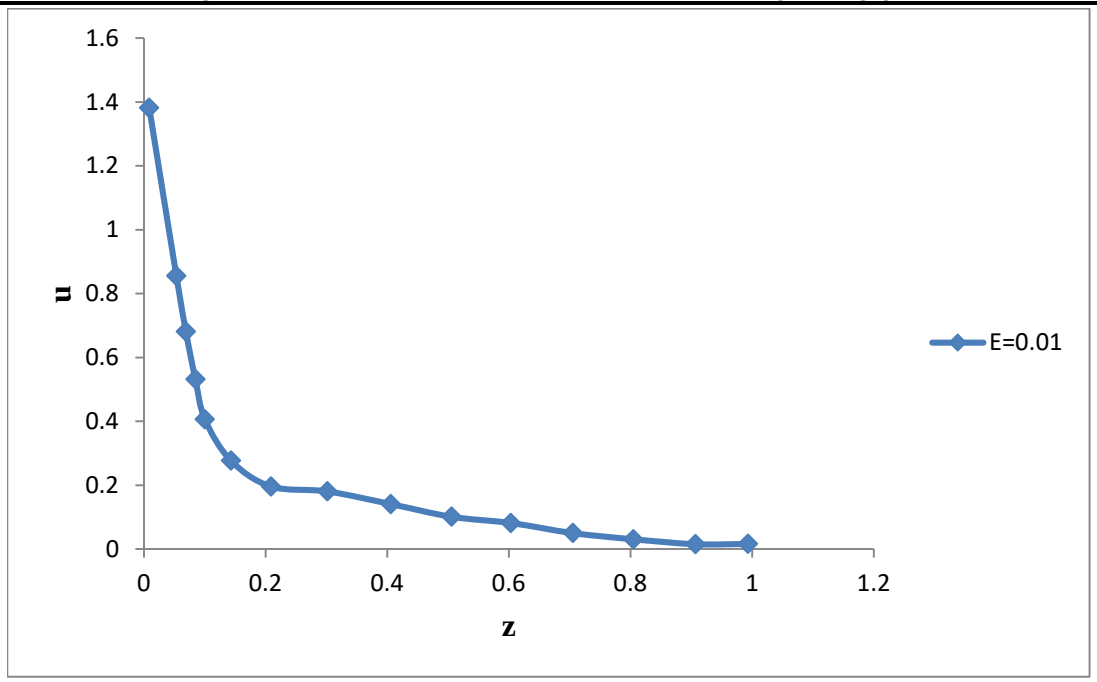

Figure 50 : Illustration of the Velocity profile of u with E=0.01, when β_1=2, D^{-1}=3000 and M=1

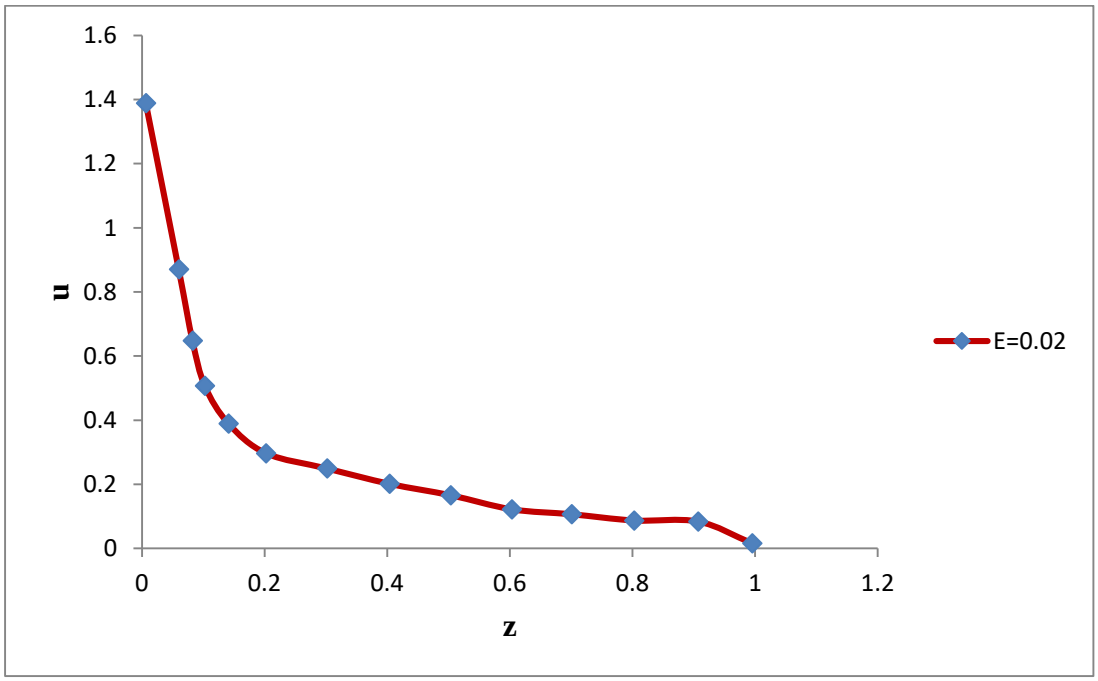

Figure 51 : Illustration of the Velocity profile of u with E=0.02, when β_1=2, D^{-1}=3000 and M=1

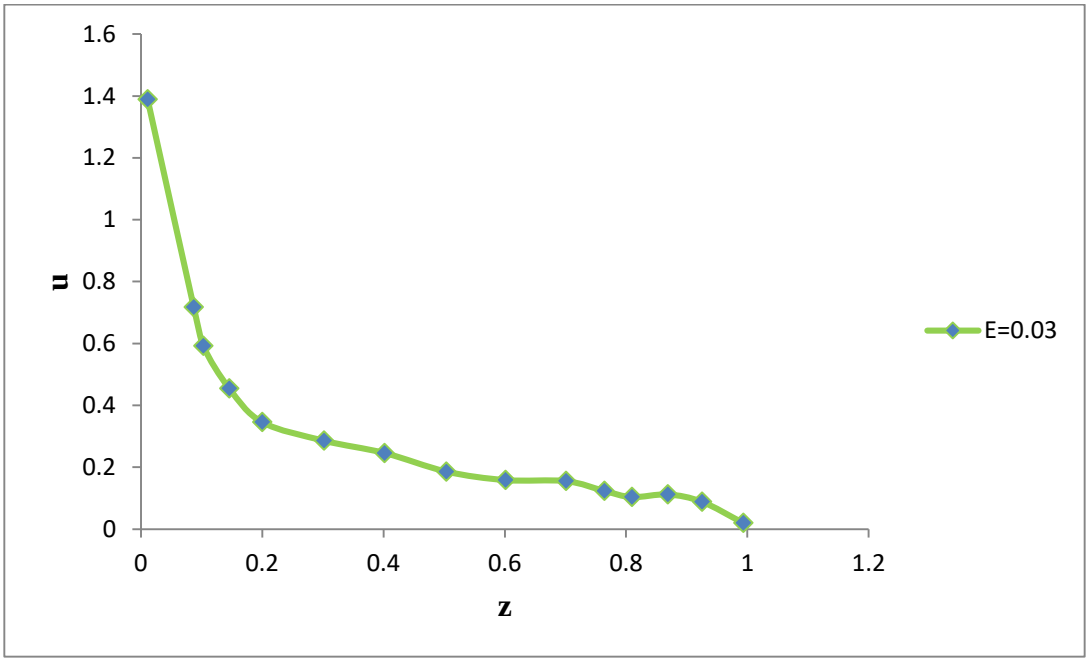

Figure 52 : Illustration of the Velocity profile of u with E=0.03, when β_1=2, D^{-1}=3000 and M=1

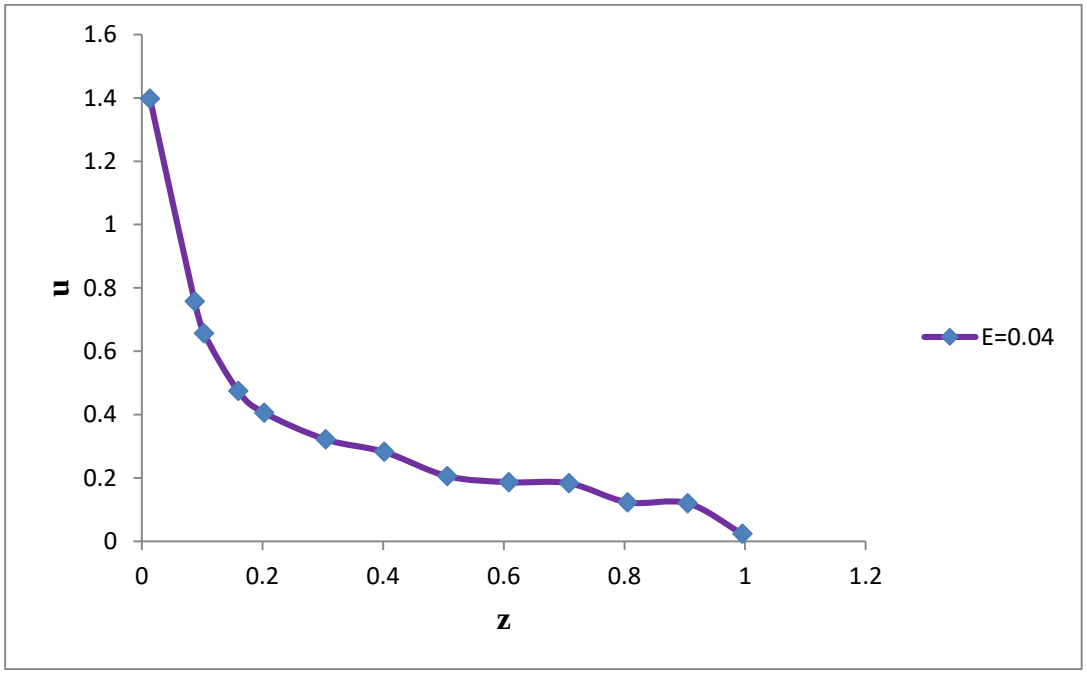

Figure 53 : Illustration of the Velocity profile of u with E=0.04, when β_1=2, D^{-1}=3000 and M=1

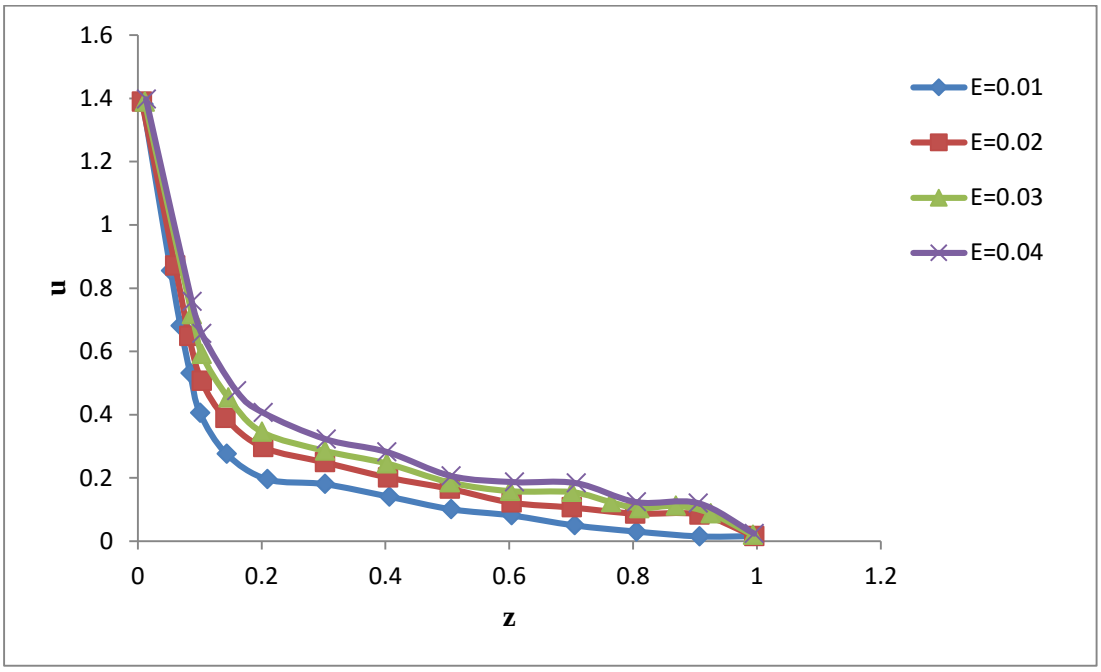

Figure 54 : Illustration of the Velocity profile of u with different values of E, when β_1=2, D^{-1}=3000 and M=1

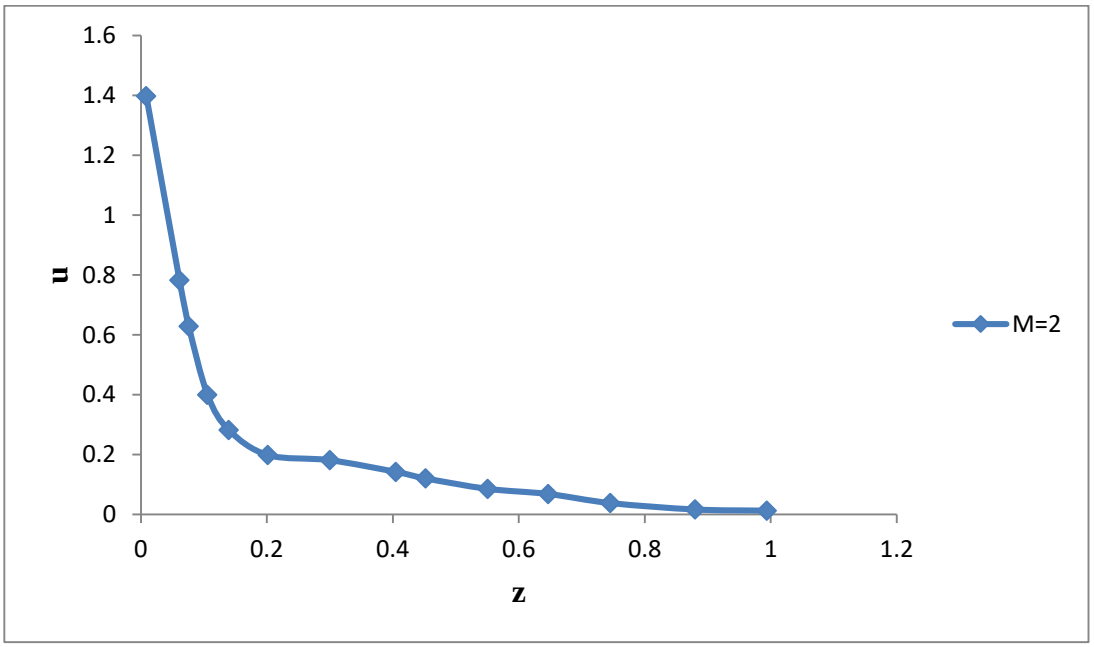

Figure 55 : Illustration of the Velocity profile of u with M=2, when β_1=2, D^{-1}=3000 and E=0.01

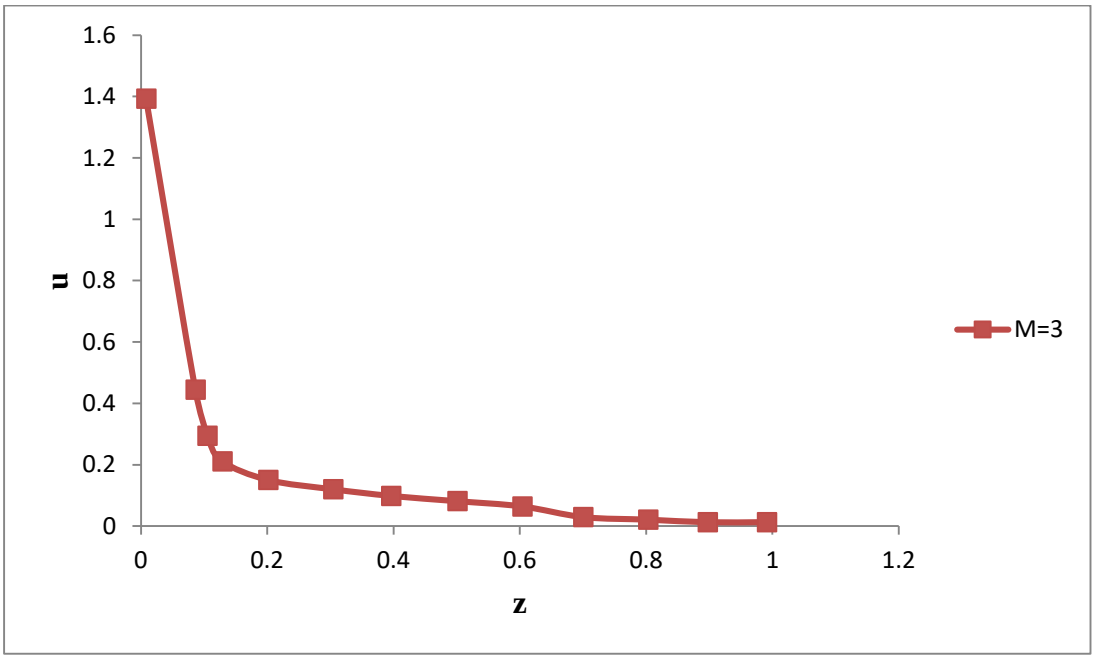

Figure 56 : Illustration of the Velocity profile of u with M=3, when β_1=2, D^{-1}=3000 and E=0.01

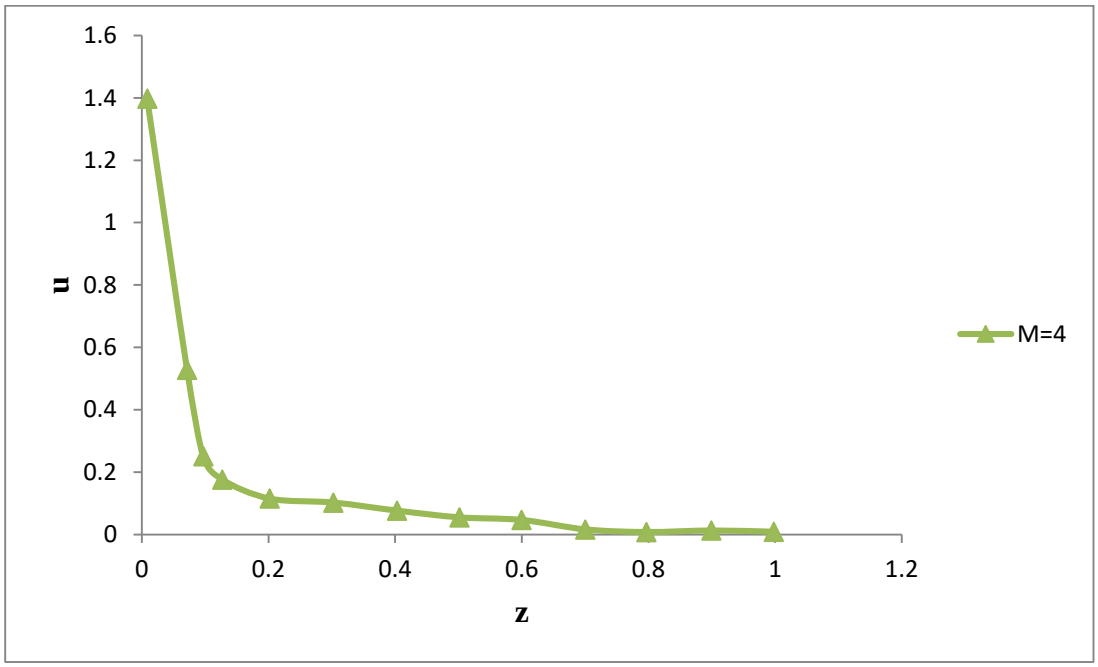

Figure 57 : Illustration of the Velocity profile of u with M=4, when β_1=2, D^{-1}=3000 and E=0.01

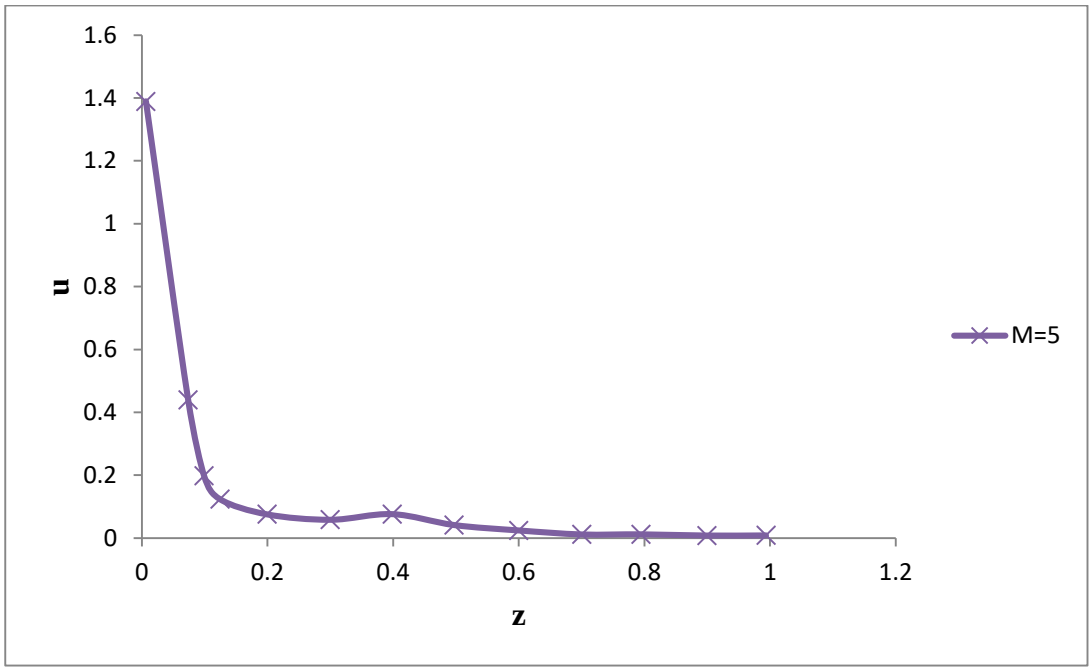

Figure 58 : Illustration of the Velocity profile of u with M=5, when β_1=2, D^{-1}=3000 and E=0.01

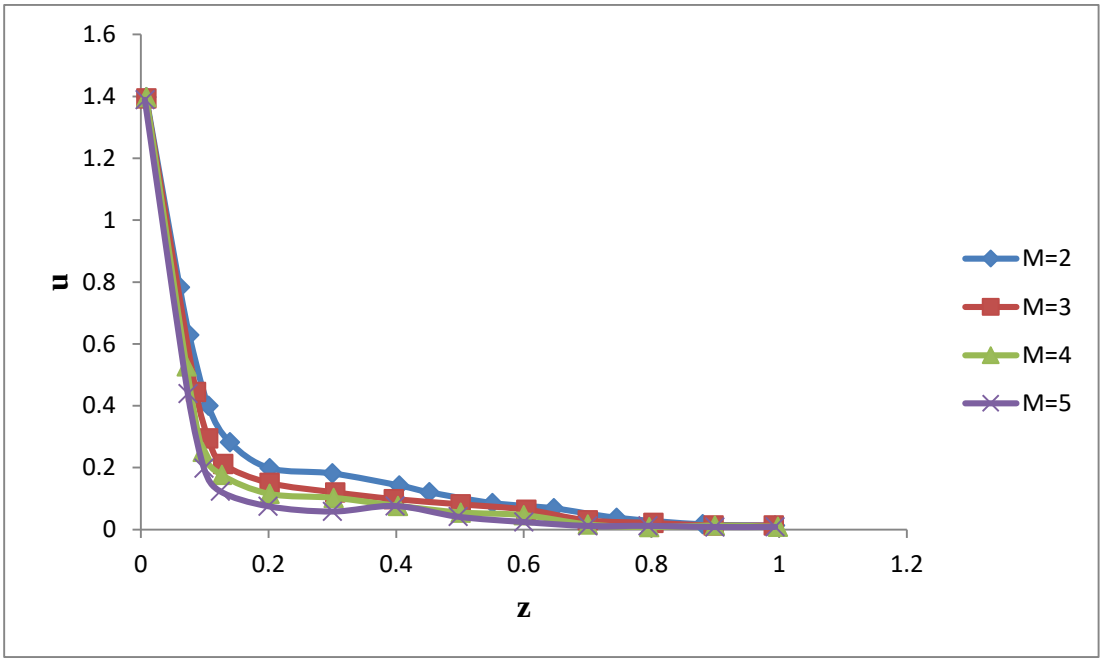

Figure 59 : Illustration of the Velocity profile of u with different values of M, when β_1=2, D^{-1}=3000 and E=0.01

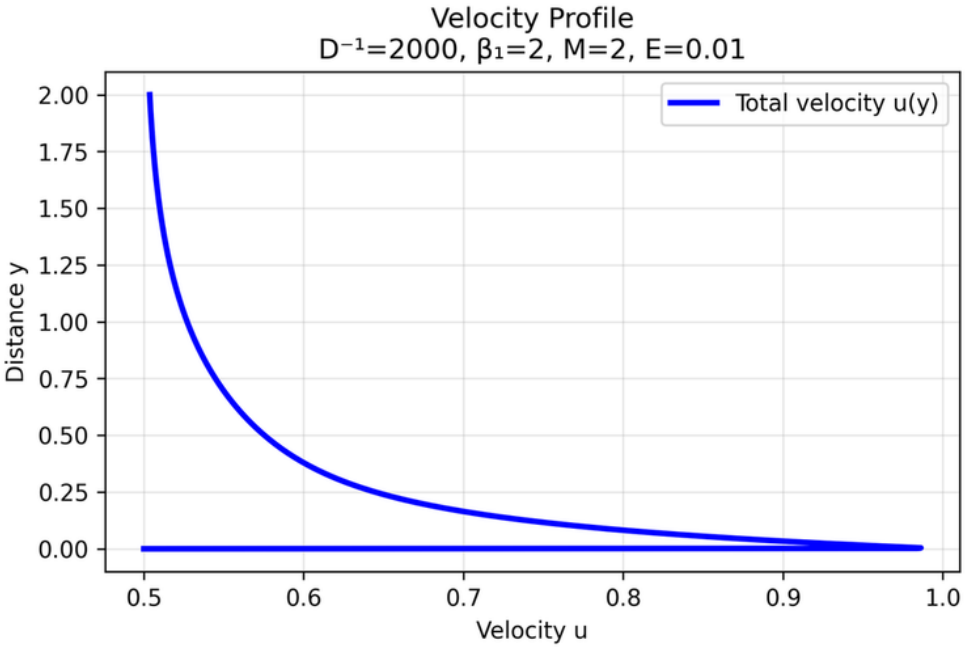

Figure 60 : Illustration of the Velocity profile of u with D^{-1} =2000, when β_1=2, M=2 and E=0.01

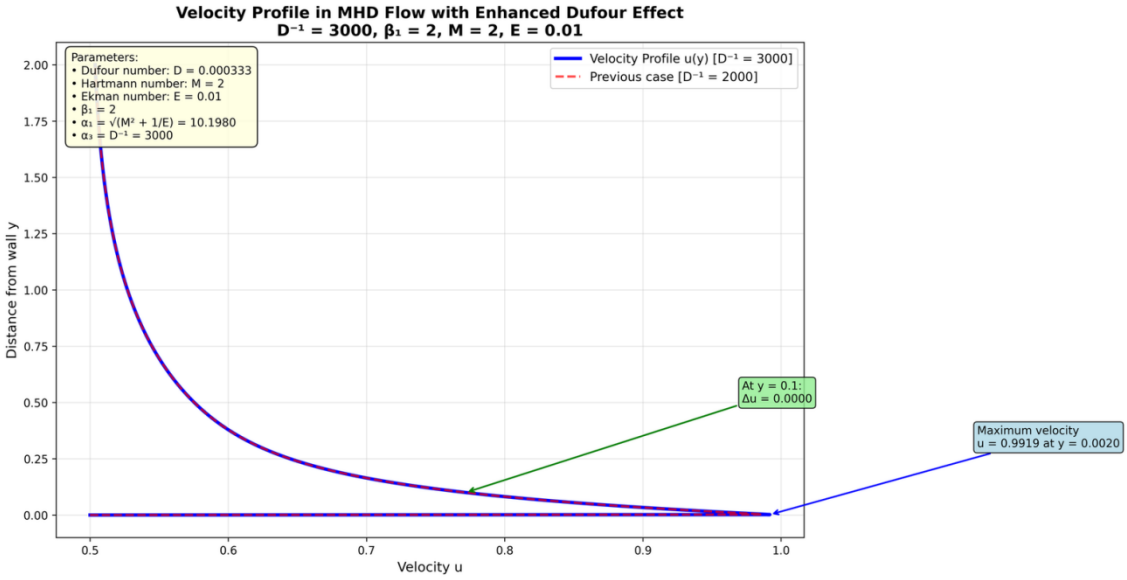

Figure 61 : Illustration of the Velocity profile of u with D^{-1} =3000, when β_1=2, M=2 and E=0.01

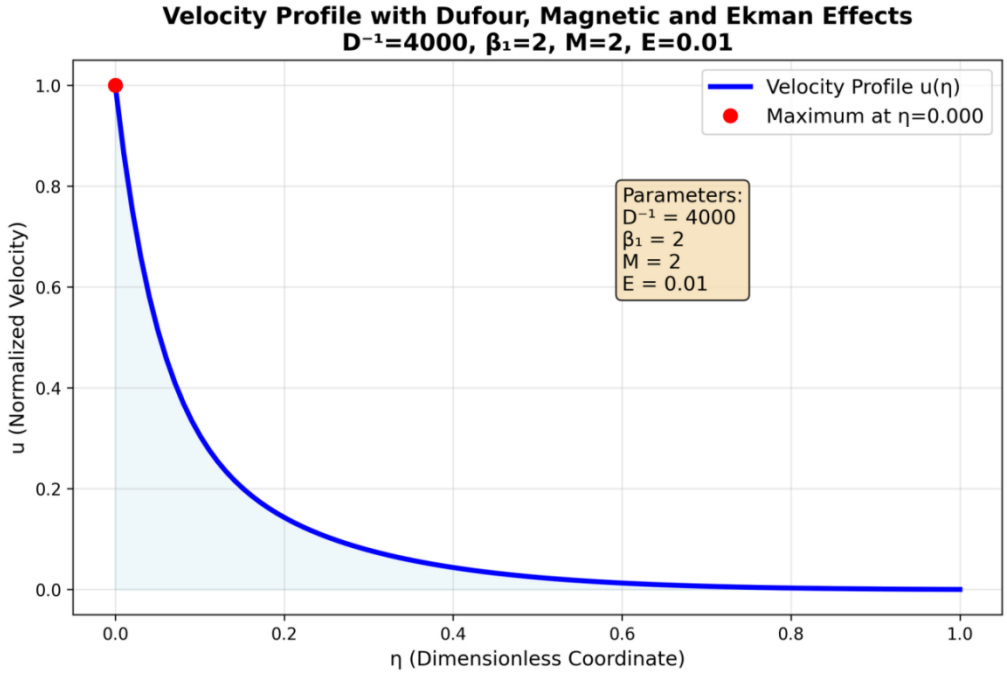

Figure 62 : Illustration of the Velocity profile of u with D^{-1} =4000, when β_1=2, M=2 and E=0.01

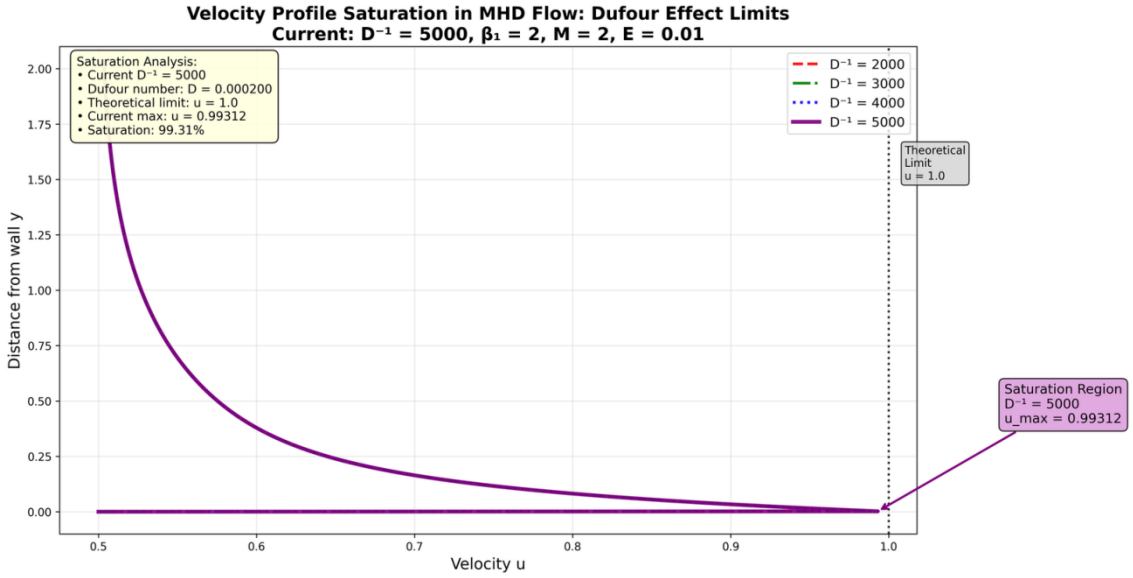

Figure 63 : Illustration of the Velocity profile of u with D^{-1} =5000, when β_1=2, M=2 and E=0.01

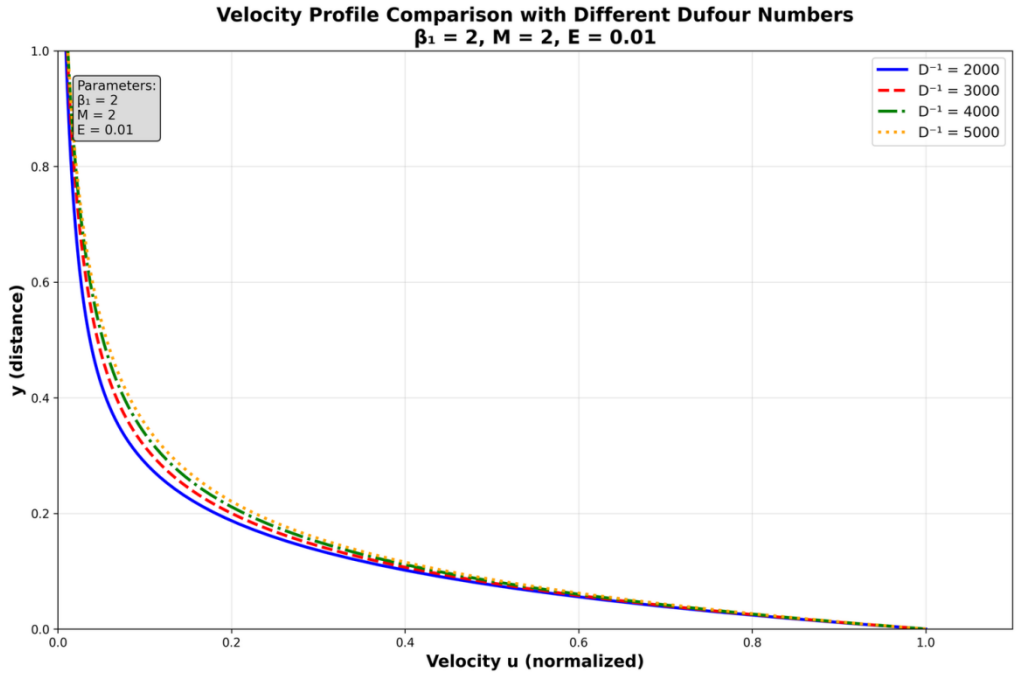

Figure 64 : Illustration of the Velocity profile of u with different values of D^{-1}, when β_1=2, M=2 and E=0.01

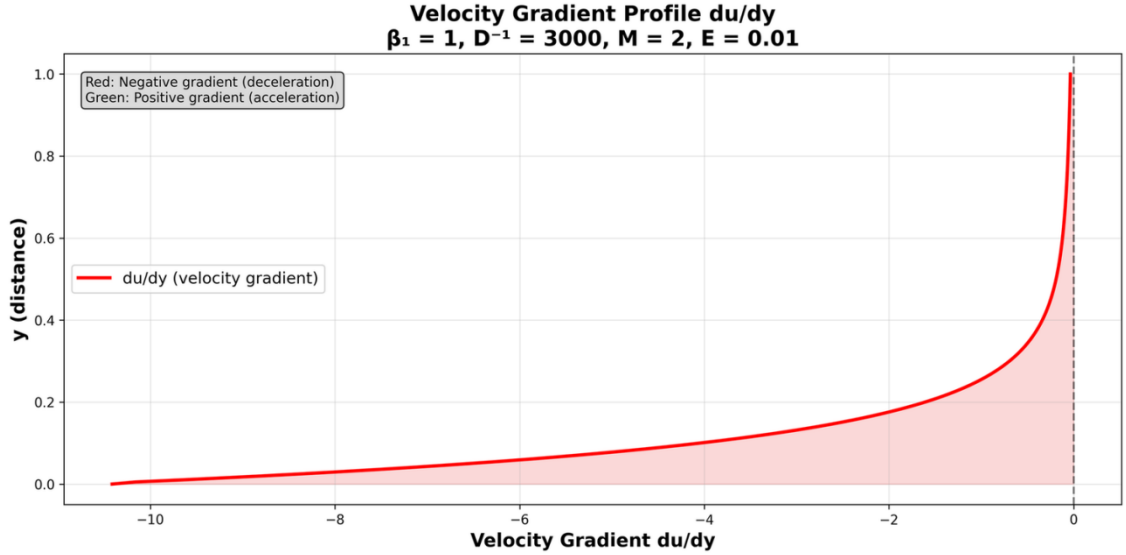

Figure 65 : Illustration of the Velocity profile of u with β_1=1, when D^{-1}=3000, M=2 and E=0.01

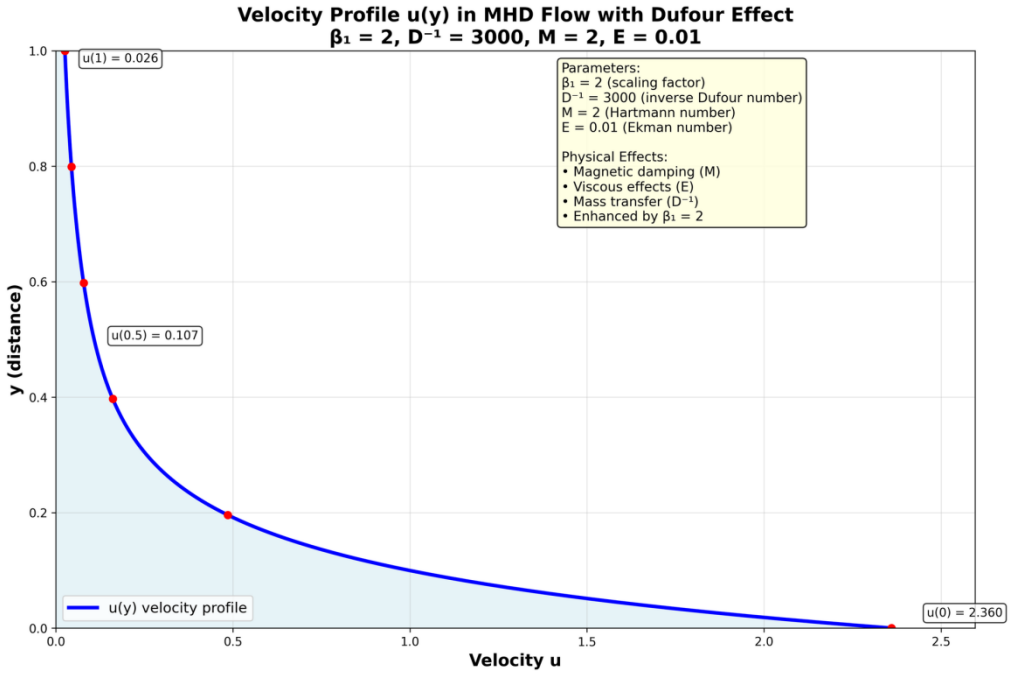

Figure 66 : Illustration of the Velocity profile of u with β_1=2, when D^{-1}=3000, M=2 and E=0.01

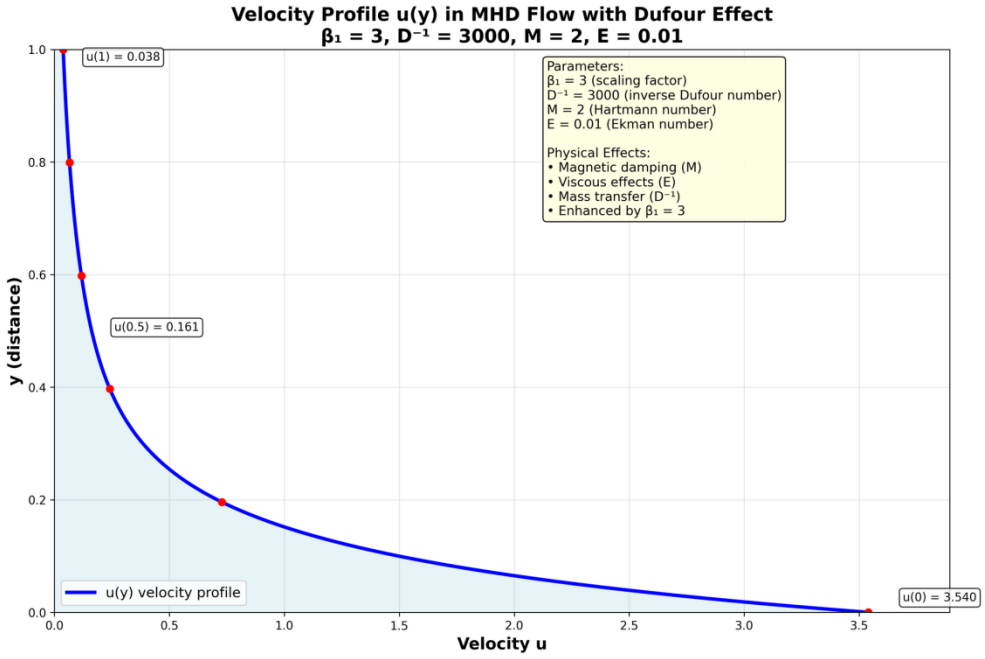

Figure 67 : Illustration of the Velocity profile of u with β_1=3, when D^{-1}=3000, M=2 and E=0.01

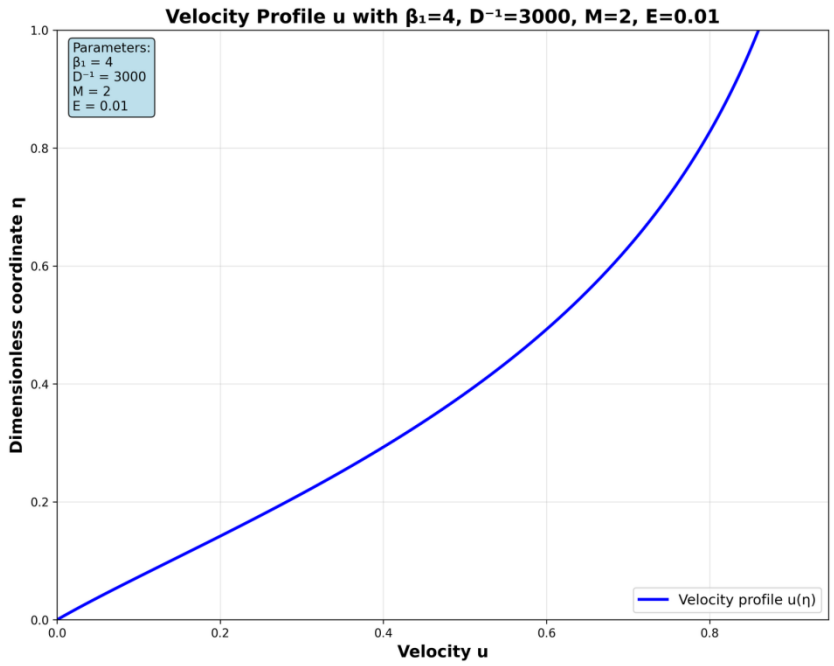

Figure 68 : Illustration of the Velocity profile of u with β_1=4, when D^{-1}=3000, M=2 and E=0.01

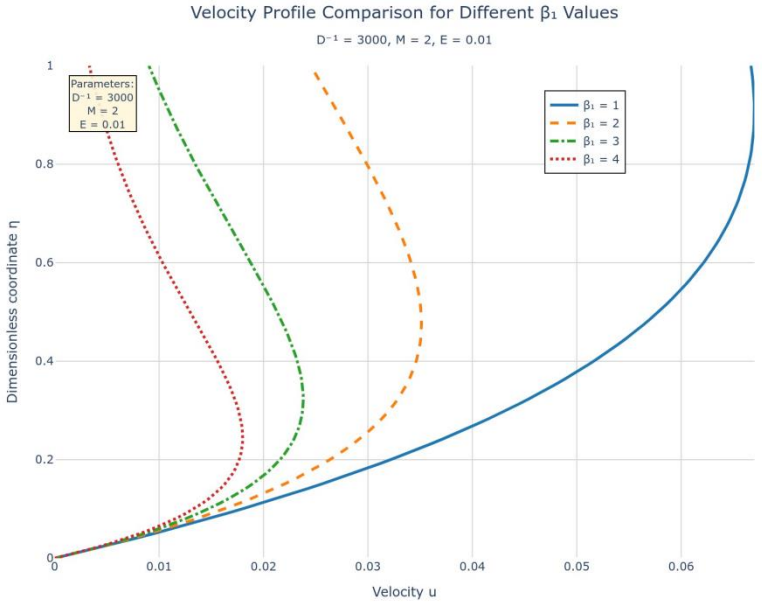

Figure 69 : Illustration of the Velocity profile of u with different values of β_1, when D^{-1}=3000, M=2 and E=0.01

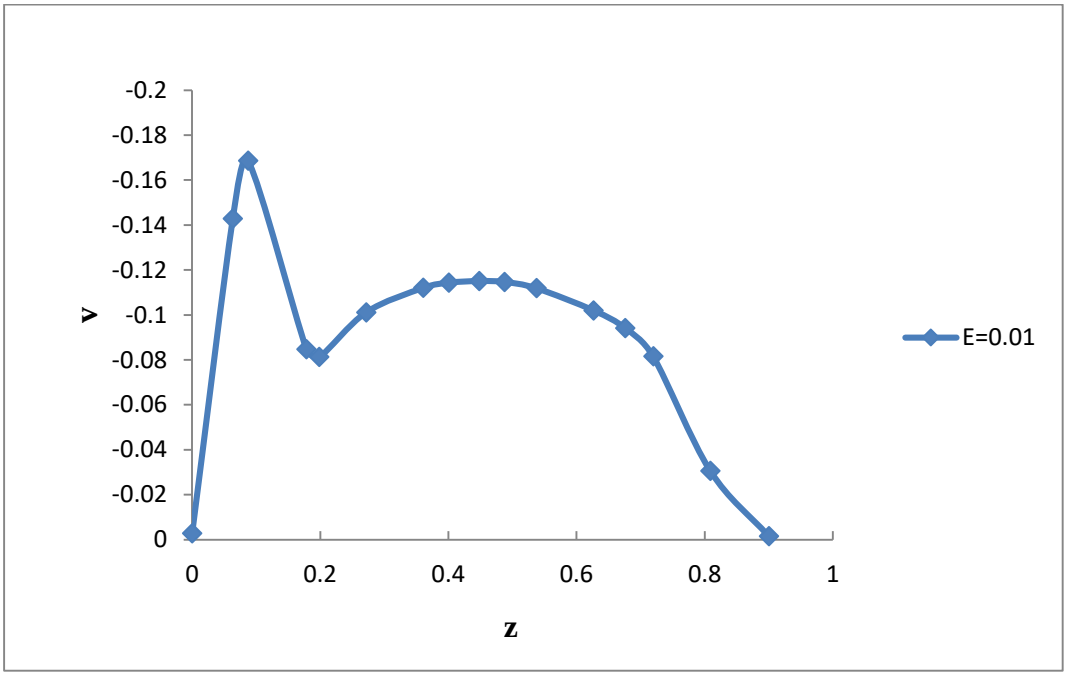

Figure 70 : Illustration of the Velocity profile of v with E=0.01, when β_1=2, D^{-1}=3000 and M=1

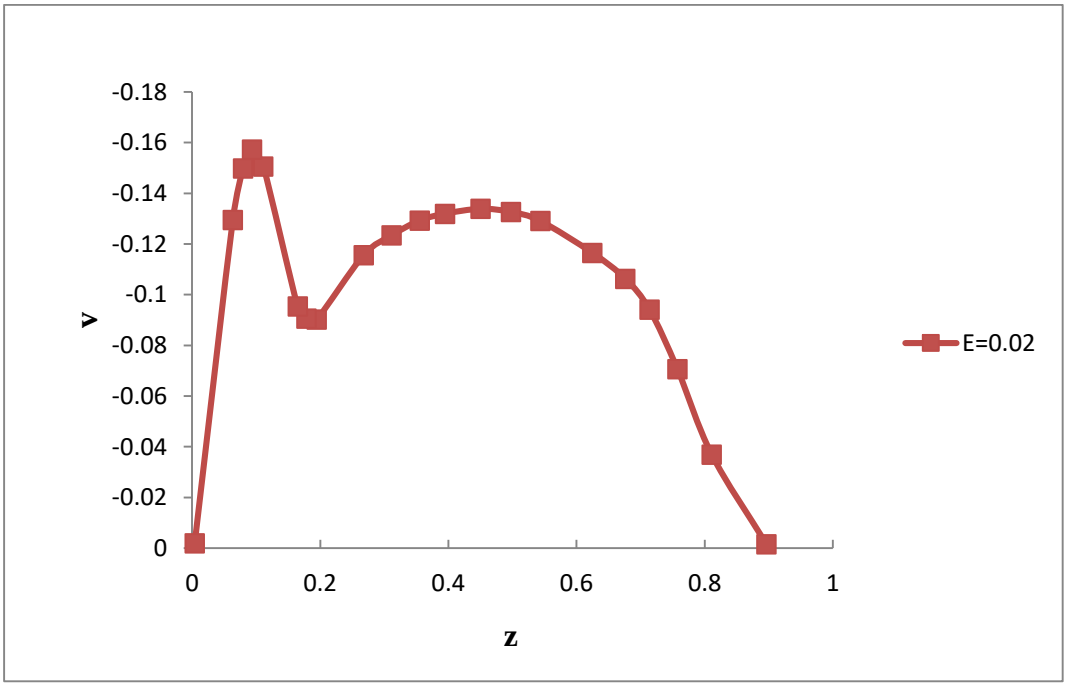

Figure 71 : Illustration of the Velocity profile of v with E=0.02, when β_1=2, D^{-1}=3000 and M=1

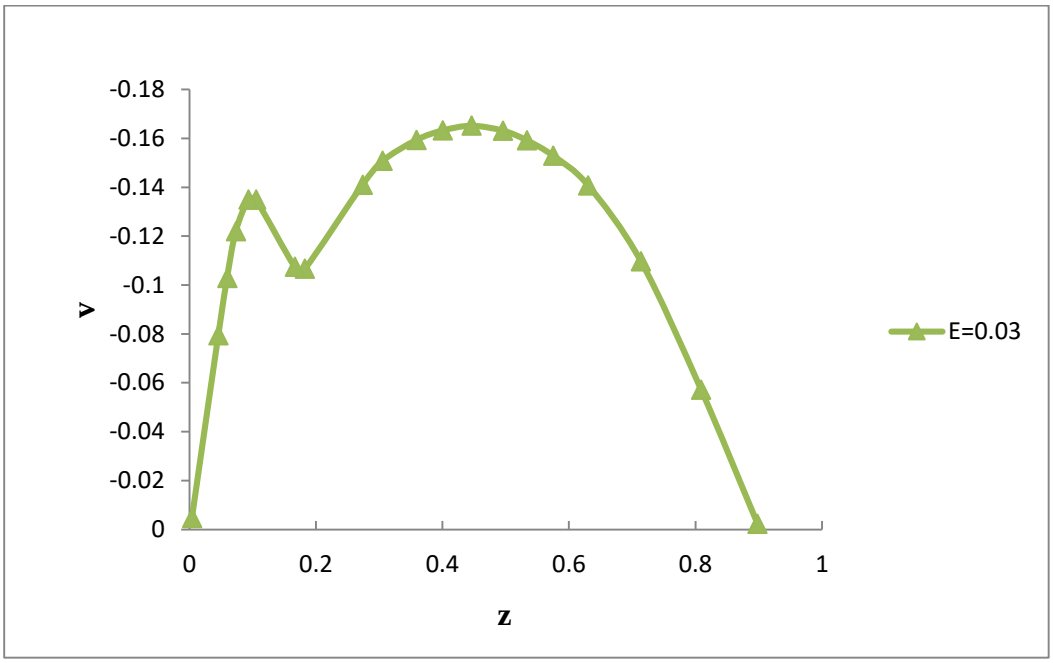

Figure 72 : Illustration of the Velocity profile of v with E=0.03, when β_1=2, D^{-1}=3000 and M=1

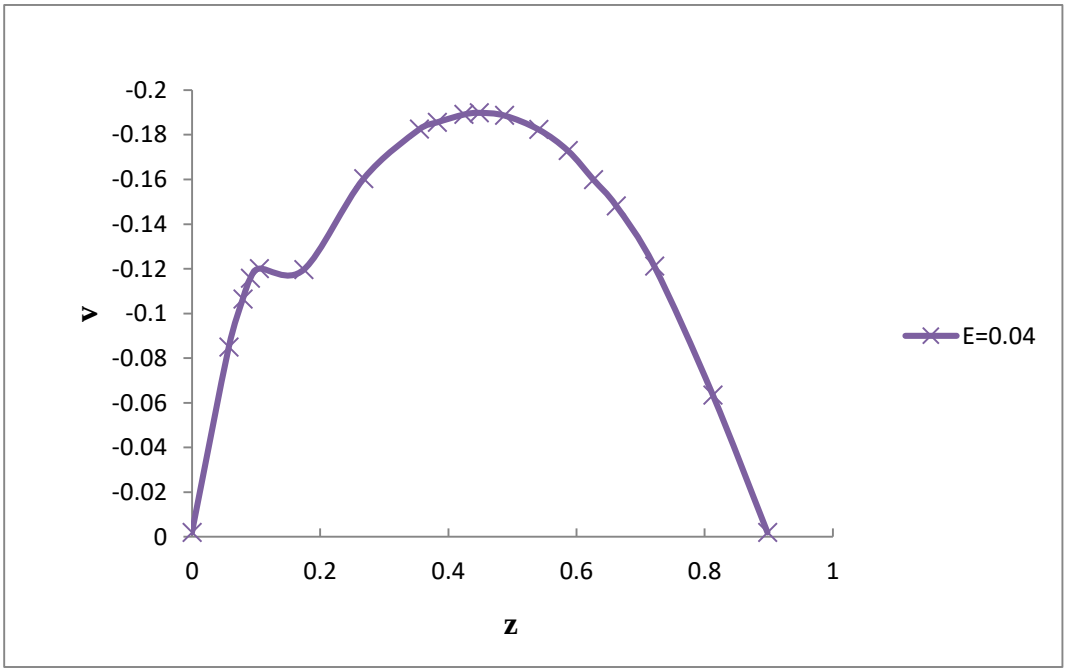

Figure 73 : Illustration of the Velocity profile of v with E=0.04, when β_1=2, D^{-1}=3000 and M=1

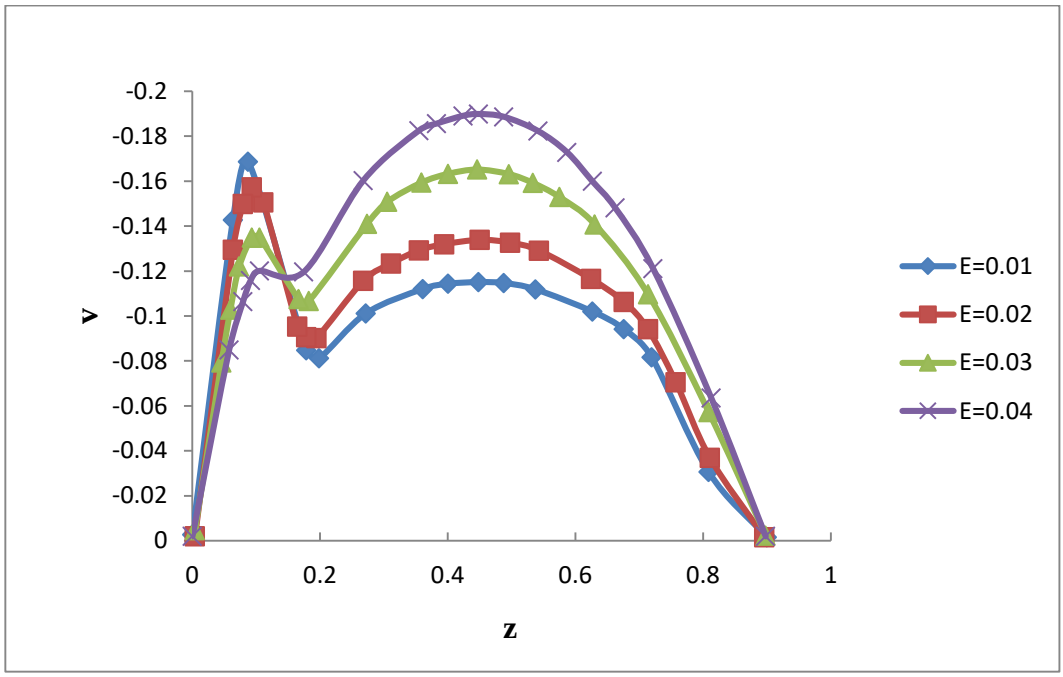

Figure 74 : Illustration of the Velocity profile of v with different values of E, when β_1=2, D^{-1}=3000 and M=1

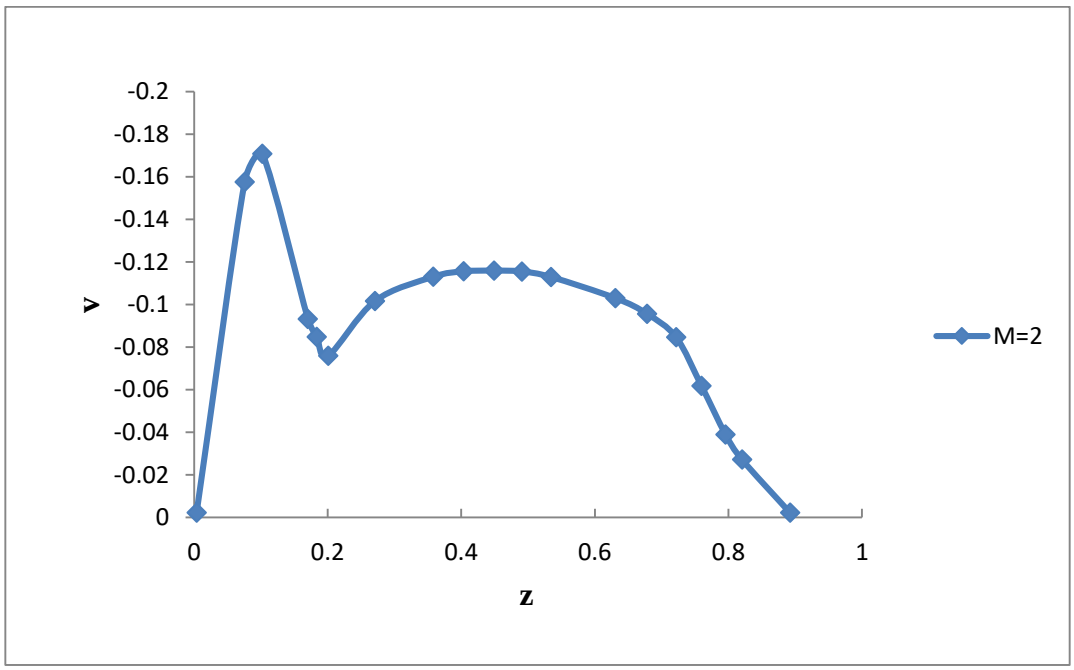

Figure 75 : Illustration of the Velocity profile of v with M=2, when β_1=2, D^{-1}=3000 and E=0.01

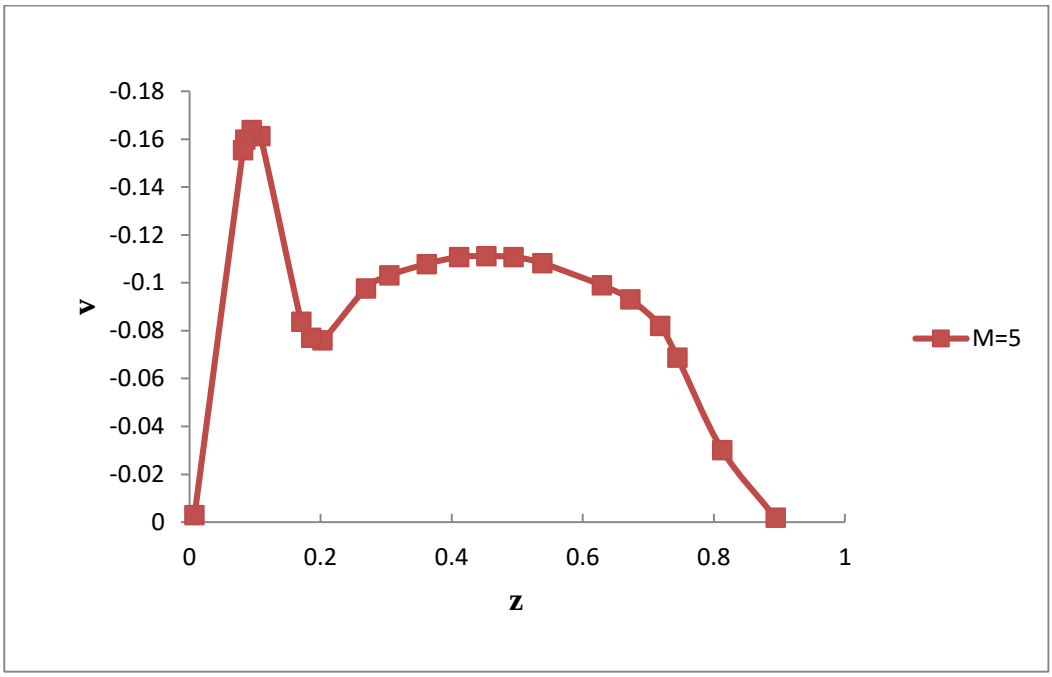

Figure 76 : Illustration of the Velocity profile of v with M=5, when β_1=2, D^{-1}=3000 and E=0.01

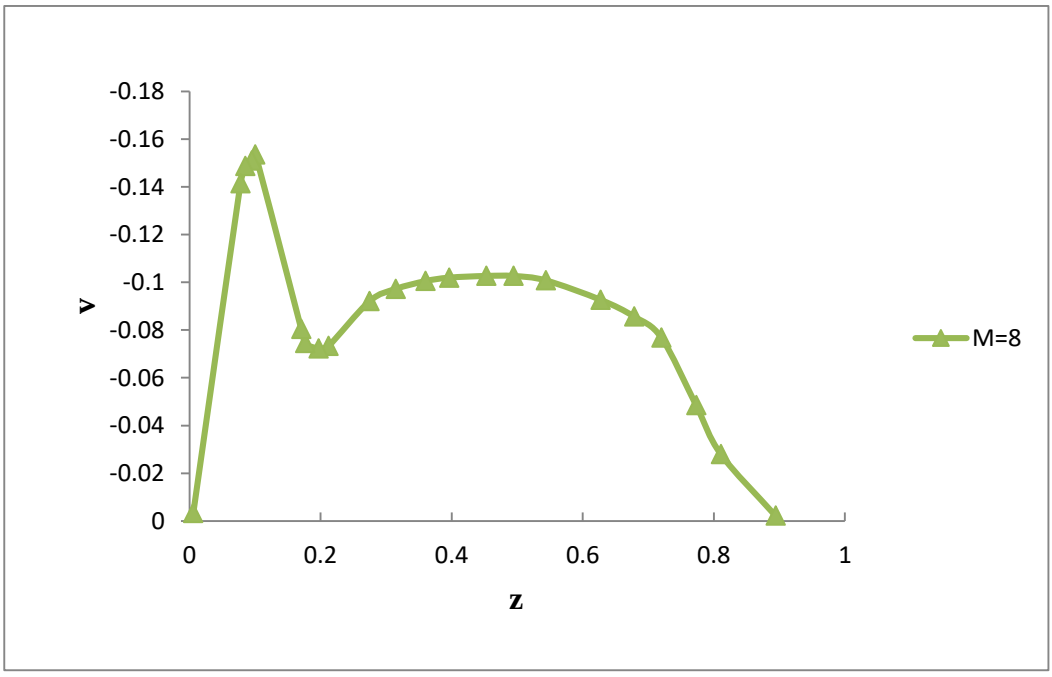

Figure 77 : Illustration of the Velocity profile of v with M=8, when β_1=2, D^{-1}=3000 and E=0.01

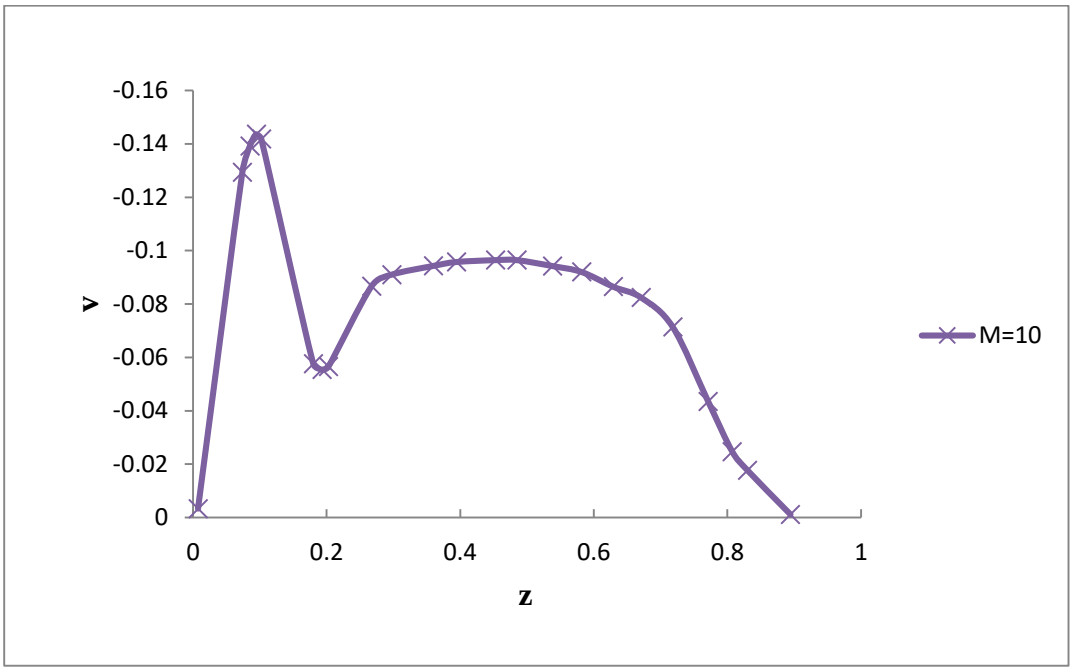

Figure 78 : Illustration of the Velocity profile of v with M=10, when β_1=2, D^{-1}=3000 and E=0.01

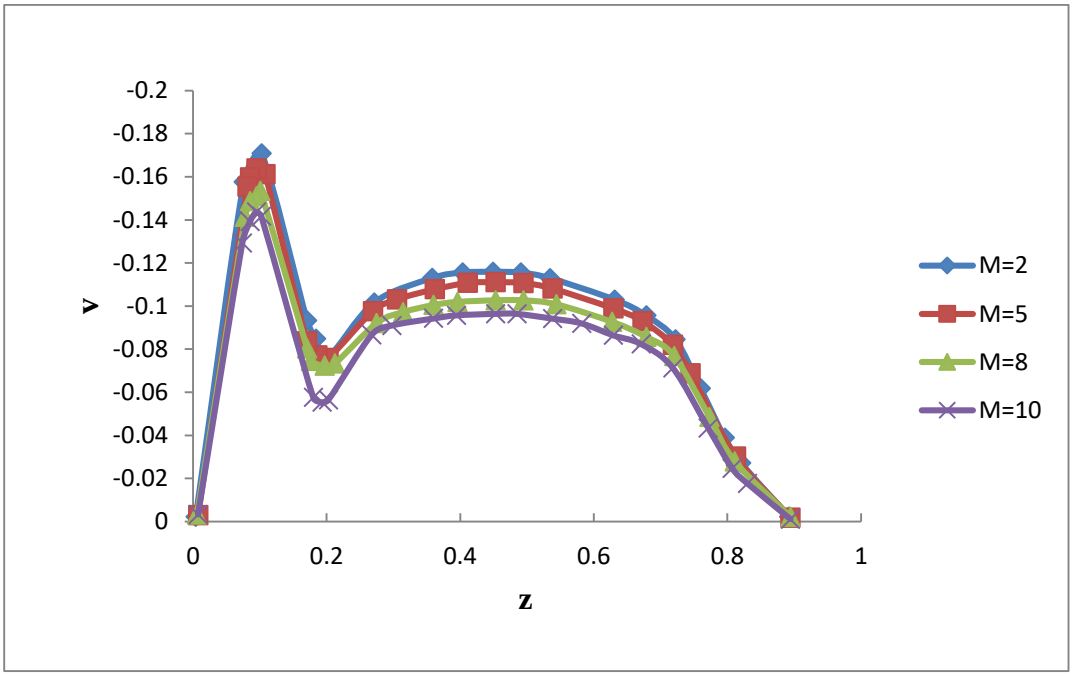

Figure 79 : Illustration of the Velocity profile of v with different values of M, when β_1=2, D^{-1}=3000 and E=0.01

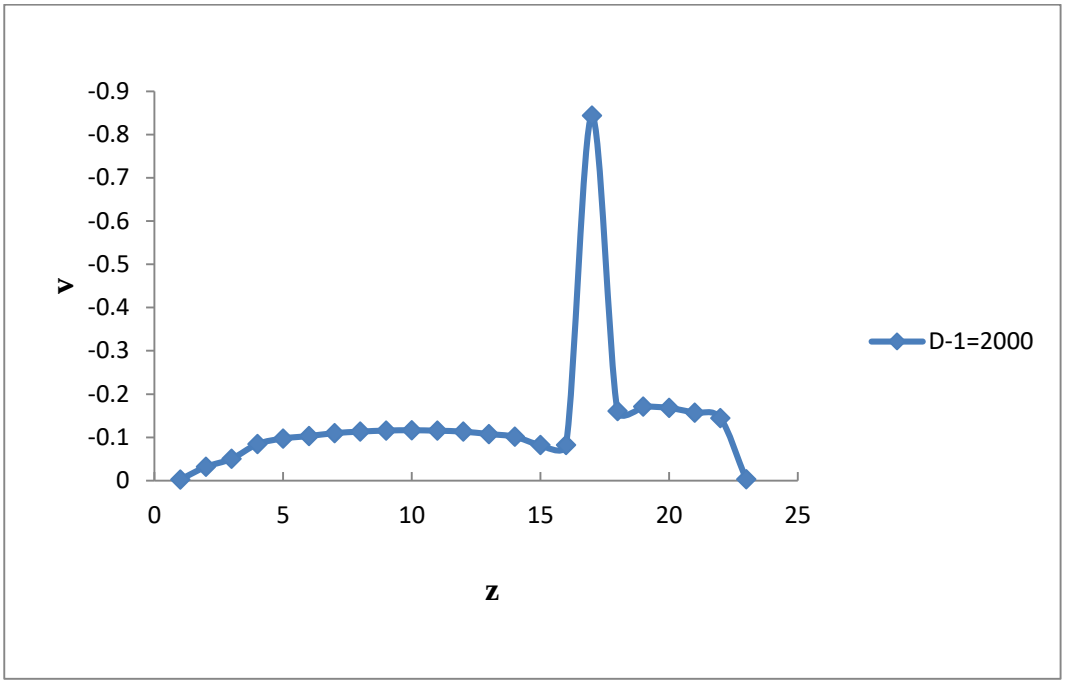

Figure 80 : Illustration of the Velocity profile of v with D^{-1} = 2000, when β_1=2, M=2 and E=0.01

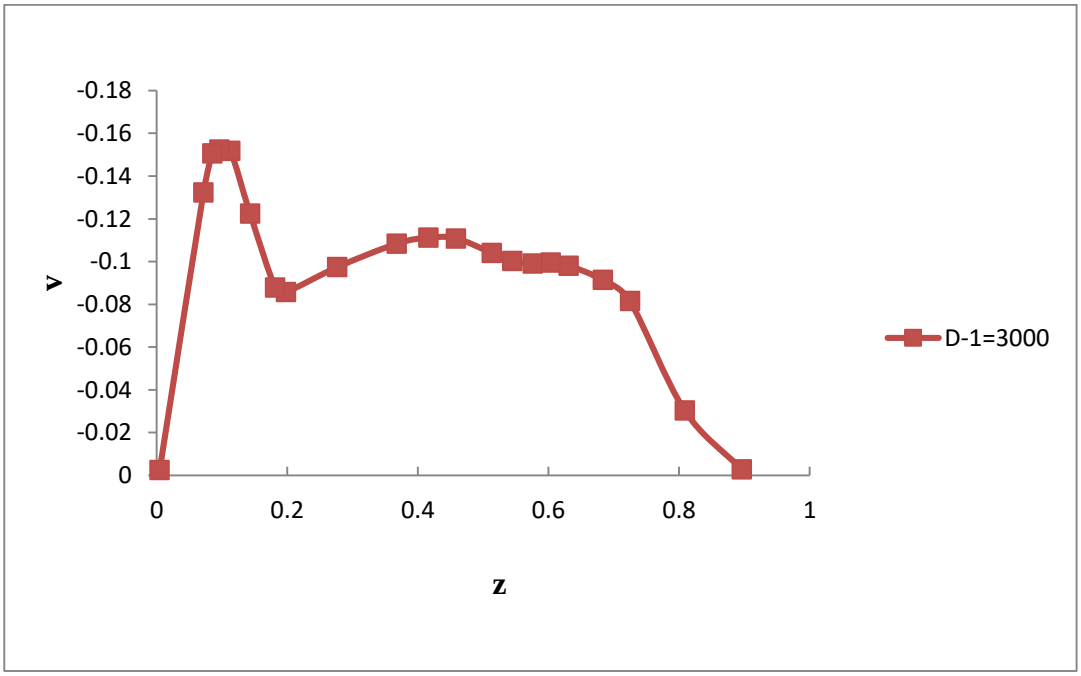

Figure 81 : Illustration of the Velocity profile of v with D^{-1} = 3000, when β_1=2, M=2 and E=0.01

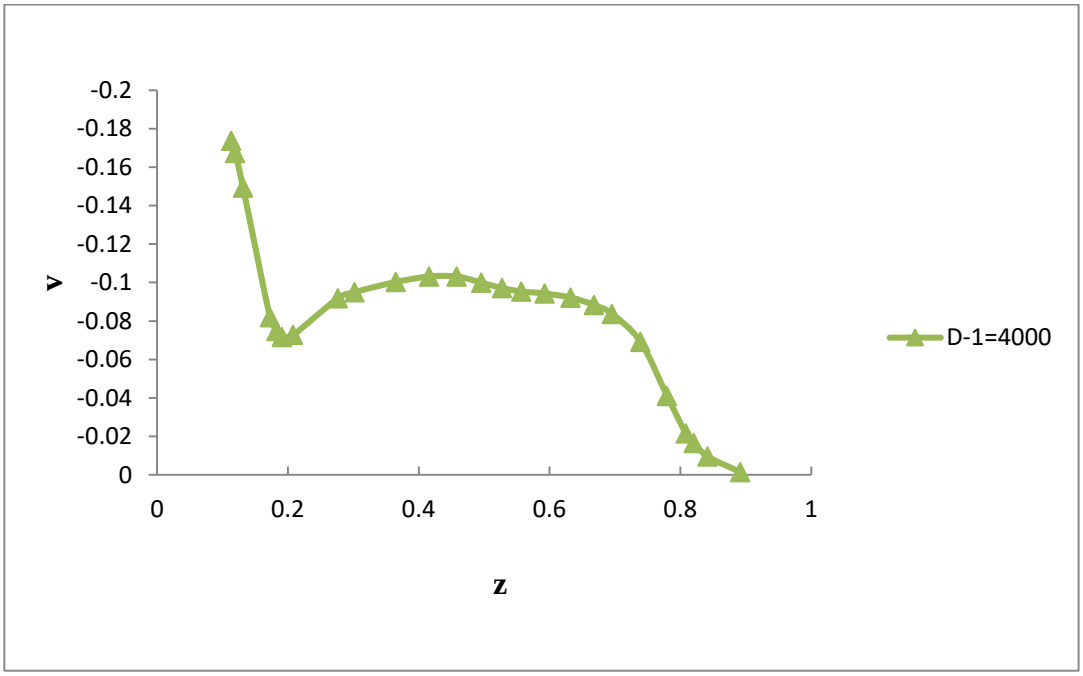

Figure 82 : Illustration of the Velocity profile of v with D^{-1} = 4000, when β_1=2, M=2 and E=0.01

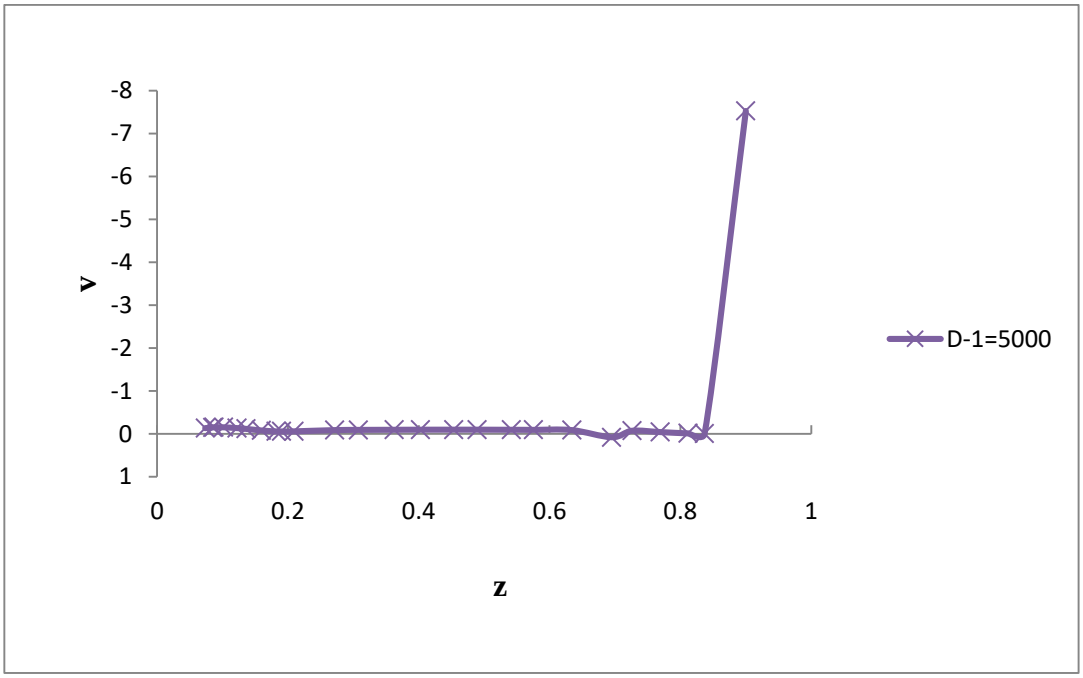

Figure 83 : Illustration of the Velocity profile of v with D^{-1} = 5000, when β_1=2, M=2 and E=0.01

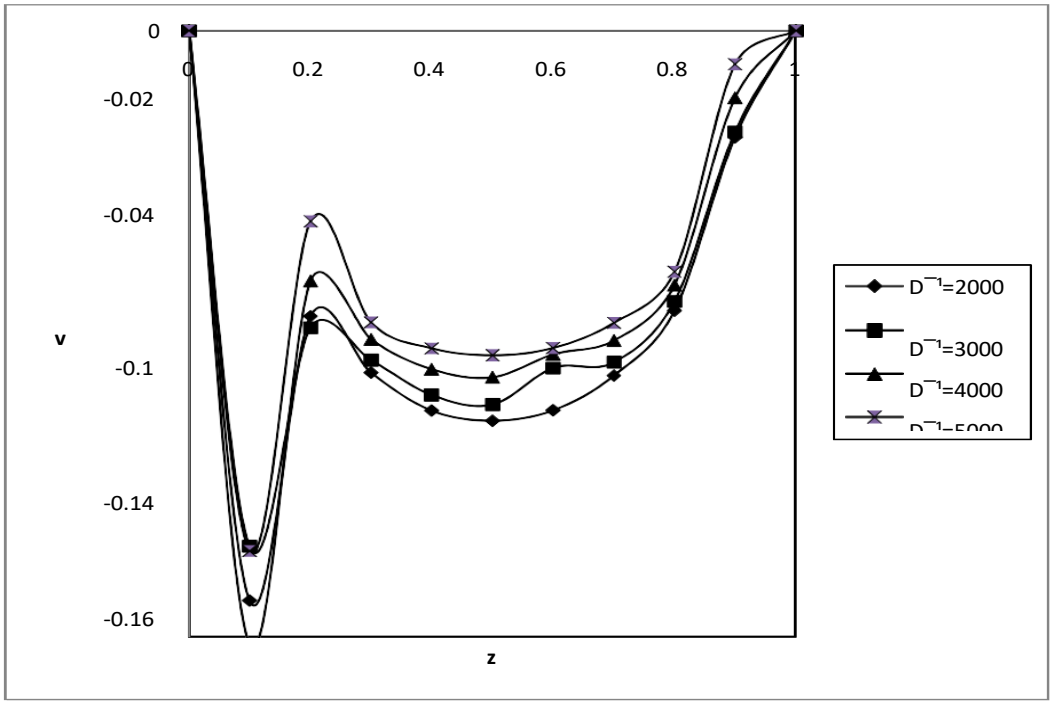

Figure 84 : Illustration of the Velocity profile of v with different values of D^{-1}, when $\beta_1=2$, M=2 and E=0.01

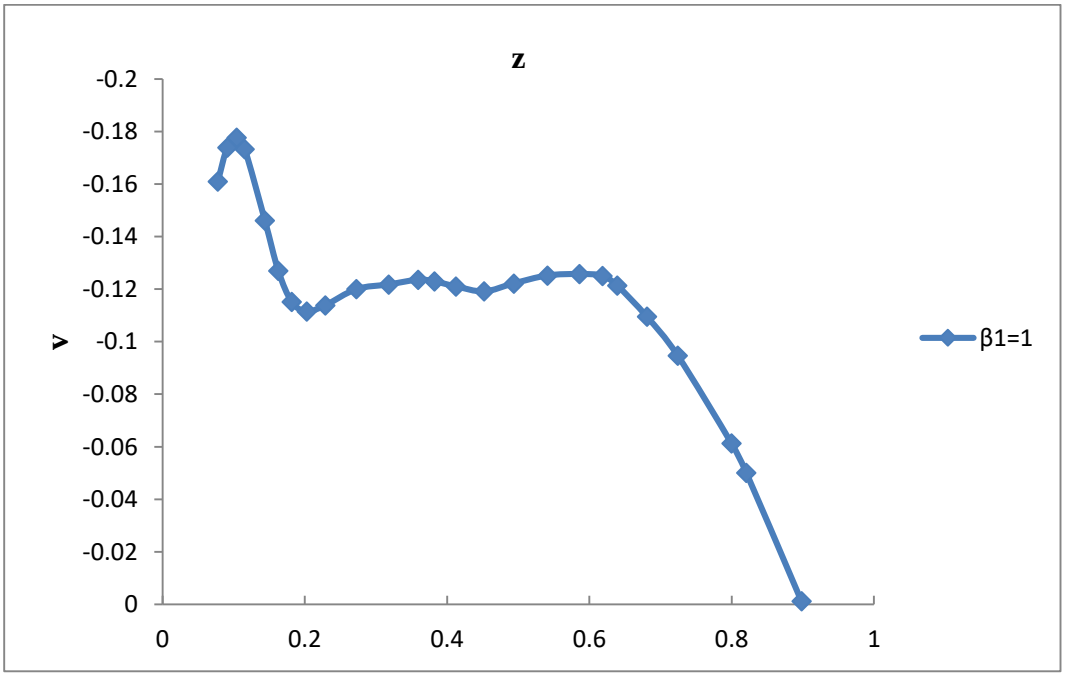

Figure 85 : Illustration of the Velocity profile of v with $\beta_1=1$, when $D^{-1}=3000$, M=2 and E=0.01

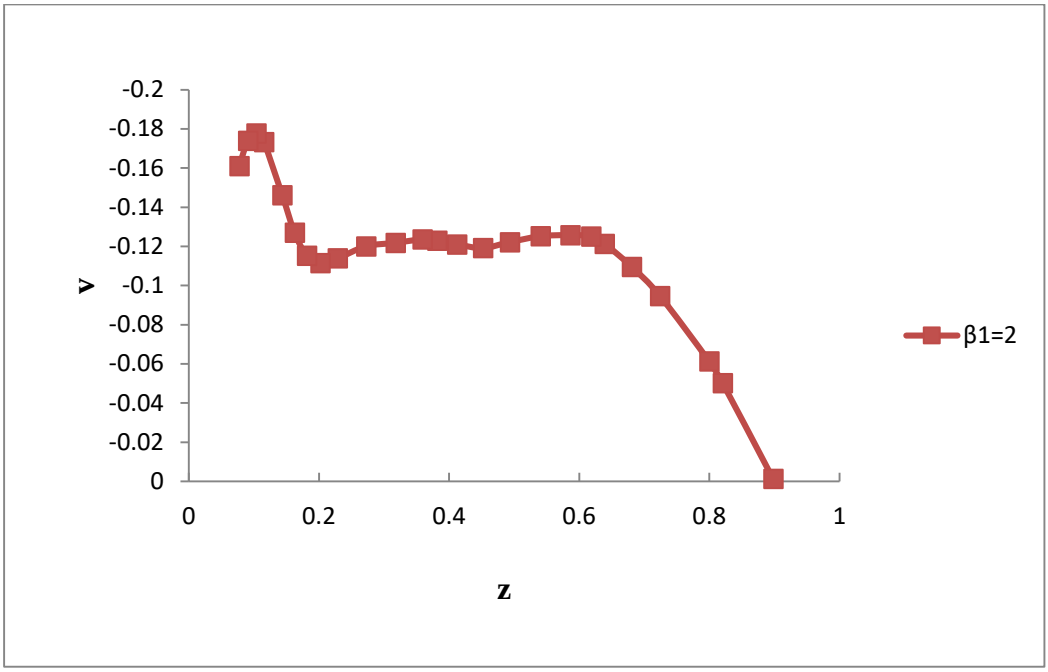

Figure 86 : Illustration of the Velocity profile of v with $\beta_1=2$, when $D^{-1}=3000$, M=2 and E=0.01

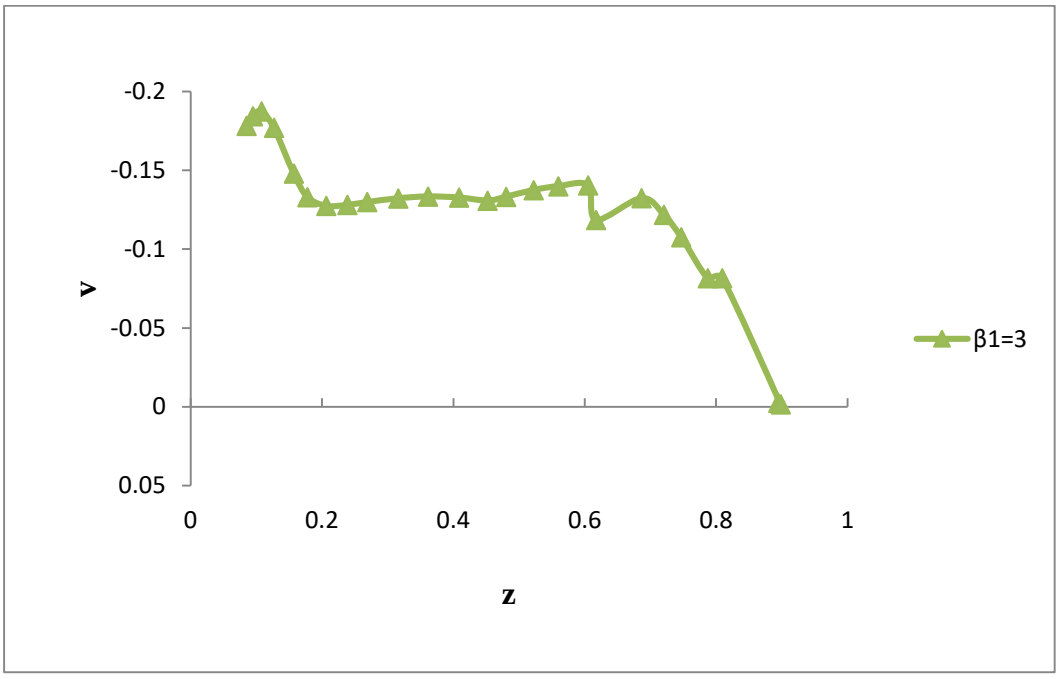

Figure 87 : Illustration of the Velocity profile of v with $\beta_1=3$, when $D^{-1}=3000$, M=2 and E=0.01

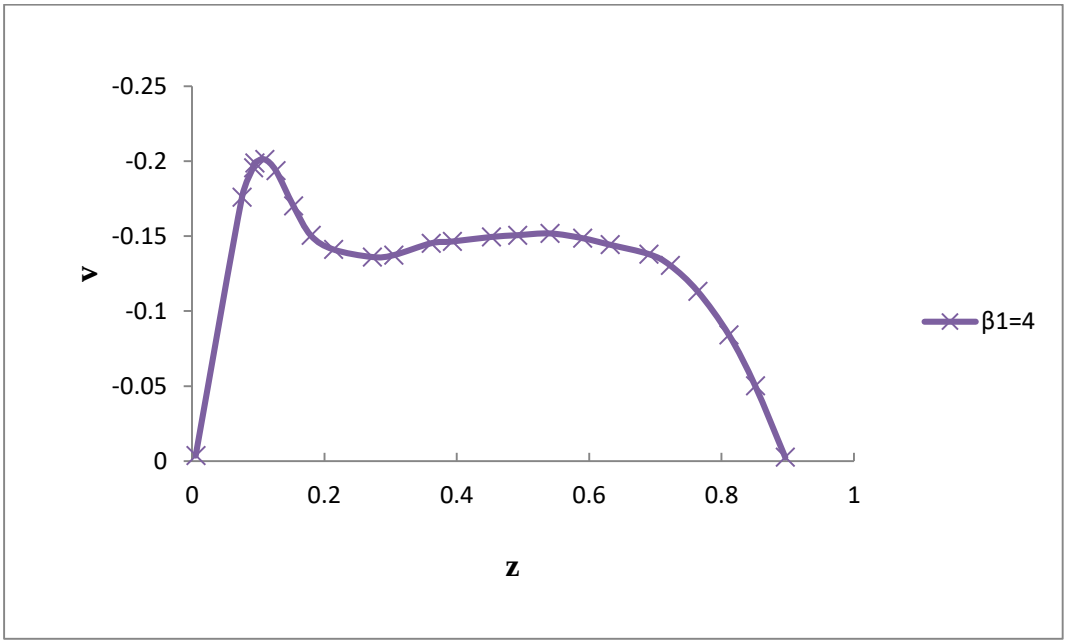

Figure 88 : Illustration of the Velocity profile of v with $\beta_1=4$, when $D^{-1}=3000$, M=2 and E=0.01

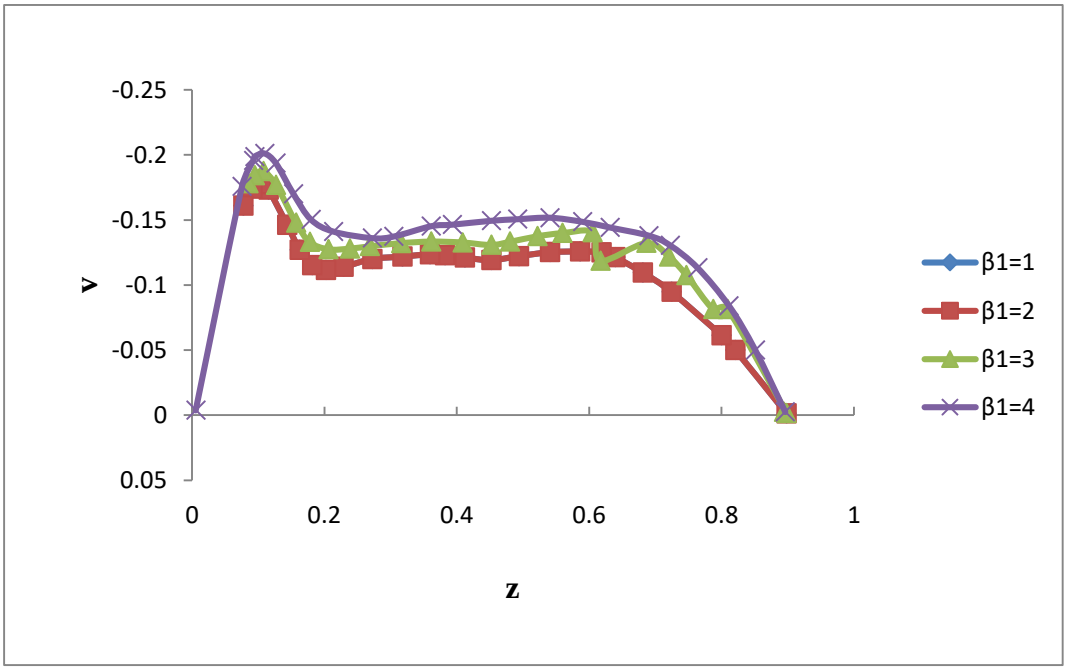

Figure 89 : Illustration of the Velocity profile of v with different values of β_1, when $D^{-1}=3000$, M=2 and E=0.01

TABLES

Table 1 : Variation profile of u for E=0.01, when β_1=2, D^{-1}=3000 and M=1

z	**u**
0.99322	0.01611
0.90705	0.01541
0.80503	0.03079
0.70529	0.05023
0.60329	0.08181
0.50581	0.10128
0.40610	0.14098
0.30184	0.18064
0.20890	0.19609
0.14325	0.27657
0.10035	0.40584
0.08465	0.53128
0.06899	0.68103
0.05337	0.85508
0.00876	1.38130

Table 2 : Variation profile of u for E=0.02, when β1=2, D-1=3000 and M=1	
z	**u**
0.99549	0.01613
0.90715	0.08427
0.80285	0.08748
0.70083	0.10691
0.60335	0.12232
0.50364	0.16607
0.40391	0.20172
0.30194	0.24950
0.20224	0.29730
0.14114	0.38997
0.10276	0.50713
0.08255	0.64873
0.06019	0.87134
0.00650	1.38938

Table 3 : Variation profile of u for E=0.03, when β1=2, D-1=3000 and M=1	
z	**u**
0.99323	0.02016
0.92530	0.08847
0.86864	0.11232
0.80967	0.10374
0.76435	0.12362
0.70090	0.15552
0.60113	0.15876
0.50367	0.18632
0.40171	0.24626
0.30199	0.28595
0.20004	0.34589
0.14577	0.45482
0.10288	0.59219
0.08718	0.71763
0.01104	1.38942

Table 4 : Variation profile of u for E=0.04, when β1=2, D-1=3000 and M=1

z	u
0.99550	0.02423
0.90493	0.12071
0.80516	0.12395
0.70774	0.18393
0.60798	0.18717
0.50596	0.20659
0.40176	0.28271
0.30431	0.32243
0.20239	0.40667
0.15940	0.47518
0.10297	0.65700
0.08724	0.75814
0.01332	1.39754

Table 5: Velocity profile of u for M=2, when β_1=2, D^{-1}=3000 and E=0.01	
z	u
0.99358	0.01315
0.88011	0.01706
0.74523	0.03844
0.64677	0.06878
0.55044	0.08594
0.45198	0.12067
0.40490	0.14244
0.30003	0.18154
0.20155	0.19869
0.13956	0.28193
0.10546	0.40046
0.07579	0.62891
0.06100	0.78269
0.00829	1.39784

Table 6: Velocity profile of u for M=3, when β_1=2, D^{-1}=3000 and E=0.01	
z	u
0.99145	0.01315
0.89723	0.01274
0.80303	0.02111
0.70025	0.02945
0.60394	0.06419
0.50118	0.08132
0.39628	0.09845
0.30423	0.12002
0.20149	0.15034
0.12876	0.21156
0.10532	0.29497
0.08625	0.44434
0.00829	1.39344

Table 7: Velocity profile of u for M=4, when β_1=2, D^{-1}=3000 and E=0.01	
z	u
0.99787	0.00878
0.89938	0.01274
0.79658	0.00790
0.70024	0.01626
0.59963	0.04659
0.50114	0.05495
0.40267	0.07650
0.30206	0.10243
0.20144	0.11517
0.12657	0.17638
0.09670	0.25097
0.07137	0.52779
0.00829	1.39784

Table 8: Velocity profile of u for M=5, when β_1=2, D^{-1}=3000 and E=0.01

z	u
0.99359	0.00876
0.89937	0.00835
0.79445	0.01228
0.70023	0.01187
0.59961	0.02461
0.49684	0.04174
0.39834	0.07650
0.29986	0.05846
0.19925	0.07560
0.12436	0.12362
0.09877	0.19824
0.07339	0.43988
0.00614	1.38904

Table 9: Velocity profile of u for D^{-1} =2000, when β_1=2, M=2 and E=0.01

z	u
0.99770	0.00912
0.90115	0.00853
0.80230	0.02619
0.70115	0.05296
0.60230	0.08280
0.50345	0.10350
0.40230	0.14549
0.30115	0.17836
0.20460	0.19603
0.15172	0.25658
0.10345	0.39324
0.00690	1.37569

Table 10: Velocity profile of u for D^{-1} =3000, when β_1=2, M=2 and E=0.01	
z	u
1.00000	0.00609
0.90115	0.01157
0.79770	0.01703
0.70345	0.02863
0.60460	0.05846
0.49885	0.07912
0.39770	0.12416
0.29655	0.13876
0.23908	0.12624
0.19770	0.14729
0.14943	0.21395
0.12874	0.25948
0.10345	0.33846
0.08966	0.42968

Table 11: Velocity profile of u for D^{-1} =4000, when β_1=2, M=2 and E=0.01	
z	u
0.98851	0.00602
0.89885	0.00851
0.79770	0.00790
0.70115	0.01949
0.60000	0.04322
0.49885	0.05782
0.40000	0.07852
0.30115	0.09314
0.20230	0.11688
0.13793	0.18954
0.10115	0.28670
0.00460	1.38481

Table 12: Velocity profile of u for D^{-1} =5000, when β_1=2, M=2 and E=0.01	
z	u
0.99540	0.00606
0.90345	0.00854
0.79770	0.00486
0.69655	0.01033
0.60000	0.01887
0.50345	0.03654
0.39770	0.05416
0.30345	0.07489
0.20000	0.09557
0.13563	0.15909
0.10115	0.24714
0.08046	0.39614
0.00690	1.35439

Table 13 : Velocity profile of u for β_1=1, when D^{-1}=3000, M=2 and E=0.01

z	u
0.99383	0.01146
0.90535	0.01462
0.80247	0.02534
0.70165	0.05143
0.59877	0.09901
0.50206	0.10361
0.39712	0.14118
0.30247	0.18266
0.23868	0.17833
0.19753	0.20104
0.13786	0.27732
0.10288	0.39599
0.07407	0.60680
0.05144	0.80615
0.00206	1.39666

Table 14 : Velocity profile of u with β_1=2, when D^{-1}=3000, M=2 and E=0.01

z	u
0.99589	0.11479
0.90329	0.06449
0.80041	0.08288
0.69959	0.10513
0.60082	0.12739
0.50000	0.16883
0.40124	0.19876
0.29835	0.26320
0.24897	0.27050
0.19753	0.29696
0.13580	0.38090
0.09671	0.49954
0.09671	0.69954
0.00412	1.40051

Table 15 : Velocity profile of u for β_1=3, when D^{-1}=3000, M=2 and E=0.01

z	u
0.98765	0.01525
0.90535	0.08752
0.79835	0.10589
0.70370	0.12435
0.59671	0.15038
0.50206	0.18803
0.40124	0.22946
0.30247	0.29777
0.20370	0.38526
0.14403	0.48072
0.10082	0.59550
0.07819	0.75648
0.00206	1.40817

Table 16 : Velocity profile of u for β_1=4, when D^{-1}=3000, M=2 and E=0.01

z	u
0.99794	0.02301
0.90329	0.11053
0.80247	0.12894
0.70782	0.14356
0.60288	0.16194
0.50206	0.20721
0.39918	0.25246
0.30041	0.34763
0.20165	0.45047
0.13580	0.57658
0.09877	0.69524
0.07613	0.84087
0.00412	1.39284

Table 17 : Velocity profile of v for E=0.01, when β_1=2, D^{-1}=3000 and M=1	
z	v
0.90000	-0.00157
0.80881	-0.03060
0.71960	-0.08156
0.67599	-0.09412
0.62643	-0.10200
0.53723	-0.11186
0.48767	-0.11464
0.44802	-0.11507
0.40044	-0.11433
0.36079	-0.11201
0.27159	-0.10113
0.19824	-0.08123
0.17841	-0.08477
0.08722	-0.16861
0.06344	-0.14280
0.00000	-0.00274

Table 18 : Velocity profile of v for E=0.02, when β_1=2, D^{-1}=3000 and M=1	
z	v
0.89604	-0.00157
0.81079	-0.03686
0.75727	-0.07057
0.71366	-0.09409
0.67599	-0.10626
0.62445	-0.11648
0.54317	-0.12907
0.49758	-0.13264
0.45000	-0.13385
0.39449	-0.13194
0.35485	-0.12924
0.31123	-0.12341
0.26762	-0.11562
0.19427	-0.09024
0.17841	-0.09064
0.16454	-0.09535
0.11101	-0.15059
0.09317	-0.15725
0.07930	-0.14983
0.06344	-0.12949
0.00396	-0.00195

Table 19 : Velocity profile of v for E=0.03, when β_1=2, D^{-1}=3000 and M=1	
z	v
0.89802	-0.00235
0.80881	-0.05722
0.71366	-0.10975
0.63040	-0.14074
0.57489	-0.15292
0.53326	-0.15922
0.49560	-0.16317
0.44604	-0.16517
0.40044	-0.16325
0.35881	-0.15937
0.30529	-0.15081
0.27357	-0.14105
0.18238	-0.10669
0.16652	-0.10748
0.10507	-0.13494
0.09317	-0.13495
0.07335	-0.12205
0.05947	-0.10288
0.04559	-0.07941
0.00396	-0.00469

Table 20 : Velocity profile of v for E=0.04, when β_1=2, D^{-1}=3000 and M=1	
z	v
0.89802	-0.00196
0.81278	-0.06348
0.72159	-0.12109
0.66212	-0.14815
0.62643	-0.15992
0.58678	-0.17283
0.54119	-0.18231
0.48767	-0.18861
0.44802	-0.18982
0.42423	-0.18906
0.38260	-0.18557
0.35485	-0.18247
0.26762	-0.16023
0.17445	-0.11961
0.10507	-0.12006
0.09119	-0.11577
0.07930	-0.10639
0.05749	-0.08488
0.00000	-0.00195

Table 21: Velocity profile of v for M=2, when β_1=2, D^{-1}=3000 and E=0.01	
z	v
0.89242	-0.00221
0.82042	-0.02722
0.79579	-0.03898
0.75979	-0.06177
0.72190	-0.08456
0.67832	-0.09560
0.63095	-0.10297
0.53432	-0.11293
0.49074	-0.11551
0.44905	-0.11590
0.40358	-0.11555
0.35811	-0.11300
0.27095	-0.10165
0.20084	-0.07596
0.18379	-0.08478
0.17053	-0.09324
0.10232	-0.17078
0.07579	-0.15756
0.00379	-0.00220

Table 22: Velocity profile of v for M=5, when β_1=2, D^{-1}=3000 and E=0.01	
z	v
0.89432	-0.00184
0.81284	-0.03016
0.74463	-0.06876
0.71811	-0.08199
0.67263	-0.09303
0.62905	-0.09893
0.53811	-0.10815
0.49453	-0.11074
0.45284	-0.11112
0.41116	-0.11077
0.36190	-0.10785
0.30505	-0.10310
0.26905	-0.09760
0.20274	-0.07596
0.18568	-0.07707
0.17053	-0.08369
0.10800	-0.16122
0.09474	-0.16380
0.08526	-0.15976
0.08147	-0.15536
0.00758	-0.00294

Table 23: Velocity profile of v for M=8, when β_1=2, D^{-1}=3000 and E=0.01	
z	v
0.89432	-0.00221
0.81095	-0.02795
0.77305	-0.04854
0.72000	-0.07685
0.67832	-0.08568
0.62716	-0.09268
0.54379	-0.10080
0.49453	-0.10266
0.45284	-0.10267
0.39600	-0.10196
0.36000	-0.10051
0.31453	-0.09722
0.27474	-0.09209
0.21221	-0.07338
0.19705	-0.07229
0.17621	-0.07450
0.17053	-0.08038
0.10042	-0.15351
0.09474	-0.15094
0.08526	-0.14874
0.07768	-0.14140
0.00568	-0.00330

Table 24: Velocity profile of v for M=10, when β_1=2, D^{-1}=3000 and E=0.01	
z	v
0.89432	-0.00110
0.82990	-0.01766
0.80716	-0.02465
0.77116	-0.04340
0.71811	-0.07134
0.67074	-0.08238
0.62905	-0.08644
0.58168	-0.09197
0.53811	-0.09419
0.48505	-0.09641
0.45284	-0.09643
0.39411	-0.09572
0.36000	-0.09426
0.29747	-0.09098
0.26716	-0.08658
0.20274	-0.05649
0.19326	-0.05539
0.18000	-0.05760
0.10232	-0.14175
0.09474	-0.14359
0.08526	-0.13919
0.07389	-0.12928
0.00758	-0.00330

Table 25: Velocity profile of v for D^{-1} = 2000, when β_1=2, M=2 and E=0.01	
z	v
0.89799	-0.00212
0.82349	-0.03141
0.78010	-0.05012
0.72899	-0.08400
0.66848	-0.09706
0.63502	-0.10271
0.58897	-0.10941
0.54276	-0.11294
0.50283	-0.11541
0.45649	-0.11612
0.40586	-0.11506
0.36571	-0.11294
0.31065	-0.10729
0.27243	-0.10129
0.20619	-0.08224
0.19144	-0.08224
0.18100	-0.84353
0.11712	-0.16059
0.10283	-0.17047
0.09216	-0.16765
0.07689	-0.15671
0.06998	-0.14400

Table 26: Velocity profile of v for D^{-1} = 3000, when β_1=2, M=2 and E=0.01	
z	v
0.89592	-0.00282
0.80868	-0.03035
0.72466	-0.08153
0.68297	-0.09141
0.63059	-0.09812
0.60326	-0.09953
0.57584	-0.09918
0.54427	-0.10024
0.51284	-0.10412
0.45835	-0.11082
0.41621	-0.11118
0.36760	-0.10835
0.27646	-0.09741
0.19793	-0.08576
0.18117	-0.08788
0.14274	-0.12247
0.11250	-0.15177
0.09567	-0.15247
0.08504	-0.15071
0.07154	-0.13235
0.00433	-0.00247

Table 27: Velocity profile of v for D^{-1} = 3000, when β_1=2, M=2 and E=0.01	
z	v
0.89164	-0.00141
0.84143	-0.00953
0.82068	-0.01659
0.80827	-0.02153
0.77967	-0.04094
0.73884	-0.06918
0.69525	-0.08365
0.66807	-0.08824
0.63242	-0.09212
0.59247	-0.09424
0.55669	-0.09529
0.52726	-0.09706
0.49578	-0.09988
0.45799	-0.10306
0.41583	-0.10306
0.36512	-0.10024
0.30164	-0.09494
0.27620	-0.09176
0.20786	-0.07271
0.19094	-0.07165
0.18266	-0.07482
0.17245	-0.08188
0.13135	-0.14929
0.11955	-0.16729
0.11352	-0.17365

Table 28: Velocity profile of v for D^{-1} = 4000, when β_1=2, M=2 and E=0.01	
z	v
0.90002	-7.52941
0.83698	-0.00459
0.81194	-0.00988
0.76910	-0.04024
0.72631	-0.07165
0.69507	0.07976
0.63428	-0.08682
0.57551	-0.09212
0.54189	-0.09424
0.48929	-0.09635
0.45346	-0.09635
0.40286	-0.09600
0.36271	-0.09388
0.30779	-0.09141
0.27173	-0.08647
0.20925	-0.05753
0.19015	-0.05471
0.18180	-0.05647
0.15961	-0.07765
0.13609	-0.11541
0.12217	-0.13341
0.10196	-0.15177
0.08725	-0.15282
0.08488	-0.14718
0.07366	-0.13271

Table 29 : Velocity profile of v for β_1=1, when D^{-1}=3000, M=2 and E=0.01	
z	v
0.89811	-0.00124
0.82059	-0.05011
0.79979	-0.06125
0.72416	-0.09469
0.68067	-0.10956
0.63908	-0.12135
0.61828	-0.12508
0.58613	-0.12574
0.54076	-0.12518
0.49349	-0.12216
0.45189	-0.11913
0.41219	-0.12104
0.38193	-0.12293
0.35924	-0.12358
0.31765	-0.12179
0.27227	-0.12000
0.22878	-0.11388
0.20231	-0.11145
0.18151	-0.11518
0.16261	-0.12694
0.14370	-0.14610
0.11534	-0.17330
0.10399	-0.17764
0.09076	-0.17395
0.07752	-0.16101

Table 30 : Velocity profile of v for β_1=2, when D^{-1}=3000, M=2 and E=0.01	
z	v
0.89811	-0.00124
0.82059	-0.05011
0.79979	-0.06125
0.72416	-0.09469
0.68067	-0.10956
0.63908	-0.12135
0.61828	-0.12508
0.58613	-0.12574
0.54076	-0.12518
0.49349	-0.12216
0.45189	-0.11913
0.41219	-0.12104
0.38193	-0.12293
0.35924	-0.12358
0.31765	-0.12179
0.27227	-0.12000
0.22878	-0.11388
0.20231	-0.11145
0.18151	-0.11518
0.16261	-0.12694
0.14370	-0.14610
0.11534	-0.17330
0.10399	-0.17764
0.09076	-0.17395
0.07752	-0.16101

Table 31 : Velocity profile of v for β_1=3, when D^{-1}=3000, M=2 and E=0.01	
z	v
0.89413	-0.00249
0.89814	-0.00149
0.80914	-0.08161
0.78700	-0.08162
0.74685	-0.10762
0.72038	-0.12189
0.68635	-0.13239
0.61719	-0.11861
0.60504	-0.14053
0.55966	-0.13997
0.52185	-0.13756
0.48025	-0.13329
0.45189	-0.13086
0.40840	-0.13277
0.36113	-0.13346
0.31576	-0.13228
0.26849	-0.12988
0.23824	-0.12807
0.20609	-0.12750
0.17773	-0.13309
0.15693	-0.14793
0.12668	-0.17699
0.10777	-0.18751
0.09454	-0.18444
0.08508	-0.17828

Table 32 : Velocity profile of v for β_1=4, when D^{-1}=3000, M=2 and E=0.01	
z	v
0.89622	-0.00247
0.85084	-0.05007
0.81113	-0.08407
0.76387	-0.11315
0.72227	-0.13049
0.69013	-0.13794
0.63151	-0.14420
0.58992	-0.14857
0.54076	-0.15173
0.49160	-0.15056
0.45189	-0.14938
0.39328	-0.14637
0.36113	-0.14518
0.30441	-0.13724
0.27227	-0.13605
0.21366	-0.14107
0.17962	-0.15037
0.15315	-0.17016
0.12668	-0.19365
0.10966	-0.20108
0.09454	-0.19864
0.09265	-0.19555
0.07563	-0.17582
0.00567	-0.00370

Table 33: Variations in the skin friction and Nusselt number under influence of Prandtl number, heat source parameter and radiation parameter.

Pr	*Q*	*F*	*Df*	τ_x	τ_y	*Nu*
2	1	0.21	1	2.2135	0.0111	2.4191
4	1	0.22	1	1.5995	0.0288	4.4673
5	1	0.22	1	1.4054	0.0378	5.4853
2	1	0.22	1	1.2534	0.0471	2.5026
2	3	0.22	1	2.4729	0.002	1.8596
2	4	0.22	1	2.3633	0.0032	1.0803
2	1	0.7	1	2.8319	0.1587	1.0492
2	1	0.78	1	2.796	0.1488	1.0498
2	1	0.96	1	2.7366	0.1254	1.0498
2	1	0.22	1	2.982	0.0848	1.1477
2	1	0.23	2	3.281	0.1713	1.2471
2	1	0.22	3	3.782	0.5178	1.6451

Table 34: Variations in the skin friction under the influence of Grashof number modified Grashof number, magnetic parameter, porosity parameter and rotation parameter

ttr	*ttm*	*M*	*K*	Ω	τ_x	τ_y
5	5	3	1.2	2.2	3.9445	0.0049
6	5	3	1.2	2.2	3.707	0.0037
7	5	3	1.2	2.2	3.4695	0.0024
8	5	3	1.2	2.2	3.132	0.0011
5	6	3	1.2	2.2	4.7479	0.2227
5	7	3	1.2	2.2	4.6309	0.1669
5	8	3	1.2	2.2	4.5138	0.0565
5	5	4	1.2	2.2	1.279	0.01
5	5	5	1.2	2.2	1.4619	0.0142
5	5	6	1.2	2.2	1.7388	0.0184
5	5	3	2.3	2.2	3.0392	0.0015
5	5	3	3.2	2.2	3.14	0.0016
5	5	3	4.3	2.2	3.2403	0.0018
5	5	3	1.2	3.2	3.1162	0.0015
5	5	3	1.2	4.2	3.1264	0.0014
5	5	3	1.2	8.2	3.1369	0.0013

Table 35: Effect of the chemical reaction parameters, Soret number and Schmidt number on skin friction and Sherwood number.

Kr	*Sc*	S_0	*Sh*
3	1	2	0.8081
5	1	2	1.2738
6	1	2	1.3197
3	1	2	0.1903
3	2	2	0.4004
3	3	2	0.9918
3	1	2	8.4573
3	1	4	7.9326
3	1	6	7.1524

Table 36: Data flow of the shear stresses (t_x) on the upper plate							
E	I	II	III	IV	V	VI	VII
0.01	0.084673	0.156783	0.246352	0.0625	0.046782	0.107466	0.145336
0.02	0.121454	0.186299	0.268751	0.116002	0.083146	0.144237	0.181673
0.03	0.146755	0.208889	0.278752	0.118208	0.121483	0.180083	0.256335
0.04	0.163752	0.408755	0.544798	0.127436	0.118442	0.207853	0.501651

	I	II	III	IV	V	VI	VII
M	2	5	8	2	2	2	2
D □1	2000	2000	2000	3000	4000	2000	2000
□1	5	5	5	5	5	6	8

Table 37: Data flow of the shear stresses (t_y) on the upper plate							
E	I	II	III	IV	V	VI	VII
0.01	-0.01468	-0.02561	-0.03216	-0.01565	-0.01682	-0.01512	-0.01811
0.02	-0.01814	-0.02848	-0.0482	-0.01255	-0.02845	-0.02147	-0.02532
0.03	-0.02107	-0.03245	-0.04552	-0.02856	-0.03216	-0.02659	-0.03275
0.04	-0.04251	-0.06838	-0.0755	-0.05478	-0.06253	-0.05865	-0.08314

	I	II	III	IV	V	VI	VII
M	2	5	8	2	2	2	2
D^{-1}	2000	2000	2000	3000	4000	2000	2000
□1	5	5	5	5	5	6	8

Table38: Data flow of the shear stresses (t_x) on the lower plate							
E	I	II	III	IV	V	VI	VII
0.01	0.000048	0.000054	0.000064	0.000042	0.000032	0.000052	0.000084
0.02	0.000066	0.000072	0.000083	0.000042	0.000034	0.000062	0.000098
0.03	0.000072	0.000079	0.000089	0.000052	0.000042	0.00008	0.000099
0.04	0.000085	0.000094	0.000132	0.000062	0.000048	0.000092	0.000145

	I	II	III	IV	V	VI	VII
M	2	5	8	2	2	2	2
D □1	2000	2000	2000	3000	4000	2000	2000
□1	5	5	5	5	5	6	8

Table39: Data flow of the shear stresses (t_y) on the lower plate							
E	I	II	III	IV	V	VI	VII
0.01	-0.00466	-0.00599	-0.00653	-0.00321	-0.00301	-0.00546	-0.00674
0.02	-0.00521	-0.00685	-0.00744	-0.00427	-0.00357	-0.00583	-0.00748
0.03	-0.00633	-0.00744	-0.00832	-0.00524	-0.00428	-0.00752	-0.00846
0.04	-0.00801	-0.00856	-0.00946	-0.00621	-0.00582	-0.00942	-0.00999

	I	II	III	IV	V	VI	VII
M	2	5	8	2	2	2	2
D^{-1}	2000	2000	2000	3000	4000	2000	2000
□1	5	5	5	5	5	6	8

REFERNCES :

1. Alam, M. S., Rahman, M. M., & Sattar, M. A. (2009). Effects of variable suction and thermophoresis on steady MHD combined free–forced convective heat and mass transfer flow over a semi-infinite permeable inclined plate in the presence of thermal radiation. *International Journal of Thermal Sciences*, *48*(4), 758–767.
2. Abo-Eldahab, E. M., & El Aziz, M. A. (2004). Blowing/suction effect on hydromagnetic heat transfer by mixed convection from an inclined continuously stretching surface with internal heat generation/absorption. *International Journal of Thermal Sciences*, *43*(7), 709–719.
3. Abbas, Z., Hayat, T., & Javed, T. (2011). MHD flow and heat transfer past a stretching sheet with Soret and Dufour effects. *International Journal of Heat and Mass Transfer, 54*(9–10), 2088–2097.
4. Ahern, R. A., & Vafai, K. (2016). Magnetohydrodynamic mixed convection in porous media. *Transport in Porous Media, 113*(2), 277–302.
5. Ahmad, M., & Munir, S. (2021). Unsteady MHD flow of a second-grade nanofluid over an exponentially stretching sheet with variable thermal conductivity. *European Physical Journal Plus, 136*, 1054.

6. Aksu, N., & Yurtseven, H. (2015). Second-grade fluid flow in a rotating porous disk under thermal radiation. *Journal of Non-Equilibrium Thermodynamics, 40*(2), 127–142.

7. Alam, N., Beg, O. A., & Siddiqui, M. U. (2022). Soret and Dufour effects in MHD flow of Maxwell nanofluid past a stretching surface. *Journal of Thermophysics and Heat Transfer, 36*(1), 175–185.

8. Ali, M. E. (2013). Viscous flow and heat transfer in a rotating porous disk with thermal radiation. *Applied Mathematics and Computation, 225*, 704–716.

9. Ali, N., Hayat, T., & Alsaedi, A. (2013). MHD flow of second-grade fluid over a stretching sheet with slip conditions. *International Journal of Heat and Mass Transfer, 60*, 690–696.

10. Alamri, A., & Hossain, M. A. (2020). Unsteady MHD Casson nanofluid flow over a rotating disk with Darcy–Forchheimer model. *Journal of Applied Fluid Mechanics, 13*(1), 39–49.

11. Al-Saedi, A., & Hayat, T. (2012). Numerical study on Soret and Dufour effects on MHD flow of viscoelastic nanofluid. *Results in Physics, 2*, 38–46.

12. Anwar, S., & Mehmood, S. (2024). Hall current and Joule heating effects on unsteady MHD flow with thermal radiation. *Frontiers in Heat and Mass Transfer, e024.*

13. Asibor, R. E., & Osudia, C. F. (2023). MHD flow properties due to a porous rotating disk in a mixed convective fluid flow with buoyancy and radiation. *Global Journal of Engineering and Technology Advances, 14*(3), 61–75.

14. Attia, H. A. (2012). Unsteady MHD flow near a rotating porous disk with uniform suction or injection. *Fluid Dynamics Research, 44*(5), 055515.

15. Awan, R. U., & Hayat, T. (2018). Slip flow and heat transfer of a Casson nanofluid past a stretching sheet through a porous medium. *International Journal of Heat and Mass Transfer, 127*, 1200–1207.

16. Baag, S., & Mishra, S. R. (2018). Heat and mass transfer in MHD micropolar fluid with Soret and Dufour effects. *Journal of Magnetism and Magnetic Materials, 467*, 152–160.

17. Bahria, F., & Rashid, M. (2020). Numerical investigation of Soret and Dufour effects on MHD flow of an Oldroyd-B fluid. *Journal of Marine Science and Application, 19*, 12–21.

18. Basit, A., & Shah, Z. (2017). Combined influence of thermal radiation and chemical reaction on MHD flow past a stretching sheet. *Journal of Thermal Analysis and Calorimetry, 127*(3), 1563–1574.

19. Behboudi, A., & Izadi, M. (2011). Boundary layer flow and heat transfer of Jeffrey fluid past a stretching sheet. *International Journal of Heat and Mass Transfer, 54*(17–18), 4037–4045.

20. Bejan, A., & Nield, D. A. (2013). *Convection in Porous Media* (5th ed.). Springer.

21. Bilal, S., & Qasim, M. (2021). Unsteady MHD nanofluid flow of Williamson fluid over a rotating disk with thermal radiation. *Journal of Applied Physics, 129*, 085101.

22. Bilal, S., & Ali, T. (2022). Soret and Dufour effects on MHD Casson fluid flow through a porous channel. *Physics of Fluids, 34*(3), 032004.

23. Biswas, M., & Pop, I. (2015). MHD flow of nanofluid past a stretching sheet with chemical reaction. *International Journal of Engineering Science, 96*, 152–164.

24. Ceylan, İ., & Yildirim, A. (2023). Unsteady magnetohydrodynamic flow and heat transfer over a rotating disk in porous media. *Heat and Mass Transfer, 59*, 131–141.

25. Chhabra, R. P., & Richardson, J. F. (2011). *Non-Newtonian Flow and Applied Rheology* (2nd ed.). Butterworth-Heinemann.

26. Choi, S. U. S. (1995). Enhancing thermal conductivity of fluids with nanoparticles. In D. A. Siginer & H. P. Wang (Eds.), *Developments and Applications of Non-Newtonian Flows* (Vol. 231, pp. 99–105). ASME.

27. Das, K., & Jana, R. N. (2013). Hall current effects on MHD rotating disk flow of viscoelastic fluid. *Journal of Magnetism and Magnetic Materials, 333*, 107–116.

28. Das, S., & Jana, R. N. (2010). Hall effects on unsteady MHD flow of viscous incompressible fluid through a porous channel in a rotating system. *Journal of Naval Architecture and Marine Engineering, 7*(2), 87–102.

29. Dhamecha, D., & Goyal, M. (2022). Impact of variable thermal conductivity on MHD Jeffrey nanofluid flow. *Results in Applied Mathematics, 10*, 100249.

30. Dogonchi, A. S., & Ganji, D. D. (2021). MHD nanofluid flow with Soret and Dufour effects in diverging/converging channel. *Journal of Thermal Analysis and Calorimetry, 143*, 1371–1384.

31. Dogonchi, A. S., & Ganji, D. D. (2023). Dufour and Soret effects in MHD Darcy–Forchheimer flow of Maxwell fluid. *Engineering Science and Technology, an International Journal, 41*, 101254.

32. Elgazzar, A. (2022). Effects of variable viscosity and thermal conductivity on rotating MHD nanofluid over a stretching sheet. *International Communications in Heat and Mass Transfer, 138*, 106901.

33. Ertunç, Ö., & Ekmekci, F. (2024). Unsteady MHD flow of a second-grade corotating nanofluid past a stretching disk. *Physics of Fluids, 36*(2), 023105.

34. Ezati, M., & Hatami, N. (2014). Influence of Soret and Dufour effects on MHD stagnation-point flow of nanofluid past a stretching cylinder. *Journal of Nanofluid, 3*, 73–81.

35. Fakhar, K., Xu, Z., & Yi, C. (2008). Exact solutions of a third-grade fluid flow on a porous plate. *Applied Mathematics and Computation, 202*, 376–382. https://doi.org/10.1016/j.amc.2008.02.029

36. Ganesan, N., & Selvaraj, N. (2017). Unsteady MHD flow of micropolar fluid with slip conditions over stretching sheet. *Journal of Industrial and Engineering Chemistry, 51*, 342–350.

37. Ganjehi, A. (2012). MHD mixed convection in a rotating porous channel with thermal radiation. *Applied Mathematical Modelling, 36*(2), 902–914.

38. Ghosh, B. C. (2019). Numerical study of unsteady MHD flow over a rotating disk with variable viscosity and thermal radiation. *International Journal of Fluid Mechanics Research, 46*(4–5), 375–390.

39. Gnaneswara, R. M., & Venkatesh, K. (2022). Soret and Dufour effects on MHD heat and mass transfer of Williamson nanofluid over a rotating disk. *Journal of Thermal Engineering, 8*(2), 205–218.

40. Gupta, P. S., & Gupta, A. S. (1977). Heat and mass transfer on a stretching sheet with suction or blowing. *Canadian Journal of Chemical Engineering*, *55*(6), 744–746.

41. Hartmann, J. (1937). Theory of the laminar flow of an electrically conductive liquid in a homogeneous magnetic field. *Mathematica Fysica Meddelelser*, *15*(6), 1–28.

42. Hassan, S. F., & Attia, H. A. (2021). MHD boundary layer flow over a rotating disk with Hall current and thermal radiation. *Heliyon*, *7*(3), e06587.

43. Hayat, T., Alsaedi, A., & Khan, I. (2015). Soret and Dufour effects on MHD flow of Maxwell fluid past a rotating disk. *International Journal of Heat and Mass Transfer*, *82*, 580–589.

44. Hayat, T., & Abbas, Z. (2012). MHD flow of a second-grade fluid with thermal radiation and Ohmic heating. *Physics Letters A, 376*, 1479–1485.

45. Hayat, T., Javed, T., & Imtiaz, M. (2016). Unsteady MHD flow and heat transfer past an oscillating plate in a porous medium with Soret and Dufour effects. *Journal of Magnetism and Magnetic Materials, 397*, 42–50.

46. Hatami, N., Ebrahim, S., & Hatami, B. (2013). Soret and Dufour effects on MHD flow past a stretching sheet with viscous dissipation. *Physica Scripta, 88*, 038502.

47. Hayat, T., Imtiaz, M., & Alsaedi, A. (2018). Analytical solutions for MHD flow of third-grade nanofluid with Soret–Dufour in a porous channel. *Mathematical Methods in the Applied Sciences, 41*(10), 3756–3770.

48. Ibrahim, E. M., & Bakr, A. A. (2020). Chemical reaction and thermal radiation effects on MHD flow over a rotating cylinder. *Results in Physics*, *19*, 103445.

49. Ishak, A., Nazar, R., & Pop, I. (2008). Hydromagnetic flow and heat transfer adjacent to a stretching vertical sheet. *Heat and Mass Transfer, 44*(8), 921–927.

50. Ishak, A., & Nazar, R. (2011). MHD flow and heat transfer of a Casson fluid over a vertical plate with radiation. *International Journal of Applied Mechanics, 03*(6), 1131–1142.

51. Jeffreys, H. (1929). *The Earth: Its Origin, History and Physical Constitution*. Cambridge University Press.

52. Johnson, N., & Pop, I. (2019). Numerical simulation of rotating MHD nanofluid flow over a stretching surface with Soret and Dufour effects. *Journal of Porous Media, 22*(5), 531–546.

53. Khan, W. A., & Pop, I. (2010). Boundary-layer flow of a nanofluid past a stretching sheet. *International Journal of Heat and Mass Transfer, 53*(11–12), 2477–2483.

54. Kumaran, V., & Ramanaiah, G. (2011). MHD flow past a stretching cylinder with slip boundary. *Chemical Engineering Science, 66*(5), 948–956.

55. Lavanya, S., & Kalaivanan, K. (2022). Effect of variable thermal conductivity on MHD flow of Oldroyd-B nanofluid over a rotating disk. *Journal of Thermal Analysis and Calorimetry, 147*, 1593–1605.

56. Li, X., & Li, Y. (2021). Soret and Dufour effects on unsteady MHD flow and heat transfer over a stretching sheet. *International Journal of Thermal Sciences, 164*, 106872.

57. Lin, C. H., & Tu, J. Y. (2012). Analysis of MHD flow and heat transfer of a nanofluid over a stretching surface with Dufour–Soret effects. *Heat Transfer Research, 43*(8), 687–703.

58. Liu, Q., & Fan, J. (2019). Enhanced heat transfer of MHD nanofluids in a rotating porous channel. *International Journal of Numerical Methods for Heat & Fluid Flow, 29*(2), 541–559.

59. Magyari, E., & Keller, B. (2000). Heat and mass transfer in the boundary layers on an exponentially stretching continuous surface. *Journal of Physics D: Applied Physics, 32*(5), 577–585.

60. Matin, M., & Hashim, I. (2014). Thermal radiation effect on unsteady MHD flow of a third-grade fluid past a stretching surface. *Journal of Molecular Liquids, 200*, 125–133.

61. Mishra, S. R., Baag, S., & Mohapatra, D. K. (2016). Chemical reaction and Soret effects on hydromagnetic micropolar fluid along a stretching sheet. *Engineering Science and Technology, 19*(4), 1919–1928.

62. Mythili, D., & Sivaraj, R. (2016). Influence of higher-order chemical reaction and non-uniform heat source/sink on Casson fluid flow over a vertical cone and flat plate. *Journal of Molecular Liquids, 216*, 466–475.

63. Nagamani, K., & Varadharajan, K. (2016). Triple diffusive MHD flow of Maxwell nanofluid over a stretching sheet with Soret, Dufour, and Holmes–Mahta effects. *Results in Physics, 6*, 1296–1303.

64. Na, T. Y. (1979). *Computational Methods in Engineering Boundary Value Problems*. Academic Press.

65. Nadeem, S., & Ashraf, S. (2019). MHD flow of a Williamson nanofluid over a stretching surface with Soret and Dufour effects. *Journal of Thermal Analysis and Calorimetry, 136*, 2033–2044.

66. Nield, D. A., & Bejan, A. (2017). *Convection in Porous Media* (5th ed.). Springer.

67. Nandeppanavar, M. M., Vajravelu, K., Abel, M. S., & Ravi, S. (2010). Heat transfer in MHD viscoelastic boundary layer flow over a stretching sheet with thermal radiation and non-uniform heat source/sink. *Communications in Nonlinear Science and Numerical Simulation, 16*(9), 3578–3590.

68. Navier, C. L. M. H. (1823). Mémoire sur les lois du mouvement des fluides. *Mémoires de l'Académie Royale des Sciences de l'Institut de France, 6*, 389–440.

69. Nauman, E. B. (2019). *Chemical Reactor Design, Optimization, and Scaleup* (2nd ed.). McGraw-Hill Education.

70. Naz, M. Y., & Siddiqui, A. (2020). Slip flow and heat transfer of a Herschel–Bulkley fluid over a stretching surface with Soret and Dufour effects. *Physics of Fluids, 32*(12), 123105.

71. Oldroyd, J. G. (1950). On the formulation of rheological equations of state. *Proceedings of the Royal Society of London. Series A, Mathematical and Physical Sciences, 200*(1063), 523–541.

72. Pal, D., & Mondal, H. (2010). Effect of variable viscosity on MHD non-Darcy mixed convective heat transfer over a stretching sheet embedded in a porous medium with non-uniform heat source/sink. *Communications in Nonlinear Science and Numerical Simulation, 15*(6), 1553–1564.

73. Pantokratoras, A. (2014). Nonlinear thermal radiation effect on MHD flow over a stretching sheet with Soret and Dufour effects. *International Journal of Heat and Mass Transfer, 78*, 499–508.

74. Prasad, K. V., Abel, S., & Datti, P. S. (2003). Diffusion of chemically reactive species of a non-Newtonian fluid immersed in a porous medium over a stretching sheet. *International Journal of Non-Linear Mechanics, 38*(5), 651–657.

75. Postelnicu, A. (2004). Influence of a magnetic field on heat and mass transfer by natural convection from vertical surfaces in porous media considering Soret and Dufour effects. *International Journal of Heat and Mass Transfer, 47*(6–7), 1467–1472.

76. Prandtl, L. (1904). Über Flüssigkeitsbewegung bei sehr kleiner Reibung. *Verhandlungen des III. Internationalen Mathematiker-Kongresses*, 484–491.

77. Quinn, B., & Johnson, G. R. (2011). Numerical simulation of unsteady MHD flow in porous rotating channels. *Computers & Fluids, 58*, 78–89.

78. Raptis, A., & Perdikis, C. (2006). Viscous flow over a non-linearly stretching sheet in the presence of a chemical reaction and magnetic field effect. *International Journal of Non-Linear Mechanics, 41*(4), 527–529.

79. Reynolds, O. (1883). An experimental investigation of the circumstances which determine whether the motion of water shall be direct or sinuous. *Philosophical Transactions of the Royal Society, 174*, 935–982.

80. Schlichting, H., & Gersten, K. (2017). *Boundary-Layer Theory* (9th ed.). Springer.